ΕΘΝΙΚΟ ΜΕΤΣΟΒΙΟ ΠΟΛΥΤΕΧΝΕΙΟ
Σχολή Εφαρμοσμένων Μαθηματικών και
Φυσικών Επιστημων
Τομέας Φυσικής

Διπλωματική Εργασία - Diploma Thesis

# Προσομοίωση Δέσμης Ηλεκτρονίων σε Γραμμικό Επιταχυντή για Ακτινοθεραπεία FLASH

# Electron Beam Simulation in Linear Accelerators for FLASH Radiotherapy

Ράγγος Βασίλειος - Rangos Vasileios

Επιβλέπων: Καθηγητής Γεωργακίλας Αλέξανδρος

Τριμελής εξεταστική επιτροπή:

| | | |
|---|---|---|
| ..... | ..... | ..... |
| Γεωργακίλας | Γαζής | Κοψαλής |
| Αλέξανδρος | Ευάγγελος | Ιωάννης |
| Καθηγητής ΕΜΠ | Ομ. Καθηγητής ΕΜΠ | Επ. Καθηγητής ΕΜΠ |

Αθήνα, Σεπτέμβριος 2024

Βασίλειος Ράγγος, Σχολή Εφαρμοσμένων Μαθηματικών και Φυσικών Επιστημών, Τομέας Φυσικής, Εθνικό Μετσόβιο Πολυτεχνείο

**Ευχαριστίες**

Με αυτό το μήνυμα θα ήθελα πολύ να εκφράσω τις θερμές μου ευχαριστίες στους καθηγητές κ. Αλέξανδρο Γεωργακίλα και κ. Ευάγγελο Γαζή για την αμέριστη υποστήριξή τους καθ' όλη τη διάρκεια της διπλωματικής μου εργασίας. Ο κ. Γαζής μου προσέφερε σημαντική καθοδήγηση και γνώσεις στον τομέα των γραμμικών επιταχυντών και ο κ. Γεωργακίλας συνέβαλε καθοριστικά στην κατανόηση και την μελέτη των βλαβών DNA από ιοντίζουσες ακτινοβολίες.

Θα ήθελα να ευχαριστήσω την οικογένειά μου που ήταν δίπλα μου και με στήριζαν καθ' όλη τη διάρκεια αυτής της διαδρομής. Ευχαριστώ τους φίλους μου για όλες τις στιγμές χαράς, τα ταξίδια και τις εμπειρίες που ζήσαμε.

Special thanks to Professor Robert D. Stewart from the University of Washington, who provided valuable assistance in understanding the MCDS simulation and offered insightful approaches for addressing the case of FLASH radiotherapy.

# Contents

## List of Figures

## List of Tables

**Abstract**

To enhance the efficiency of radiotherapy in targeting cancerous cells, various methods are employed. FLASH radiotherapy (FLASH-RT), which delivers dose rates greater than 40 Gy/s, has shown a potential to significantly reduce damage to normal tissues while maintaining effectiveness in destroying tumors compared to conventional techniques.

The objective of this thesis is to simulate the beam dynamics within the accelerating structure of a linear accelerator, that will be able to deliver high charge density electrons in order to achieve ultra high dose rates required for FLASH-RT.

This study will examine the impact of different parameters regarding the accelerator structure to the output beam and see the behavior of the beam inside the waveguide. Space charge effects must be taken into consideration, as the high charge density of the beam leads to expansion due to internal electromagnetic forces. Dose and dose rate will be approximated as well.

Finally, there will be an attempt to simulate DNA damage by FLASH irradiation using a Monte Carlo simulation. This will take into account assumptions about the environment of the irradiated site and indirectly approximate DNA lesions for both protons and electrons.

**Key words**

LINAC, linear accelerator, beam physics, DNA damage, Radiotherapy, FLASH-RT, Ultra High Dose Rate, ASTRA simulation, MCDS, electron beams, proton beams, ionizing radiation

**Περίληψη στα Ελληνικά**

Μια σύνηθης μέθοδος αντιμετώπισης καρκινικών όγκων είναι με ακτινοθεραπεία. Κατά την διάρκεια της θεραπείας, δηλαδή, οι ασθενείς ακτινοβολούνται με φορτισμένα σωματίδια υψηλής ενέργειας (ηλεκτρόνια, πρωτόνια, ιόντα) ή φωτόνια στο φάσμα των ακτίνων X ή γ. Πρόσφατες μελέτες έχουν δείξει, πως ο ρυθμός ακτινοβόλησης παίζει σημαντικό ρόλο στο αποτέλεσμα της θεραπείας και πιο συγκεκριμένα για ρυθμούς δόσης μεγαλύτερους των 40Gy/s, έχει παρατηρηθεί πως οι υγιείς ιστοί επιβιώνουν καλύτερα σε σχέση με τις συμβατικές θεραπείες, ενώ είναι το ίδιο αποδοτική στο να σκοτώνει καρκινικά κύτταρα. Αυτό ονομάζεται φαινόμενο FLASH και έχουν γίνει αρκετές μελέτες σε ζώα αλλά και σε ανθρώπους με θετικά αποτελέσματα. Η παραγωγή όμως δέσμης ικανής για να ακτινοβοληθεί ένας ιστός με τόσο υψηλό ρυθμό δόσης είναι μια πρόκληση, καθώς η πυκνότητα φορτίου είναι πολύ μεγάλη και πρέπει να γίνουν τροποποιήσεις στην τεχνολογία κλινικών γραμμικών επιταχυντών ώστε να υποστηρίζονται οι παραπάνω προϋποθέσεις αλλα ταυτόχρονα να είναι πρακτικό και οικονομικά βιώσιμο. Αντικείμενο μελέτης αυτής της εργασίας είναι η προσομοίωση πυκνής δέσμης ηλεκτρονίων στον κυματοδηγό γραμμικού επιταχυντή και μελέτη της συμπεριφοράς της για διάφορες παραμέτρους εισόδου.

Στο **δεύτερο κεφάλαιο** γίνεται περιγραφή της διάταξης ενός τυπικού γραμμικού επιταχυντή. Η παραγωγή των ηλεκτρονίων γίνεται με την μέθοδο της θερμιονικής εκπομπής. Θερμαίνεται δηλαδή ένα μεταλλικό σύρμα και από το νέφος ηλεκτρονίων που προκύπτει γύρω από αυτό, με εφαρμογή ηλεκτρικού πεδίου προεπιταχύνονται σε μία σχετικά χαμηλή ενέργεια (50-80keV συνήθως) και παράγεται ένα συνεχές ρεύμα ηλεκτρονίων. Με εφαρμογή εναλλασσόμενου ηλεκτρομαγνητικού πεδίου, η δέσμη γίνεται παλμική καθώς κάποια σωματίδια επιταχύνονται ενώ κάποια επιβραδύνονται με αποτέλεσμα να παράγονται δέσμες σωματιδίων.

Στην συνέχεια τα σωματίδια εισάγονται στην επιταχυντική διάταξη, η οποία είναι ένας κυματοδηγός κυκλικής διατομής. Στο εσωτερικό του υπάρχουν δίσκοι με ίριδες που τον χωρίζουν σε μικρότερους χώρους. Οι δέσμες που εισάγονται εκεί επιταχύνονται από ηλεκτρομαγνητικά κύματα σε μικροκυματικές συχνότητες η παραγωγή των οποίων γίνεται με χρήση λυχνίων κλύστρον. Για την εστίαση της δέσμης χρησιμοποιούνται σωληνοειδή και τετραπολικοί μαγνήτες. Το μαγνητικό πεδίο από αυτές τις διατάξεις τροποποιεί τις ιδιότητες της δέσμης στο εγκάρσιο επίπεδο.

Στο **τρίτο κεφάλαιο** γίνεται αναφορά στην δυναμική των δεσμών. Στον διαμήκη άξονα αναλύονται οι περιοχές σταθερότητας και αστάθειας της δέσμης σε σχέση με την θέση του ηλεκτρομαγνητικού κύματος κατα μήκος της τροχιάς. Στο εγκάρσιο επίπεδο αναλύεται η επίδραση των τετραπόλων στην δέσμη καθώς εστιάζεται ή αποεστιάζεται. Αναφέρονται οι ποσότητες που σχετίζονται με την διαδικασία αυτή, καθώς και παράμετροι για την ποιότητα της δέσμης όπως η εκπεμψιμότητα. Τέλος, οι απωστικές δυνάμεις μεταξύ των σωματιδίων που τείνουν να αποεστιάσουν την δέσμη πρέπει να ληφθούν υπόψιν, καθώς για τις μεγάλες πυκνότητες φορτίου τα φαινόμενα αυτά είναι πολύ έντονα, ειδικά στις χαμηλές ταχύτητες.

Στο **τέταρτο κεφάλαιο** αναγράφεται η θεωρία των αλληλεπιδράσεων ιοντιζουσών ακτινοβολιών με την ύλη. Περιγράφονται μηχανισμοί αλληλεπίδρασης φορτισμένων και μη σωματιδίων, η παραγωγή ακτίνων X και δίνεται έμφαση στα ηλεκτρόνια υψηλής ενέργειας. Ορίζονται τα μεγέθη για την δοσιμετρία ακτινοβολιών καθώς και σημαντικοί παράμετροι που χρησιμοποιούνται στην ακτινοθεραπεία. Περι-

γράφονται στη συνέχεια οι αλληλεπιδράσεις με την βιολογική ύλη, οι βλάβες DNA που προκύπτουν, οι μηχανισμοί επιδιόρθωσης και ένα μοντέλο που δείχνει το κλάσμα επιβίωσης. Δεν απουσιάζει βέβαια μια σύντομη ανάλυση για το φαινόμενο FLASH και οι πιθανοί μηχανισμοί που ενδεχομένως περιγράφουν το φαινόμενο αυτό, καθώς ο ακριβής τρόπος δράσης δεν είναι ακόμη γνωστός.

Το **πέμπτο κεφάλαιο** είναι για την προσομοίωση ηλεκτρονίων στον γραμμικό επιταχυντή. Αρχικά γίνεται προσομοίωση με το παράδειγμα που δίνει ο οδηγός του λογισμικού και ύστερα τροποποιώ τις παραμέτρους όπως το πλάτος του ηλεκτρομαγνητικού κύματος για να βγάλω έξοδο με διαφορετικές ενέργειες. Σε δεύτερη φάση γίνονται προσομοιώσεις αλλά λαμβάνοντας υπόψιν τις δυνάμεις μεταξύ των σωματιδίων στην δέσμη, που αλλοιώνει αρκετά τα αποτελέσματα, καθώς πολλές φορές η δέσμη γίνεται ασταθής και πρέπει να αλλάξουν οι τιμές της αρχικής ενέργειας ή το αρχικό μέγεθός της ή το πλάτος του ηλεκτρομαγνητικού κύματος ώστε να διατηρείται σταθερή. Εξετάζεται επίσης η επίδραση σωληνοειδούς που βοηθάει στην εστίαση της δέσμης. Το λογισμικό δίνει επίσης την δυνατότητα να απεικονίσει γραφικά τις Ηλεκτρομαγνητικές δυνάμεις που ασκούνται στο φορτίο και μελετάται το μέγεθός τους σε διάφορες ενέργειες.

Στο **έκτο κεφάλαιο** γίνεται δοσιμετρία σε στόχο νερού δεδομένων των παραμέτρων εξόδου της αρχικής προσομοίωσης και μια δεύτερη προσομοίωση (MCDS) η οποία υπολογίζει τις βλάβες DNA. Καθώς το συγκεκριμένο λογισμικό Monte Carlo δεν υποστηρίζει ρυθμούς δόσης αντίστοιχους του FLASH, θα γίνει μια προσπάθεια προσέγγισης των συνθηκών στην ακτινοβολούμενη περιοχή με βάση κάποιες θεωρίες στον τρόπο που ενδεχομένως λειτουργεί το FLASH. Από τις γραφικές παραστάσεις θα γίνει μια σύντομη ποιοτική ανάλυση για το κατά πόσο αυτή η μέθοδος θα μπορούσε να είναι αποδοτική, καθώς και μια σύγκριση μεταξύ πρωτονίων και ηλεκτρονίων.

**Λέξεις Κλειδιά**

LINAC, γραμμικός επιταχυντής, βλάβες DNA, Ακτινοθεραπεία, FLASH-RT, ASTRA, MCDS, δέσμες πρωτονίων, δέσμες ηλεκτρονίων, ιοντίζουσες ακτινοβολίες

# 1 Introduction

Radiotherapy is a critical component of cancer treatment, which uses high-energy radiation to target and destroy cancer cells. Linear accelerators (LINACs), cyclotrons and synchrotrons that can deliver high-energy charged particles (protons, electrons, ions) or photons directly to tumours are widely used in clinical setups. This thesis will be focusing on electron Linacs that deliver high charge density electron beams.

The primary aim of radiotherapy is to precisely target and destroy cancer cells using radiation as described while minimizing damage to the surrounding healthy tissues around it, by delivering focused radiation doses that shrink or eradicate cancerous growths. The treatment can be either as standalone radiotherapy or a combination with other therapies like surgery or chemotherapy. Overall, the ultimate goal is to improve the patient's quality of life and making the treatment less invasive and minimizing discomfort.

Recent research has shown that the dose rate can play an important role in the outcome of radiotherapy. It has been shown that at rates greater than 40 Gy/s normal cells seem to have a better survival rate than in conventional therapies, while maintaining similar anti-tumour effects. This phenomenon is known as the FLASH effect, has shown the potential to revolutionize radiotherapy. Generating such ultra-high dose rate beams, however, remains a significant challenge due to the need for very high charge density particle beams and the equipment must be compact enough to be suitable for clinical enviromnets.

To simulate the beam within the LINAC and the output beam characteristics, the software "ASTRA" (A Space-charge TRacking Algorithm) will be used. Charged particle beams experience repulsive forces that tend to expand the beam and need to be taken into consideration. ASTRA can also calculate those space charge forces for a given charge distribution. The output dose and dose rate will be approximated using the output data from ASTRA and using water as a target.

Finally, an attempt will be made to simulate the conditions at the irradiated site using MCDS. Currently, there is no software capable of simulating FLASH dose rates and their effect on biological matter. While MCDS may not offer precise or detailed simulations, it will be used to qualitatively approximate the effects of variations in oxygen and DMSO (a ROS scavenging agent) concentrations. This approach aims to provide an estimate of how these factors influence the radiotherapy process. By taking some properties of FLASH irradiation into account, the factors above will be adjusted to mirror the conditions at the irradiated site.

## 2 Linear Accelerators

Sources: [1] [4]

Linear accelerators (linac) are devices that accelerate charged particles along a straight line, using time dependent electromagnetic fields. In RF linacs, radiofrequency electromagnetic waves are used to accelerate particles. The first linac was proposed by Rolf Wideroe in 1928[16]. It was made of coaxial metallic tubes, where the accelerating field is generated in gaps between adjacent tubes (Fig 2.0.1). That array was able to accelerate potassium ions up to 50keV, by applying an altrenating voltage at 25kV at a frequency of 1MHz.

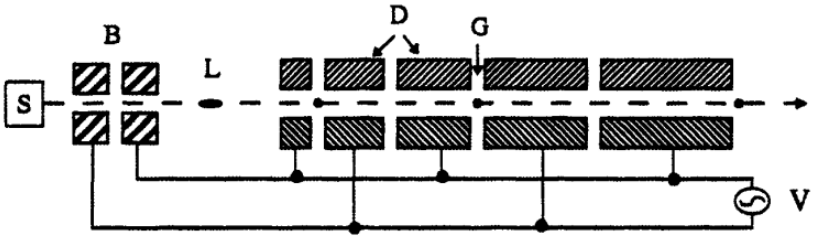


Figure 2.0.1: Wideroe drift tube linac [1]

During World War II, the invention of devices used for radar systems (Klystron), were useful to generate high power RF signals, but the Wideroe linac would become unstable. To overcome this issue, Alvarez [17] proposed a structure that encloses the gaps between the tubes with metallic cavities. The acceleration section would now be composed of a series of tubes forming, together with the outer enclosure a resonant cavity (Fig 2.0.2).

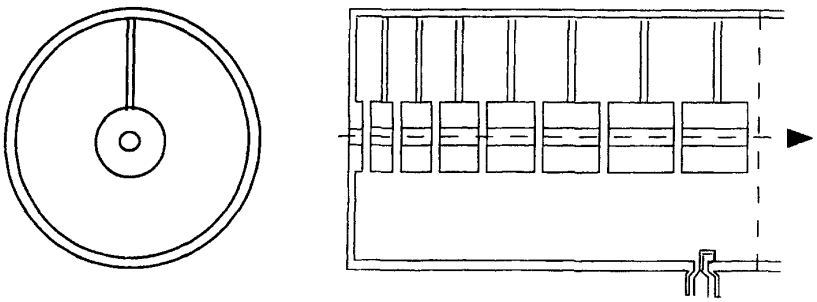

Figure 2.0.2: Alvarez Drift Tube Linac Cavity [1]

Linear accelerators are widely used for a variety of application including electron/positron colliders, high-quality electron beams for free-electron lasers and for radiotherapy either by delivering directly electrons to the patient or being used as an X-ray source by bombarding a target (like tungsten) to produce electromagnetic radiation capable of killing tumours.
The complete LINAC structure that will be discussed below, consists of a DC electron source that will be bunched before entering the accelerating waveguide. Inside the structure there are accelerating cavities and focusing magnets. The system needs to be cooled and operates in a vacuum.

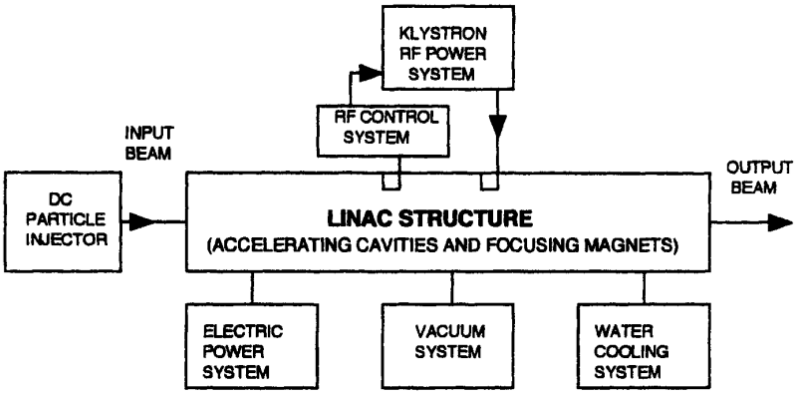


Figure 2.0.3: LINAC block diagram [1]

## 2.1 Electron Sources and Pre-Acceleration in Linear Accelerators

### 2.1.1 Electron emission

Sources: [2] [3] [18] [19]

The simplest model of an electron source is the planar diode. Electrons are emitted from the cathode and accelerated to the anode due to the potential difference between the electrodes.

The main principle of operation of thermionic emission is that the cathode is heated and a cloud of electrons forms around the heated cathode. By applying an electric field, electrons are accelerated towards the anode, which has a small opening for the beam to escape. This method is impractical because most electrons will hit the anode. In order to ensure that most electrons pass through that opening, a third electrode is introduced to strongly focus the beam (Wenhelt triode gun [20]). Also the anode is cooled.

The flow of electrons can be monitored through fluorescent screens and controlled by either regulating the electric field or the temperature of the cathode. There are some disadvantages of controlling the cathode temperature, because factors like thermal conductivity that increase the response time. The Wenhelt potential can significantly vary the beam output without the need to change the anode voltage or cathode temperature.

Electrons have to escape from the metal surface which means that they have to gain enough energy to escape the cathode. If $\phi_{work}$ the work function of the metal, we get that:

$$e(\phi_{out} - \phi_{work}) = -\frac{e^2}{16\pi^2\epsilon_0 x^2} - eE_0 x \tag{2.1.1}$$

At the cathode, the kinetic energy required must be at least:

$$K = \frac{1}{2}mv_x^2 > e\phi_{work} => v_x > \sqrt{\frac{2\phi_{work}}{m}} \tag{2.1.2}$$

Electrons are fermions and follow Fermi-Dirac statistics, that are described by the

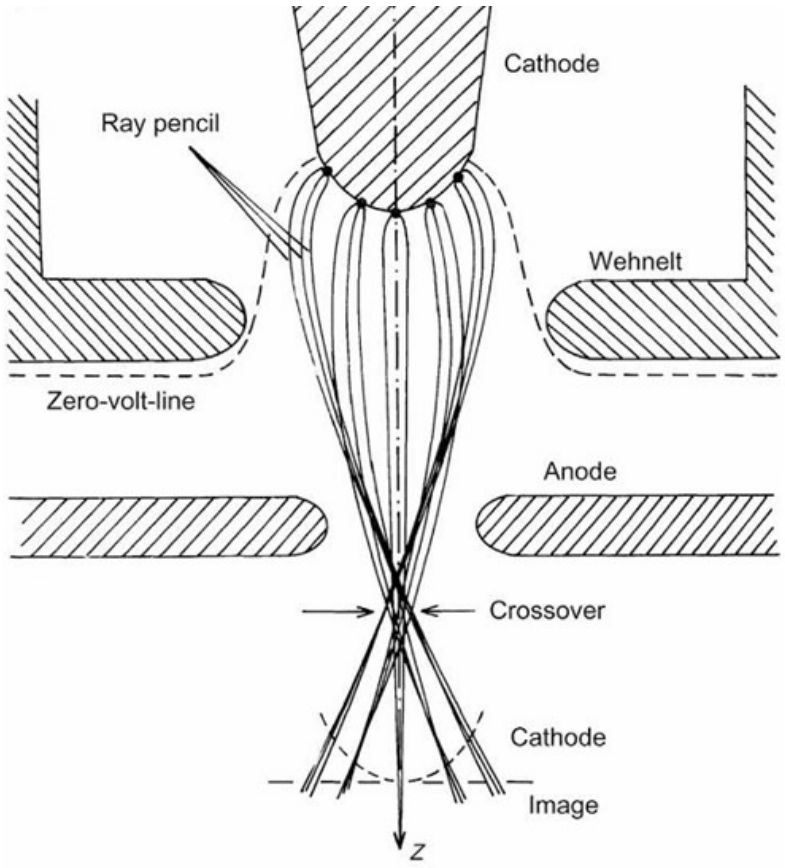


Figure 2.1.1: Structure of a triode and electron trajectories. [2]

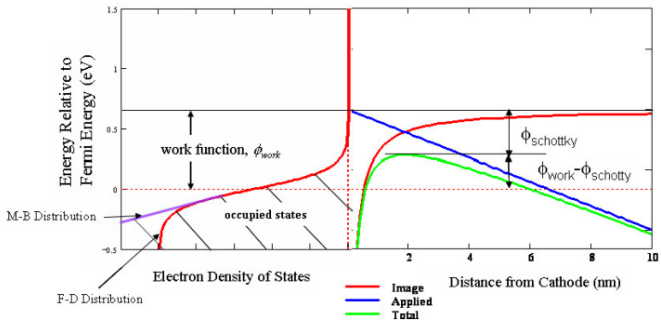


Figure 2.1.2: Emission occurs when electrons have enough energy to overcome the potential 'barrier' [3]

Fermi-Dirac distribution:

$$f(E) = \frac{1}{e^{\frac{E-\mu}{kT}} + 1} \tag{2.1.3}$$

The thermionic current density can be written as $J = en\langle v_x \rangle$ and by using the

Maxwell speed distribution [21]

$$J = en\langle v_x \rangle \ = en \int_{v_{x0}}^{\infty} v_x f_{FD}\, d\vec{v}$$

$$J = A(1-r)T^2 e^{-\frac{\phi}{kT}} \quad \text{where } A = \frac{|e|mk_B^2}{2\pi^2\hbar^3} \tag{2.1.4}$$

which is the Richardson-Dutchman equation. The current density is dependent on the temperature $T$ of the cathode and the work function $\phi$ of the metal. The factor $(1-r)$ accounts for the reflection of electrons at the metal surface. The value of $A$ is constant and equal to $A = 1.2 * 10^{-6} Am^{-2}K^{-2}$.
To design a thermionic cathode it is important to use materials that:

- Have a low work function
- Have a long lifetime at high temperatures

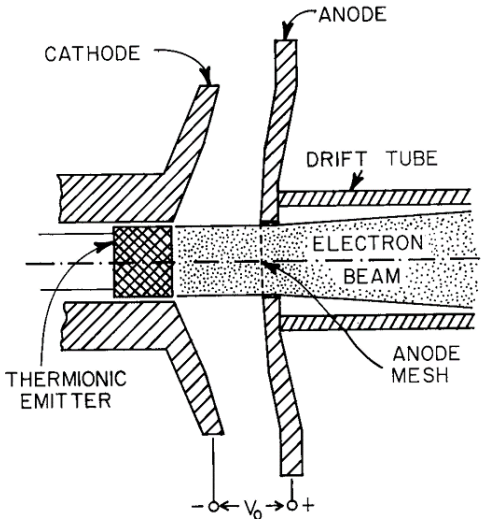


Figure 2.1.3: Electron beam in a thermionic emitter. [2]

Electrons are pre-accelerated through this process and leave the electron gun as a DC current.

Electron guns used in standard accelerators are characterized by their high-quality optics and their flexibility rather than by their emission power.

### 2.1.2 Pre-Injector/Pre-Buncher

[4] The beam must be properly prepared before acceleration. Particles might be generated in a continuous stream (like that from the thermionic emission) at specific energies that are relatively low or from a microwave source of different frequency. The accelerating fields of a linac are usually oscillatory, which means that not all particles will be accelerated. Thus it is required to bunch the beam and to be concentrated at an optimal phase to achieve maximum intensity.

A simple concept to produce a bunched beam is by passing the continuous beam through a chopper system. At the end of the chopper system a pulsed beam

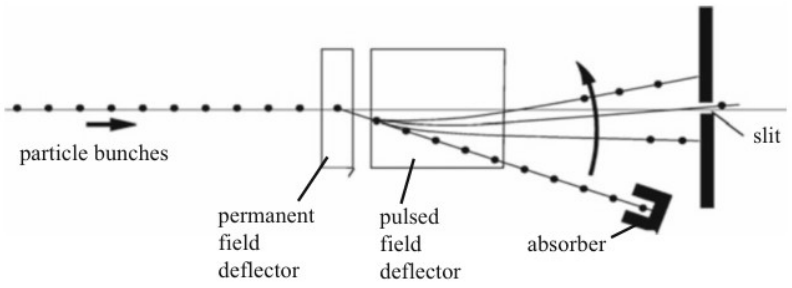


Figure 2.1.4: Chopper system. [4]

is produced but there are many losses inbetween. As described later, this system is useful in combination with an RF prebuncher. The prebuncher consists of an RF cavity followed by a drift space. In this area, some particles are accelerated and some are decelerated.

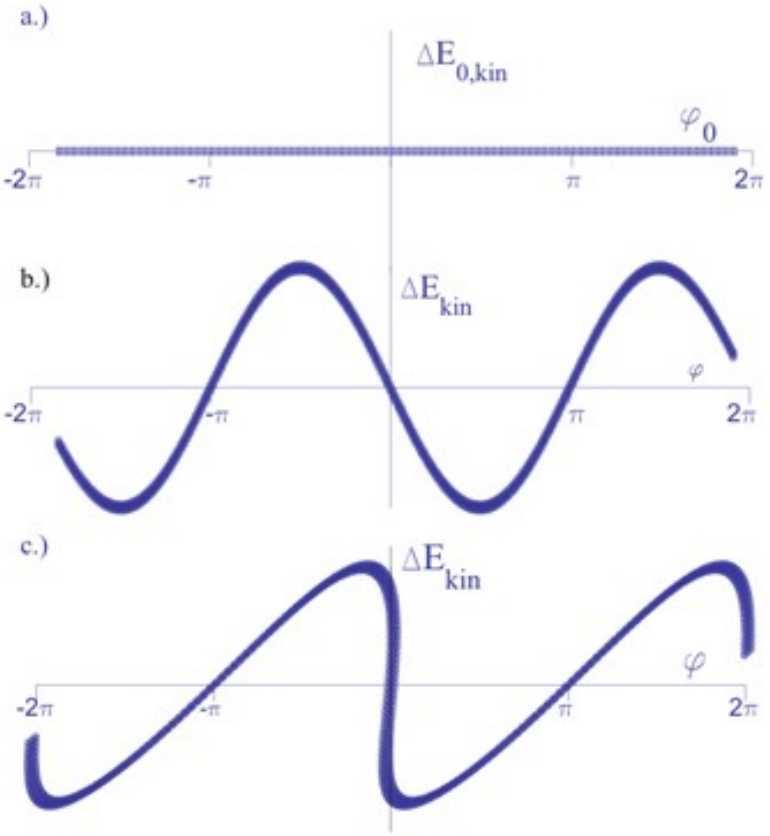


Figure 2.1.5: Energy spread of electrons. [4]

As seen on Figure 2.1.5, a continuous stream of particles enters the prebuncher (a). In the RF-cavity a sinusodidal electric field is applied and the particle distribution becomes as (b). The energy modulation corresponds to a velocity modulation. Due to that, after a distance L downstream of the buncher cavity shows strong bunching (c).

For a prebuncher operating at a voltage $V = V_0 \sin(\phi)$, the energy is $E = eV_0 \sin(\phi) = \gamma mc^2$ and the energy spread given the velocity spread is equal to $\delta E = mc^2\gamma^3\beta\delta\beta$. Perfect bunching occurs at a time $\Delta t$ later when $\sin(\phi) \approx \phi$.

$$\phi = \frac{2\pi}{\lambda_{rf}} c\delta\beta\Delta t = k_{rf} c\delta\beta\Delta t$$

where $\lambda_{rf}$ is the RF wavelength in the cavity. We obtain for non relativistic particles that:

$$\Delta t = \frac{\lambda_{rf}}{2\pi}\frac{mv}{eV_0}, \quad L = v\Delta t = \frac{2E}{k_{rf}eV_0}, \quad \delta L = \frac{\delta E}{k_{rf}eV_0}$$

A significant portion of the particles might reach the end of the linac with a large energy deviation (from zero to maximum energy), which may lead to particles being lost in a subsequent beam transport system and create high radiation levels. Those low energy particles can be eliminated through the use of a chopper system. In order to achieve single pulse, the chopper system will consist of a permanent magnet that deflects the beam into an absorber and a fast pulsed magnet that deflects the beam away from the absorber across a small slit.

## 2.2 Accelerating Structures

### 2.2.1 LINAC waveguide

Sources: [1],[4]

LINACS consist of a circular waveguide structure is modified by adding iris like metallic disks (see fig 2.2.1) that reduce the phase velocity to that of the particles (see fig 2.2.2). The linac consists of a sequence of identical "tanks" separated by the irises, each containing a set of accelerating cells.

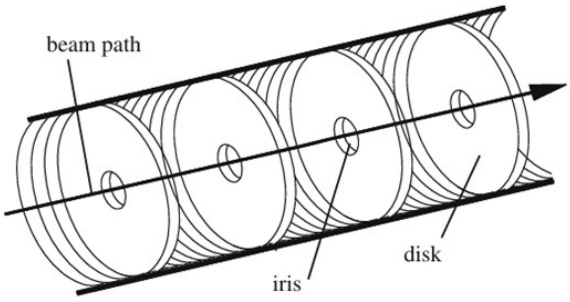


Figure 2.2.1: Iris loaded disk structure [4]

An electromagnetic wave is initiated at the input cell of every tank, propagating along the beam direction, where beam bunches are injected along the axis to undergo acceleration by the wave. The electromagnetic energy is absorbed by the **conductor walls** and the **beam**, so the field amplitude is reduced in each tank and the remaining energy is delivered to an external resistive load. Acceleration

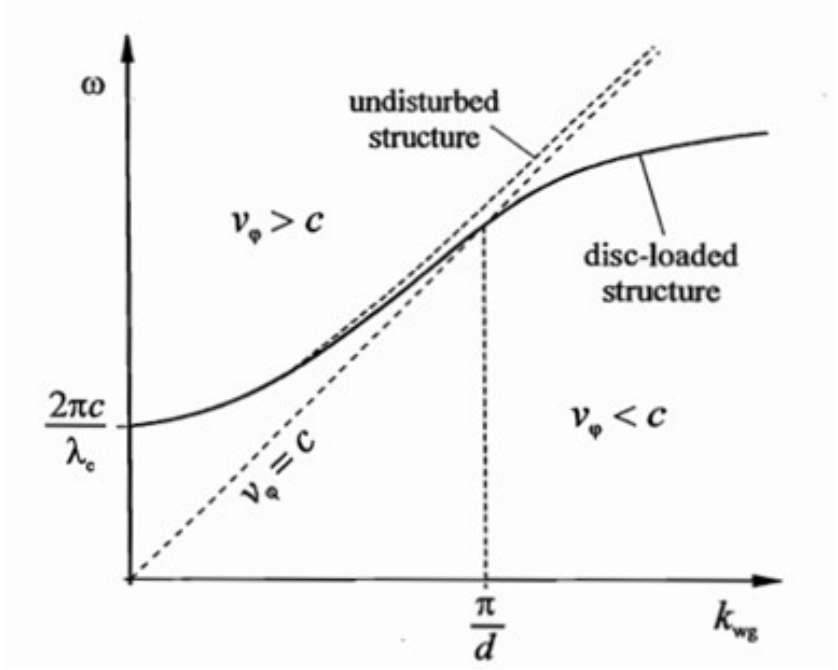


Figure 2.2.2: Phase velocity in disc loaded structure. [5]

should be achieved with high power efficiency, which means that the energy gain of the beam per unit length should be maximized.

One parameter to be considered is the operating frequency because high power efficiency is achieved at higher frequencies (shunt resistance proportional to $\omega^{1/2}$), but at higher frequencies the interactions of the charged particles with the conductor walls, create the undesirable effects of **wakefields**, which are proportional to $\omega^2$ in the longitudinal direction and proportional to $\omega^3$ in the transverse plane, must be taken into consideration. A common frequency, which is also used in SLAC, is 2856MHz.

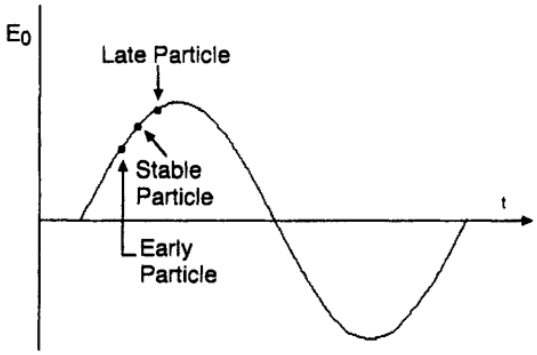


Figure 2.2.3: The particle bunch must be synchronous to the travelling wave. In order for the beam to be stable, it must be located in the region shown. [1]

The RF cavities for particle acceleration can aslo be operated in standing wave modes. Standing wave cavities operating at steady state are usually used in synchrotrons and storage rings for beam acceleration or energy compensation of synchrotron radiation energy loss. The standing wave can also accelerate oppositely charged beams traveling in opposite directions. [22]

### 2.2.2 Particle acceleration by EM waves

Sources: [1] [22]

Charged particles should not move parallel to the direction of the em wave. The electric field must be parallel to the direction of the beam. The design principle of RF cavities is a waveguide that provides Electric field along the particle trajectory at a phase velocity equal to that of the particle.

In linac technology, EM waves are propagated in transmission lines, waveguides and cavities. Since there are no true monochromatic waves in nature, waves exist in groups that are a superposition of waves with different frequencies and wave numbers. If the spread of the phase velocities of the individual waves is small, the total wave will tend to maintain its shape and move with a velocity called **group velocity**. The wave fronts inside the accelerating structure move at **phase velocity**, which should be modulated to match the particle speed.

$$v_p = \frac{\omega}{k} \quad v_g = \frac{d\omega}{dk} \tag{2.2.1}$$

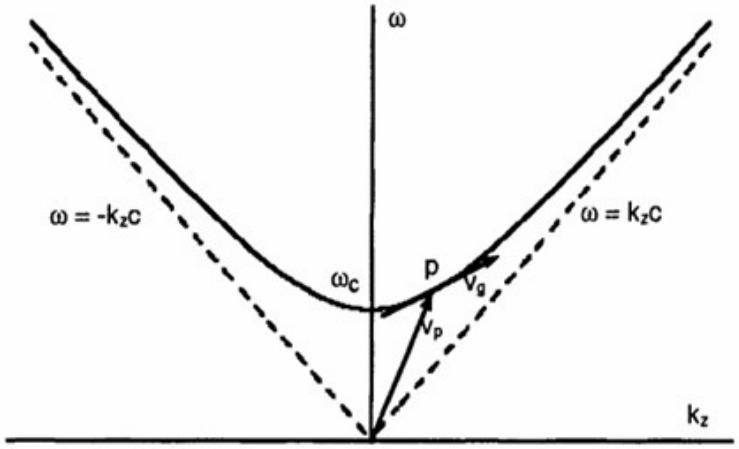


Figure 2.2.4: Phase and group velocities. [1]

### 2.2.3 Fundamental properties

Sources: [1] [4] [23] [22]

**Transit time factor** Considering an electric field $\vec{E_z} = \vec{E_0}\cos(\omega t)$, the energy gain in traversing the accelerating gap is $\Delta W = eE_0\cos(\omega t)$.

$$\Delta E = e\int_{-L/2}^{L/2} E_0\cos(\frac{\omega z}{\upsilon})dz = eE_0LT_{tr} = eV_0$$

$$T_{tr} = \frac{sin(\frac{\pi L}{\beta\lambda})}{\frac{\pi L}{\beta\lambda}} \tag{2.2.2}$$

where $E_0 L T_{tr}$ is the effective voltage of the gap and $T_{tr}$ is the transit time factor that can be defined as the passage time through the RF-cavity. The RF-wavelength is $\lambda = 2\pi c/\omega$ and $\frac{\pi L}{\beta\lambda}$ is the RF phase shift across the gap. Higher efficiency is achieved for smaller gap length but there is a limit under which arcing may occur. For a value of $L = \beta\lambda/4$ we have $T_{tr} = 0.9$ but there is little gain for values of $L < \beta\lambda/4$ A typical value for standing wave structures in DTL (drift tube linacs) is about 0.8.
A reduction of the accelerating voltage gap increases the transit time factor, but a small gap can cause an electric field breakdown (spark) due to the Kilpatrick effect. This can occur if the Electric field is high enough and air is present. This used to be the case in older systems and it was experimentally derived that:

$$f(MHz) = 1.64 E_k e^{-8.5/E_k} \tag{2.2.3}$$

where $E_k$ is the electric field in $MV/m$.

**Transit time effect** Regardless of the phase $\phi$ of the particle in a harmonically time varying field, the energy gain is less than the energy gain in a constant electric field. The transient time factor can be defined as the ratio for a given value of the maximum electric field ac/dc as well. T is a measure of the reduction in the energy gain caused by the sinusoidal time variation of the field in the gap.

$$T_{tr} = \frac{\int_{-L/2}^{L/2} E_0 \cos(\frac{\omega z}{v}) dz}{\int_{-L/2}^{L/2} E_0 dz} \tag{2.2.4}$$

**Shunt Impedance** Electromagnetic energy is consumed in the cavity wall and due to the beam acceleration. The shunt impedance for an RF cavity is defined as:

$$R_{sh} = \frac{V_0^2}{P_d} \tag{2.2.5}$$

where $V_0$ is the effective acceleration voltage and $P_d$ is the dissipated power. It is useful to define the shunt impedance per unit length:

$$r_{sh} = \frac{R_{sh}}{l_{cav}} = \frac{V_0^2}{P_d L_{cav}} = \frac{e^2 L_{cav}}{P_d} \tag{2.2.6}$$

$$\frac{dP_d}{dz} = -\frac{E^2}{r_{sh}}$$

where $E$ is the effective longitudinal electric field that includes the transit time factor and $\frac{dP_d}{dz}$ is the power loss per unit length in the wall. For high frequencies, shunt impedance is proportional to $\omega^{1/2}$. A high shunt impedance with low surface

fields is an important guideline in RF cavity design because it indicates less energy losses, better performance, stability and higher beam quality.
It is important to define the effective shunt impedance:

$$R = R_{sh}T_{tr}^2 \tag{2.2.7}$$

where $T_{tr}$ the transit time factor and the effective shunt impedance per unit length:

$$r = r_{sh}T^2 = \frac{R}{L} = \frac{E^2T_{tr}^2}{P_dL_{cav}} \tag{2.2.8}$$

**Quality factor** $Q$ The quality factor is defined as:

$$Q = \frac{\omega W_{st}}{P_d} \tag{2.2.9}$$

where $W_{st}$ the maximum stored energy.
It can also be rewritten as follows

$$\frac{dW_{st}}{dt} = -P_d = -\frac{\omega W_{st}}{Q}, \quad W_{st} = W_{st0}e^{-\frac{2t}{t_f}}, \quad t_f = \frac{2Q_L}{\omega}$$

here $Q_L$ is the loaded Q-factor factor that includes the resistance of the power source, $t_F$ is the filling time for the standing wave operation, which is equal to the time for the field to decay by a factor $1/e$. The Q-factor is independent of weather it operates in standing or travelling wave modes.
For a travelling wave structure we can define the stored energy per unit length:

$$w_{st} = \frac{W_{st}}{L_{cav}}, \quad \frac{dP_d}{dt} = -\frac{\omega w_{st}}{Q}, \quad t_f = \frac{L_{cav}}{v_g}$$

where $v_g$ the group velocity. It is also important to define the quantity:

$$R_{sh}/Q = \frac{V_0^2}{\omega W_{st}} \quad or \quad r_{sh}/Q = \frac{E^2}{\omega w_{st}}$$

which is dependent on the geometry and independent of the wall materials.

### 2.2.4 Fields in Waveguides

Waveguides are structures that guide waves by restricting the transmission of energy to one direction. We suppose waveguides made by ideal conductors with no skin depth. The boundary conditions for the walls are that $\vec{E_{//}} = \vec{0}$ and $B_\perp = 0$. For waves that propagate in the $z$ direction we end up to the following equations:

$$\left[\frac{\partial^2}{\partial x^2} + \frac{\partial^2}{\partial y^2} + \left(\frac{\omega}{c}\right)^2 - k^2\right] E_z = 0 \tag{2.2.10}$$

$$\left[\frac{\partial^2}{\partial x^2} + \frac{\partial^2}{\partial y^2} + \left(\frac{\omega}{c}\right)^2 - k^2\right] B_z = 0 \tag{2.2.11}$$

The solutions to the equations above are:

$$\vec{E}(x,y) = \vec{E_0}(x,y)e^{j(kz-\omega t)} \quad \vec{B}(x,y) = \vec{B_0}(x,y)e^{j(kz-\omega t)}$$

Different modes are characterized based on the components of the electric and magnetic fields and can be:

- Transverse Electric (TE) when $E_z = 0$
- Transverse Magnetic (TM) when $B_z = 0$
- TEM when both $E_z = 0$ and $B_z = 0$

The EM fields of the lowest frequency TM01 mode traveling in the z direction are:

$$\begin{gathered} E_z = E_0 J_0(k_c r)e^{-j(kz-\omega t)} \\ E_r = j\frac{k}{k_r}E_0 J_1(k_c r)e^{-j(kz-\omega t)} \\ H_\phi = j\frac{\omega}{ck_c\sqrt{\mu_0/\epsilon_0}}E_0 J_1(k_r r)e^{-j(kz-\omega t)} \\ E_\phi = 0, \quad H_z = 0, \quad H_r = 0 \\ k^2 = (\omega/c)^2 - k_c^2 \end{gathered} \tag{2.2.12}$$

where $k_c = p_{mn}/a$, $p_{mn}$ the points at which the Bessel function $J_{mn} = 0$ and $a$ the radius. Hollow-pipe waveguides do not support TEM waves. Many modes labeled as $m, n$ can propagate through the waveguide and have cutoff frequencies $\omega_{mn}$. Phase and group velocities are:

$$v_{ph} = \frac{\omega}{k} = \frac{\omega c}{\sqrt{\omega^2 - \omega_{mn}^2}} > c \tag{2.2.13}$$

$$v_g = \frac{d\omega}{dk} = c\sqrt{1 - \frac{\omega_{mn}^2}{\omega^2}} < c \tag{2.2.14}$$

The time required to traverse the waveguide (filling time) is defined as:

$$t_F = \int_0^L \frac{dz}{v_g} \tag{2.2.15}$$

Specifically for circular waveguides in TM mode the phase velocity is equal to:

$$v_{ph} = \frac{c}{\sqrt{\epsilon\mu}\sqrt{1 - \left(\frac{k_c}{k}\right)^2}} > c \tag{2.2.16}$$

Electromagnetic energy travels with group velocity less than the speed of light. As shown in eq. 2.2.16, the phase velocity is greater than the speed of light, which means that there is no net acceleration, because the wave rolls over the particles that cannot move faster than light.

### 2.2.5 Pillbox Cavity solution

Source: [22]
We consider a cylinder with both ends closed and a standing wave solution. With a dime dependendt factor $e^{j\omega t}$, The solutions are:

In the Alvarez linac (resembles the TM010 standing wave mode) as the speed of the particles increases, we increase the distance between the drift tubes.

$$
\begin{array}{ll}
E_z = Ck_c^2 J_m(k_c r)\cos(m\phi)\cos(kz) & H_z = 0 \\
E_r = -Ckk_c J'_m(k_c r)\cos(m\phi)\sin(kz) & H_r = -jC\frac{m\omega\epsilon_0}{r} J_m(k_c r)\sin(m\phi)\cos(kz) \\
E_\phi = Cnk\frac{1}{r} J_m(k_c r)\sin(m\phi)\sin(kz) & H_\phi = -jC\omega\epsilon_0 k_c J'_m(k_c r)\cos(m\phi)\cos(kz)
\end{array}
$$

Table 2.2.1: Electric and Magnetic fields in cylindrical coordinates

## 2.3 Other LINAC parts

### 2.3.1 Klystron

Source: [6]
Klystrons are used to provide a high power RF signal to the accelerating structure. An elementary two-cavity Klystron requires an electron beam that is produced though thermionic emission and the electrons are pre-accelerated to have a DC flow. The first cavity is a buncher and the second cavity is a catcher. At the buncher a low level microwave signal is applied that bunches the electrons, later to be 'catched' at the second cavity. The kinetic energy is converted to electromagnetic energy and the remaining electrons are absorbed. Higer power klystrons have additional cavities to improve high current bunching and amplification.

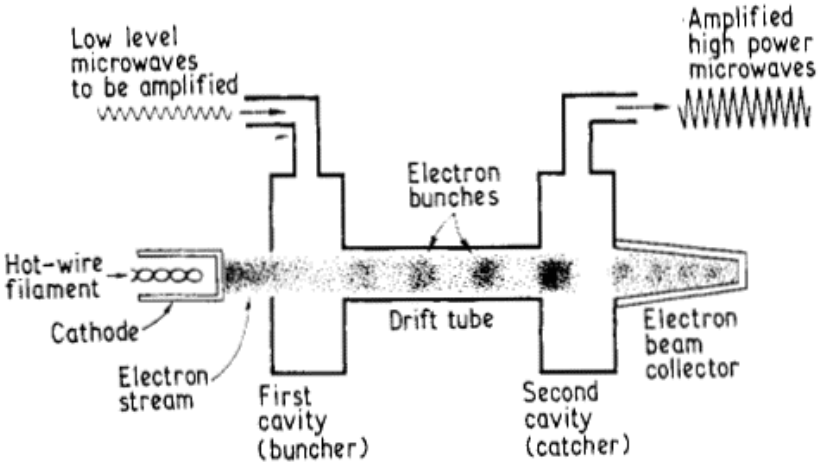


Figure 2.3.1: Klystron structure [6]

### 2.3.2 Solenoids

Source: [1]
Solenoids produce a magnetic field along their axis and can be used for electron or ion focusing. Particles moving along the magnetic field are not affected but charged particles with a velocity component vertical to the magnetic field will be accelerated to a helical motion. Comparison of a solenoid lens with a single quadrupole is not valid since at least two quadrupoles are needed to produce focusing in both planes. Compared with quadrupole doublets or triplets of the same performance, it is usually found that the power dissipation in a solenoid is much higher. At the end of the solenoid, the magnetic field dissipates. The motion

can be described from the equation:

$$\frac{d^2r}{ds^2} + \left[\frac{qB_{rms}}{2\gamma mv} - \frac{k_{l0}^2}{2}\right]r = 0 \tag{2.3.1}$$

### 2.3.3 Ideal quadrupole magnet

Source: [1]
In the ideal quadrupole magnet, at the pole tips, the magnetic field lines form hyperbolas and have a constant transverse quadrupole gradient $G$:

$$G = \frac{\partial B_y}{\partial x} = \frac{\partial B_x}{\partial y}$$

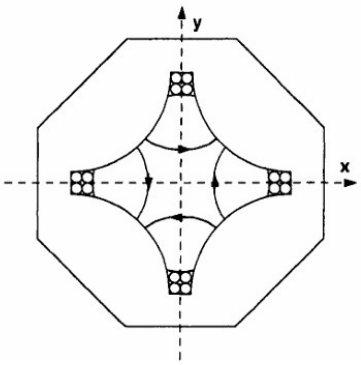


Figure 2.3.2: Quadrupole magnet. [1]

The Lorentz force can be written as:

$$F_x = -qvGx, \quad F_y = qvGy$$

We distinguish the following cases:

- If $qG > 0$, we get defocusing in y axis and focusing in the x axis
- If $qG < 0$, we get defocusing in x axis and focusing in the y axis

They can be used to focus (F) or defocus (D). Along the linac there might be inbetween the focusing structures drift space or bending magnets (O). A common arrangement is FODO.
A quadrupole transport channel can be described by the equation of motion:

$$\ddot{x} + K(s)x = 0 \tag{2.3.2}$$

# 3 Beam dynamics

## 3.1 Longitudinal beam dynamics

[1][4] For particle acceleration we must generate fields that will force the particles to accelerate in the desired direction. Such fields are called longitudinal or accelerating fields. They can be static, pulsed or electromagnetic fields oscillating at high frequencies. The simplest way to accelerate particles is by the use of two plates that have a voltage difference (electrostatic acceleration). This method is mostly used for low energy particle acceleration, because at higher voltages a voltage breakdown may occur.

Successful particle acceleration depends on stable and predictable interaction of charged particles and electromagnetic fields. Acceleration depends on the momentary phase of the field as seen by the particle. Ion LINACs are designed to accelerate a single particle which is synchronous to the accelerating fields and it is called a *synchronous particle*, For an acceptable output beam intensity, restoring forces must be present so that particles near the synchronous particle will have stable trajectories. In order to produce longitudinal restoring forces, that produce phase and energy oscillations around the synchronous particle, the electric field should be increasing with time.

### 3.1.1 Differential equations for longitudinal motion

To derive the difference equations we assume that the particle travels through drift space (where no forces are applied) and thin gaps where the forces are applied as impulses. Within the gap, the particle has constant velocity $\beta$ and $l$ the half cell

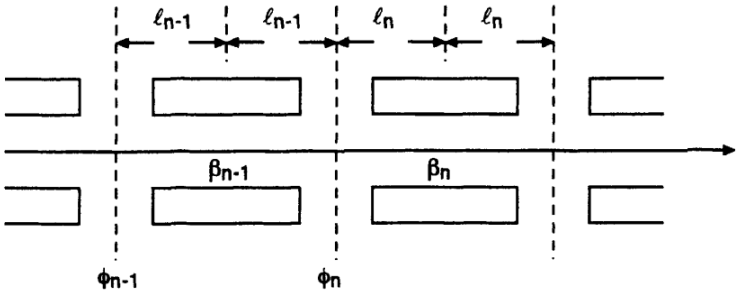


Figure 3.1.1: Accelerating cells [1]

length (Fig 3.1.1). The phase changes as follows:

$$\phi_n - \phi_{n-1} = \omega \frac{2l_{n-1}}{\beta_{n-1}c} + \theta \tag{3.1.1}$$

where $\theta$ =0 for 0 mode and $\pi$ for $\pi$ mode. The half cell length is: (N=1 for 0 mode and 1/2 for $\pi$ mode)

$$l = \frac{N\beta_s\lambda}{2}$$

The cell length is measured form the center of one to the center of the next drift tube:

$$L_n = N\lambda \frac{\beta_{s,n-1} + \beta_{s,n}}{2} \tag{3.1.2}$$

The phase change during the time an arbitrary particle travels from gap n-1 to gap n relative to that of the synchronous particle is:

$$\Delta(\phi - \phi_s)_n = \Delta\phi_n - \Delta\phi_{s,n} = 2\pi N \beta_{s,n-1} \left( \frac{1}{\beta_{n-1}} - \frac{1}{\beta_{s,n-1}} \right) \tag{3.1.3}$$

and we can approximate using taylor expansion:

$$\frac{1}{\beta} - \frac{1}{\beta_s} \approx -\frac{\delta\beta}{\beta_s^2} \quad , \delta\beta << 1$$

Form $W = \gamma mc^2$ we can get:

$$\delta W = \left| \frac{\partial W}{\partial \beta} \right| \delta\beta = \gamma^3 \beta mc^2 \delta\beta$$

The energy change of a particle relative to that of the synchronous particle can be written as follows:

$$\Delta(W - W_s)_n = qE_0 T L_n (\cos\phi_n - \cos\phi_{s,n}) \tag{3.1.4}$$

The differential equations can be written by approximating $\Delta(W - W_s) = d(W - W_s)/dn$, $\Delta(\phi - \phi_s) = d(\phi - \phi_s)/dn$ and replacing $n = s/N\beta_s\lambda$ and we get the following coupled differential equations:

$$\gamma_s^3 \beta_s^3 \frac{\Delta(\phi - \phi_s}{ds} = -2\pi \frac{W - W_s}{mc^2\lambda} \tag{3.1.5}$$

$$\frac{d(W - W_s)}{ds} = qE_0 T(\cos\phi - \cos\phi_s) \tag{3.1.6}$$

### 3.1.2 Beam stability and separatrix

By solving the equations above (3.1.5 and 3.1.6), we find that there are specific trajectories in phase space, where stable and unstable regions are separated. Within the stable regions, the particles perform oscillations.

The separatrix defines the area within which the trajectories are stable. It is also called the fish, and the stable area within is called the bucket. There are two solutions; one stable and another unstable. For a linac that is designed to accelerate relativistic electrons, the synchronous velocity profile is easily maintained, regardless of field or energy errors, because all relativistic particles have a velocity approximately equal to c.

## 3.2 Transverse beam dynamics

### 3.2.1 Focusing

[1] [4] Most common way to focus the beam (or counteract transverse rf defocusing) is by the use of magnetic lenses, more commonly magnetic quadrupole lens. They are located:

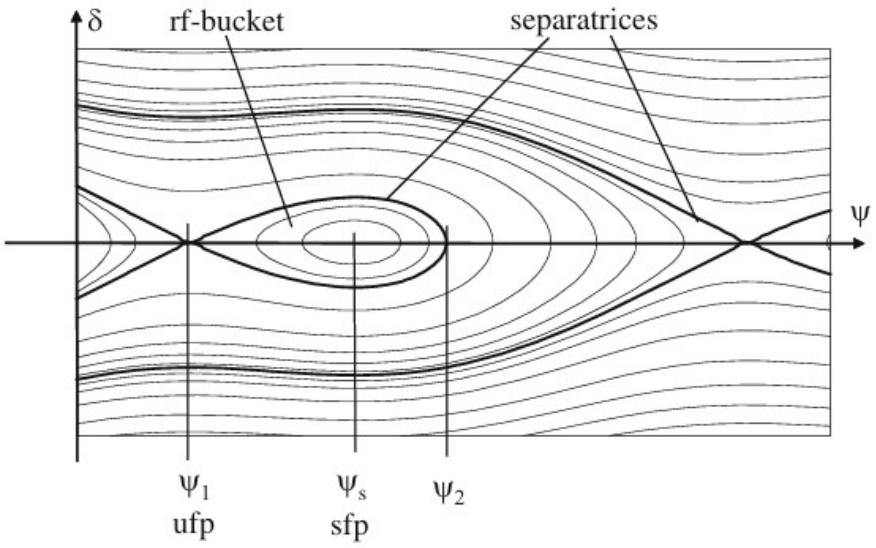


Figure 3.1.2: RF bucket and separatrices. The Stable and Unstable fixed points are shown [4]

- between the tanks in coupled cavity linacs
- within the drift tubes in drift tube linacs

### 3.2.2 Matrix Formalism

The solution to eq2.3.2 $\ddot{x} + K(s)x = 0$ can be written in a matrix form as a function of the initial conditions $x_0$ and $x_0'$:

$$\begin{bmatrix} x \\ x' \end{bmatrix} = \begin{bmatrix} a & b \\ c & d \end{bmatrix} \begin{bmatrix} x_0 \\ x_0' \end{bmatrix}$$

The 2x2 matrix is called a transfer matrix (R) and its determinant is equal to 1. The value of $K = \frac{qG}{mc\beta\gamma}$. For the different parts of an accelerator we have the following cases:

(a) Drift space (K=0)

$$R = \begin{bmatrix} 1 & l \\ 0 & 1 \end{bmatrix} \tag{3.2.1}$$

where $l$ the drift space

(b) Focusing quadrupole $K > 0$

$$R = \begin{bmatrix} \cos(\sqrt{K}l) & \frac{\sin(\sqrt{K}l)}{\sqrt{K}} \\ -\sqrt{K}\sin(\sqrt{K}l) & \cos(\sqrt{K}l) \end{bmatrix} \tag{3.2.2}$$

(c) Defocusing quadrupole $K < 0$

$$R = \begin{bmatrix} \cosh(\sqrt{K}l) & \frac{\sinh(\sqrt{K}l)}{\sqrt{K}} \\ -\sqrt{K}\sinh(\sqrt{K}l) & \cosh(\sqrt{K}l) \end{bmatrix} \tag{3.2.3}$$

(d) Thin lens approximation

$$R = \begin{bmatrix} 1 & 0 \\ \pm 1/f & 1 \end{bmatrix} \tag{3.2.4}$$

where $f$ the focal length and if:

- $f < 0$ it is a focusing lens
- $f > 0$ it is a defocusing lens

This holds when we suppose $sqrt|K|l \to 0$ while $|K|l$ is finite

$$\frac{1}{f} = \frac{qGl}{mc\beta\gamma}$$

The total transfer matrix is the product of the individual matrices and the correct order for elements in a sequence $1, 2, 3, ..., n$ is the product $R = R_n R_{n-1} ... R_2 R_1$.

### 3.2.3 Phase-amplitude solution

Suppose $K(s)$ to be a periodic function and a solution $x(s)$ that has the same period:

$$x(s) = \sqrt{\epsilon_1 \beta(s)} \cos\left[\phi(s) + \phi_1\right]$$

where $\epsilon_1, \phi_1$ constants determined by the initial conditions and $\beta(s)$ the amplitude function. For $\phi(s)$ we have:

$$\phi(s) = \int \frac{ds}{\beta(s)}$$

We also define the following functions:

$$\alpha(s) = -\frac{1}{2}\frac{d\beta(s)}{ds}, \quad \gamma(s) = \frac{1 + \alpha^2(s)}{\beta(s)}$$

All those parameters $\alpha, \beta, \gamma$ are called *Twiss Parameters* or *Courant-Snyder Parameters* that from an ellipse. The general form of the equation of an ellipse is:

$$\gamma x^2 + 2\alpha x x' + \beta x'^2 = \epsilon_1$$

The area of the ellpise is equal to $A = \pi\epsilon_1$.

The initial conditions $x_0$ and $x_0'$ are altered as we traverse an array of accelerator components, as illustrated in a preceding section by the expression $X = RX_0$. Subsequently, we can employ calculations to determine the Twiss parameters subsequent to the beam's passage through the accelerator components. The ellipse equation can be written as $X^T \sigma^- 1 X = \epsilon$ where:

$$\sigma^{-1} = \begin{bmatrix} \beta & \alpha \\ \alpha & \gamma \end{bmatrix} \quad \sigma = \begin{bmatrix} \beta & -\alpha \\ -\alpha & \gamma \end{bmatrix}$$

IF the equation of the ellipse at point 1 is $X_1^T \sigma_1^{-1} X_1 = \epsilon$ and at point 2 is $X_2^T \sigma_2^{-1} X_2 = \epsilon$, we assumed linear forces the area to be the same (it will be explained in another section). We can write:

$$\sigma_2 = R\sigma_1 R^T$$

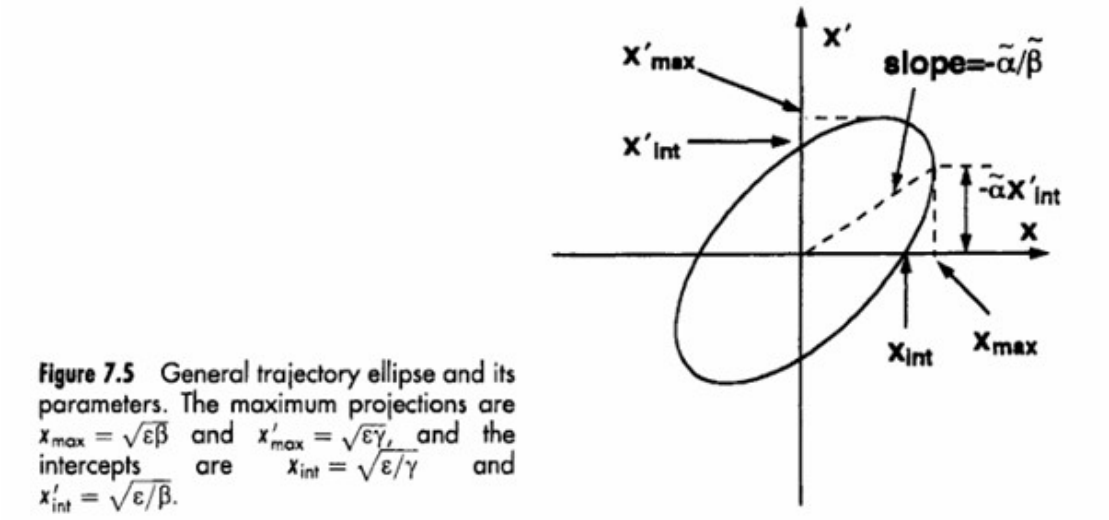


**Figure 7.5** General trajectory ellipse and its parameters. The maximum projections are $x_{max} = \sqrt{\varepsilon\beta}$ and $x'_{max} = \sqrt{\varepsilon\gamma}$, and the intercepts are $x_{int} = \sqrt{\varepsilon/\gamma}$ and $x'_{int} = \sqrt{\varepsilon/\beta}$.

Figure 3.2.1: Ellipse. [1]

Equivalently, the Courant Snyder parameters can be written as:

$$\begin{bmatrix} \beta_2 \\ \alpha_2 \\ \gamma_2 \end{bmatrix} = \begin{bmatrix} R_{11}^2 & -2R_{11}R_{12} & R_{12}^2 \\ -R_{11}R_{21} & 1 + R_{12}R_{21} & -R_{12}R_{22} \\ R_{21}^2 & -2R_{21}R_{22} & R_{22}^2 \end{bmatrix} \begin{bmatrix} \beta_1 \\ \alpha_1 \\ \gamma_1 \end{bmatrix} \tag{3.2.5}$$

where $R_{ij}$ the elements of the transfer matrix. This is valid even when there are space charge forces as long as they are linear.

### 3.2.4 FODO

[7]
Most accelerators have a periodic sequence of quadrupole magnets of alternating polarity and the main goal is to focus the beam to a smaller size while keeping it parallel. An alternating series of focusing and defocusing lenses leads to an overall focusing because the focusing lenses are, on the average, traversed at larger distance from the axis than the defocusing ones.

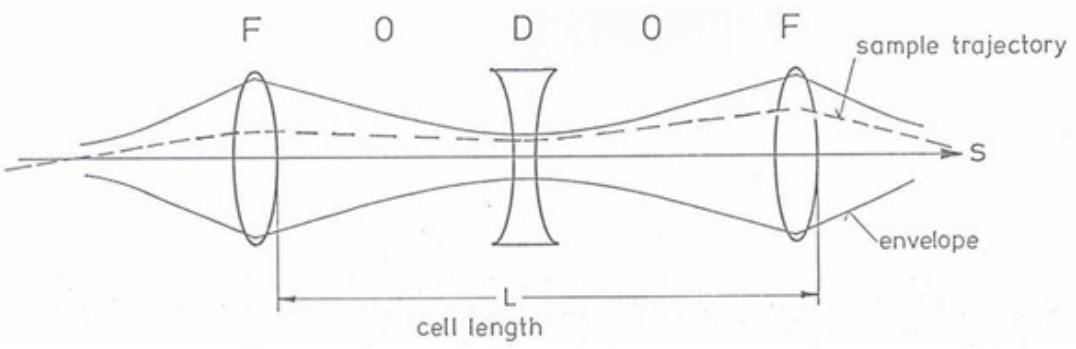


Figure 3.2.2: FODO lens equivalent. [7]

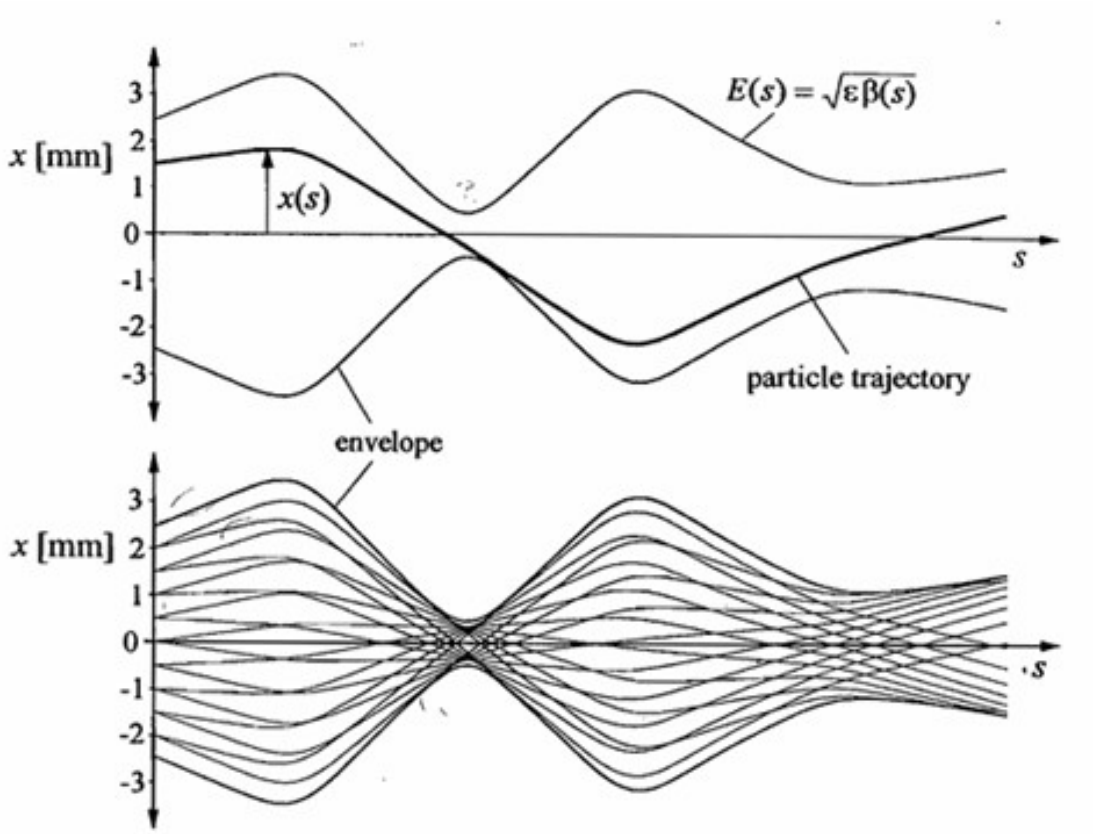


Figure 3.2.3: Particle trajectories [8]

## 3.3 Beam quality

[24] [25] [1]
In a linac, particle motion is dependent not only on applied or external fields, but also on the fields resulting from the Coulomb interactions between the particles and the charges and currents generated by the beam in the surrounding structure's walls. The Coulomb forces play an increasingly important role as the beam current increases. Because the beam density is higher at low velocities in nonrelativistic beams, the Coulomb effects in linacs are typically more significant. In relativistic beams, on the other hand, the self-magnetic forces intensify and partially cancel the electric Coulomb forces. In a linac, a beam bunch consists of particles moving in the same direction, with similar positions, phases, and energies. "Beam quality" refers to how closely these particles match a reference particle's coordinates. The best beam quality, called the laminar beam, represents a highly ordered and coherent beam, though it's never perfect. Instead of directly measuring beam quality, it's more convenient to use a measurable quantity called beam emittance.

### 3.3.1 Emittance

Sources: [1][24]
The beam emittance as a conserved quantity of motion evolves out of the Hamil-

ton formalism and is hence based on canonical coordinates. The square of the emittance RMS can be defined as the determinant of the matrix of second moments of area of the 6-D distribution of the beam. In the transverse plane, $x$ is the position and $x' = p_x/p_z$ the divergence of the beam.

$$\epsilon^2 = det\left(\begin{bmatrix} \bar{x^2} & \bar{xx'} \\ \bar{xx'} & \bar{x'^2} \end{bmatrix}\right) \tag{3.3.1}$$

where:

$$\bar{x^2} = \frac{\int x^2 f(x)dx}{\int f(x)dx} \quad or \quad \bar{x^2} = \frac{\sum x^2}{n} - \left(\frac{\sum x}{n}\right)^2$$
$$\bar{xx'} = \frac{\iint xx' f(x,x')dxdx'}{\iint f(x,x')dxdx'} \quad or \quad \bar{xx'} = \frac{\sum xx'}{n} - \frac{\sum x \sum x'}{n^2}$$

Assuming that the mean value of $x'$ is 0, $\bar{x'^2}$ can be written as

$$\bar{x'^2} = \frac{1}{n}\sum x'^2 = \frac{1}{n}\sum \frac{p_x^2}{p_z^2}$$
$$\epsilon_{tr,rms} = \sqrt{\bar{x^2}\bar{x'^2} - (\bar{xx'})^2} \tag{3.3.2}$$

This is called *trace space emittance*. In the case where we have linear forces (proportional to particle displacement), we assume an elliptical shape, in which it can be derived that the emittance is equal to the area divided by $\pi$: $\epsilon = \frac{\pi ab}{\pi} = ab$ where $a, b$ the semi-major and semi-minor axis lengths of the ellipse.
When taking into consideration the momenta of the particles, we can define the *normalized emittance* as:

$$\epsilon_{n,rms} = \frac{1}{m_0 c}\sqrt{\bar{x^2}\bar{p_x^2} - (\bar{xp_x})^2} \tag{3.3.3}$$

where:

$$\bar{xp_x} = \frac{\sum xp_x}{n} - \frac{\sum x \sum p_x}{n^2} \quad and \quad \bar{p_x^2} = \frac{\sum p_x^2}{n} - \left(\frac{\sum p_x}{n}\right)^2$$

The geometric emittance can be calculated by dividing the normalized emittance by the longitudinal momentum of the particle $p_z$:

$$\epsilon_{rms} = \epsilon_{n,rms}/p_z \tag{3.3.4}$$

The complete normalized trace-space emittance can be defined as:

$$\epsilon_{n,tr,rms} = \frac{\bar{p_z}}{m_0 c}\sqrt{\bar{x^2}\bar{x'^2} - (\bar{xx'})^2} \tag{3.3.5}$$

In the case of elliptical distribution of x,x', the transverse emittance and the normalized emittance $\epsilon_n$ can be written as:

$$\epsilon = \pi \Delta x \Delta x' \quad \epsilon_n = \beta\gamma\epsilon \tag{3.3.6}$$

and has units of $\pi \cdot mm \cdot mrad$ Similarly the longitudinal emittance can be expressed using the energy difference $\Delta W$ and phase difference $\Delta\phi$:

$$\epsilon_l = \Delta W \Delta\phi \quad \epsilon_{nl} = \frac{\Delta W \Delta\phi}{\omega mc} \tag{3.3.7}$$

and has units of $\pi \cdot keV \cdot mrad$

### 3.3.2 Brightness

The brightness of the beam is defined as the current density per solid angle:

$$B = \frac{J}{d\Omega} = \frac{dI}{dSd\Omega} \tag{3.3.8}$$

The average brightness is equal to: $\bar{B} = \frac{I}{V_4}$, where $V_4 = \iint dSd\Omega$ the 4D trace-space Volume.
In the special case in which the trace space volume is defined by a hyperellipsoind, we get $\bar{B} = \frac{2I}{\pi^2 \epsilon_x \epsilon_y}$. Similarly we can also define a normalized brightness as $B_n = \frac{B}{\beta\gamma}$. The normalized emittance and normalized brightness are invariant under ideal conditions in an accelerator.

### 3.3.3 Space Charge

Source [1][26]
The beam consists of many charged particles resulting in the appearance of repulsive forces. The electric field can be derived using Gauss' law:

$$E_r = \frac{q}{\epsilon_0 r} \int_r n(r) r dr \tag{3.3.9}$$

The azimuthial magnetic field can be calculated using Ampere's law:

$$B_\theta = \frac{q\upsilon\mu_0}{r} \int_r n(r) r dr \tag{3.3.10}$$

The radial Lorenz force is equal to:

$$F_r = q(E_r - \upsilon B_\theta) = qE_r/\gamma^2 \tag{3.3.11}$$

From eq3.3.11 it is noticeable that the space charge effects are a non relativistic phenomenon and in the case of an electron linacs, those froces are of great importance at injection.

For reference, if we consider a cylindrical beam with N particles per unit length and radius $a$, utilizing the formulae above, the following cases can be derived:

- for $r > a$:

$$E = \frac{eN}{2\pi\epsilon_0 r} \tag{3.3.12}$$

$$B = \frac{eN\upsilon}{2\pi\epsilon_0 r c^2} \tag{3.3.13}$$

- for $r < a$:

$$E = \frac{eN}{2\pi\epsilon_0 a^2} r \tag{3.3.14}$$

$$B = \frac{eN\upsilon}{2\pi\epsilon_0 a^2 c^2} r \tag{3.3.15}$$

From eqs 3.3.12 and 3.3.13, the net outward force is calculated to be:

$$F = \frac{e^2 N}{2\pi\epsilon_0 r\gamma^2} \tag{3.3.16}$$

and similarly form eqs 3.3.14 and3.3.15, the net force from the space charge to the particles is:

$$F = \frac{e^2 N}{2\pi\epsilon_0 a^2\gamma^2} r \tag{3.3.17}$$

Inside the beam, the linear dependence of the force in the transverse plane is similar to a defocusing lens. Now the equation of motion 2.3.2 can be rewritten as:

$$\ddot{x} + K(s)x = \frac{1}{\gamma m \upsilon^2} * (sp\_charge)$$

$$\ddot{x} + \left[K(s) - \frac{2r_0 N}{\beta^2\gamma^3 a^2}\right] x = 0 \tag{3.3.18}$$

Where $r_0 = \frac{e^2}{4\pi\epsilon_0 mc^2}$ the classical radius of the particle.

# 4 Ionizing radiation

Ionizing radiation is present everywhere in our environment and it is a fundamental aspect of nature. It is emitted naturally from both terrestrial (from rocks, soil, etc) and celestial sources (sun, cosmic radiation, etc) and man made sources. Living organisms have always been exposed to natural sources of radiation. Man-made radiation exposure to populations occurs mainly from medical uses of radiation and radioisotopes in health care, occupational sources in the generation of electricity from nuclear power reactors, industrial uses of nuclear techniques, and in the past from nuclear weapons testing.

## 4.1 Interactions of radiation with matter

Sources: [9] [27]

Ionizing radiation can be categorized as directly or indirectly ionizing for the understanding of biological effects. Particulate types of radiation usually have adequate kinetic energy that can directly disrupt the atomic structure by ripping electrons and causing chemical or biological damage to the molecules. Electromagnetic radiation, on the other hand, interact indirectly by producing secondary electrons after energy absorption in the material.
Ionization is the process of removing one or more electrons from atoms by the incident radiation leaving behind electrically charged particles (an electron and a positively charged ion) which may subsequently produce significant biological effects in the irradiated material. Either the excited or ionized atom or molecule will break apart and release free radicals, or it will revert to its original form.

### 4.1.1 Electromagnetic radiation

Radio-waves, microwaves, visible light, ultraviolet light, X-rays, and $\gamma$ -rays are all forms of electromagnetic radiation and their energy is essentially what defines them. Radiations with longer wavelengths (lower frequency) have lower energy ($E = hf$) than that needed to remove electrons from atoms, thus are called *non-ionizing*. They are usually considered harmless to biological tissues at levels that are not high enough to cause heating effects, because they are not known to cause significant chemical changes in atoms or molecules of the medium. However, since some molecules can ionize with small amounts of energy and far UV radiation can have similar behavior to X and $\gamma$ rays, the precise boundary between ionizing and non-ionizing radiation regions of the spectrum is somewhat arbitrary.

When electromagnetic radiation passes through a material, it can do so without transferring any energy, or it can interact with the material decreasing its intensity. The attenuation is caused by specific photon interactions with the encountered atoms. For a monoenergetic beam of photons, a constant fraction decreases as the beam travels through each unit of thickness in the absorber. This results in an

exponential decrease of the intensity given by the following equation:

$$I(x) = I_0 e^{-\mu x}$$

where $I(x)$ the intensity at depth $x$ and the absorption coefficient $\mu = \sigma n$ is equal to the absorption cross section multiplied by the number of atoms per unit volume. Electromagnetic radiations (primarily X- or $\gamma$-rays) can have biological effects when they scatter or absorb energy from atoms within tissues or organs. When ionizing radiation interacts with an organism or tissue and leaves some energy behind, biological effects of radiation occur. Photon energy and the atomic number of the material they absorb determine how they are absorbed in matter (Figure 4.1.1). Photons passing through matter transfer their energy through the following three main processes:

- **Photoelectric effect**
  Photons interact with bound inner shell electrons, transferring their entire energy ejecting the electron from the atom.

$$K_{electron} = hf - E_{binding}$$

- **Compton scattering**
  Photons interact with the outer electrons transferring some of their energy to eject the electron and a photon with the remaining energy is scattered in a different direction.
- **Pair production**
  When a high energy photon ($> 1.022MeV$) interacts with the medium, it can be spontaneously be converted to the mass of an electron-positron pair ($m_e = 511keV/c^2$). The positron will soon combine with another free electron, converting all of their energy into two $\gamma$ photons of energy $511keV$ in opposite directions.

### 4.1.2 Particulate radiation

Particulate radiation refers to particles like alpha and beta particles (electrons), protons, neutrons, and ions that can cause ionization. It can either be direct ionization, excitation or nuclear reactions. The rate of energy loss or stopping power caused by ionization interactions for heavy charged particles is proportional to the square of the particle charge and inversely proportional to the square of its velocity (eq. 4.1.1). Thus, as the particle slows down, its rate of energy loss increases and so does the ionization or absorbed dose to the medium. As shown in Figure 4.1.2, the dose deposited increases gradually with depth and then rises sharply near the end of the particle's range, before rapidly dropping to nearly zero. This sharp increase in dose near the end of the range is known as the Bragg peak.

Heavy charged particles (protons, alpha particles etc), interact with matter primarily through Coulomb interactions between their positive charge and the negative charge of the orbital electrons within the medium. Those electrons can either become excited or leave the atom (ionization), potentially causing further (secondary) ionizations if they have enough energy. Due to their mass being a

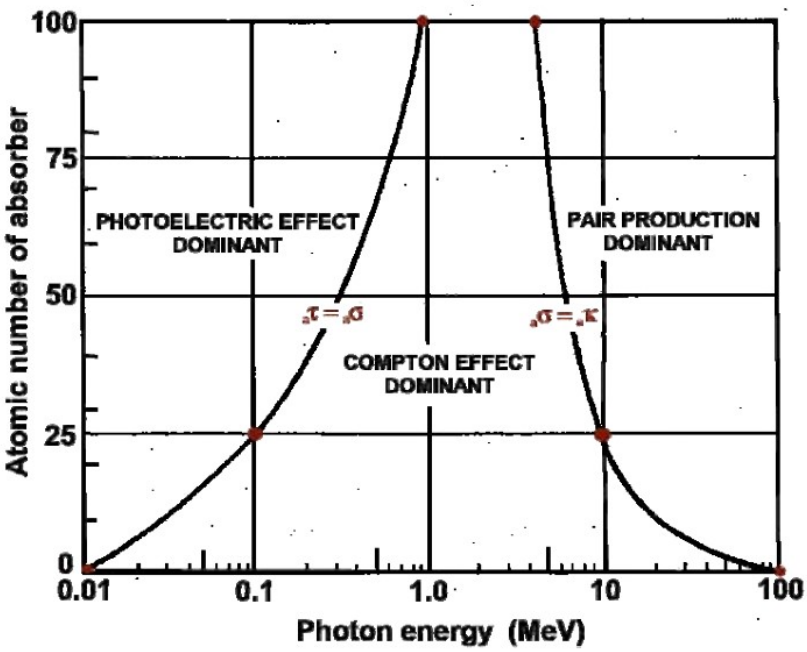


Figure 4.1.1: Dominant types of interaction as a function of the atomic number of the absorber and photon energy [9]

lot bigger than that of electrons, their tracks are quite straight, except at the end of the path where deflections can occur because of the low momentum, a process called 'straggling'. Range straggling is a stochastic process in which particles of the beam may have slightly different total path lengths. [27][28]

$$-\frac{dE}{dx} = 4\pi r_0^2 z^2 \frac{m_e c^2}{\beta^2} NZ \left[ \ln\left( \frac{2m_e c^2}{I} \beta^2 \gamma^2 \right) - \beta^2 \right] \tag{4.1.1}$$

Eq. 4.1.1 is the Bethe-Bloch formula for ions of charge $z$ travelling at a speed $\beta = v/c$. The quantity $r_0 = e^2/(4\pi\epsilon_0 mc^2)$ is the classical radius of the particle (2.818fm for electrons, $1.53 \cdot 10^{-3} fm$ for protons), $N$ is the density of the target, $Z$ is the atomic number of the target and $I$ is the mean ionization potential. It can easily be seen through this equation that $\alpha$ particles can cause more damage than protons for instance and deliver their energy as seen on the Bragg curves (fig. 4.1.2).

Because of the Bragg peak effect and minimal scattering, proton and ion beams have the ability to focus the dose within the target volume while minimizing exposure to surrounding healthy tissues, which is a great advantage. [27]

### 4.1.3 Production of X-rays

Source [11]

X-rays were discovered by Wilhelm Roentgen in 1895, have wavelenghts between $10pm - 10nm$ and lay between $\gamma$ rays and UV. They are widely utilized for their ability to penetrate matter, producing detailed images of internal structures

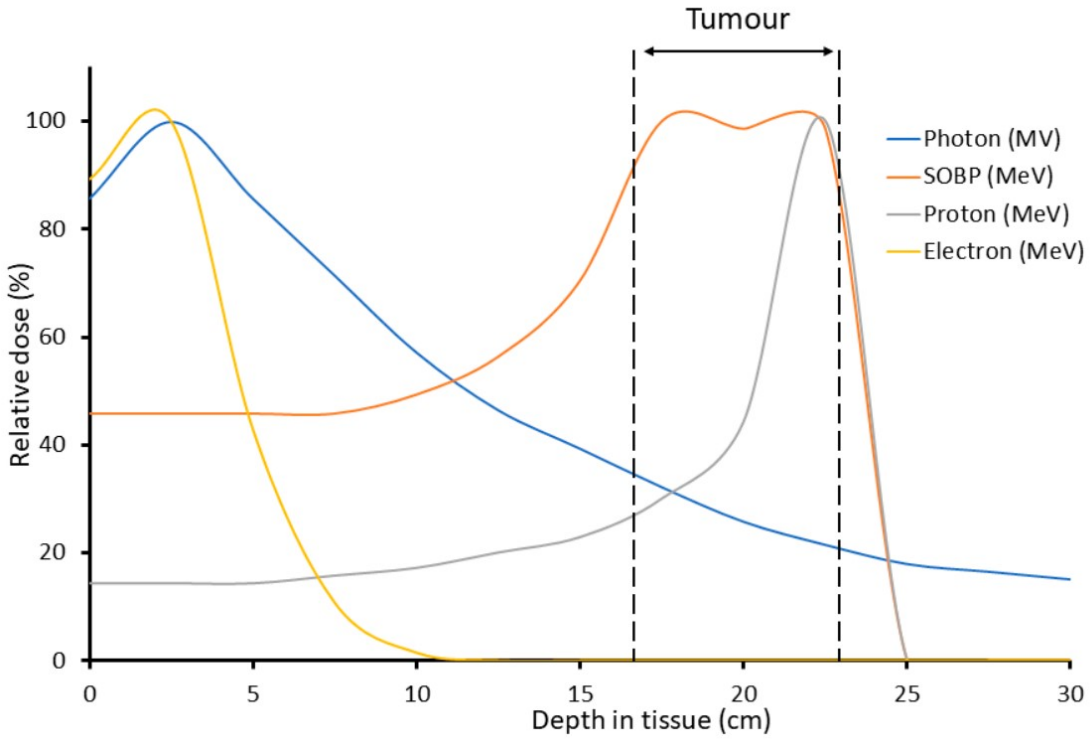


Figure 4.1.2: Depth-Dose distribution of protons, photons, electrons relative to a tumor target [10]

(broken bones etc) and for their ionizing nature, which can destroy cancerous cells, thereby providing significant therapeutic benefits.

X-rays are usually generated by converting the kinetic energy of accelerated electrons to electromagnetic radiation. An X-ray tube and X-ray generator are essential components for producing and controlling X-rays. The x-ray generator consists of the electronics (computer, high and low voltage transformers). The x-ray tube consists filament which is powered by the low voltage transformer produces free electrons by the process of thermionic emission (as described in a previous section). The electrons are accelerated by a potential difference between the anode and cathode, the voltage is provided by the high voltage transformer. The anode is also the target of the electrons and it is made of metals like Tungsten (W) as shown in figure 4.1.3. Upon hitting the target, the energy is lost as the electrons interact with the fields close to the nucleus. In certain occasions, when an electron is ejected from its orbit (K,L...), another electron will drop to that level emitting a characteristic x-ray. In the rare case when an electron falls directly at the nucleus, the emitted x-ray has the most energy (figure 4.1.4).

## 4.2 Fast electrons

[28]
Fast electrons lose their energy at a lower rate compared to heavy charged particles.

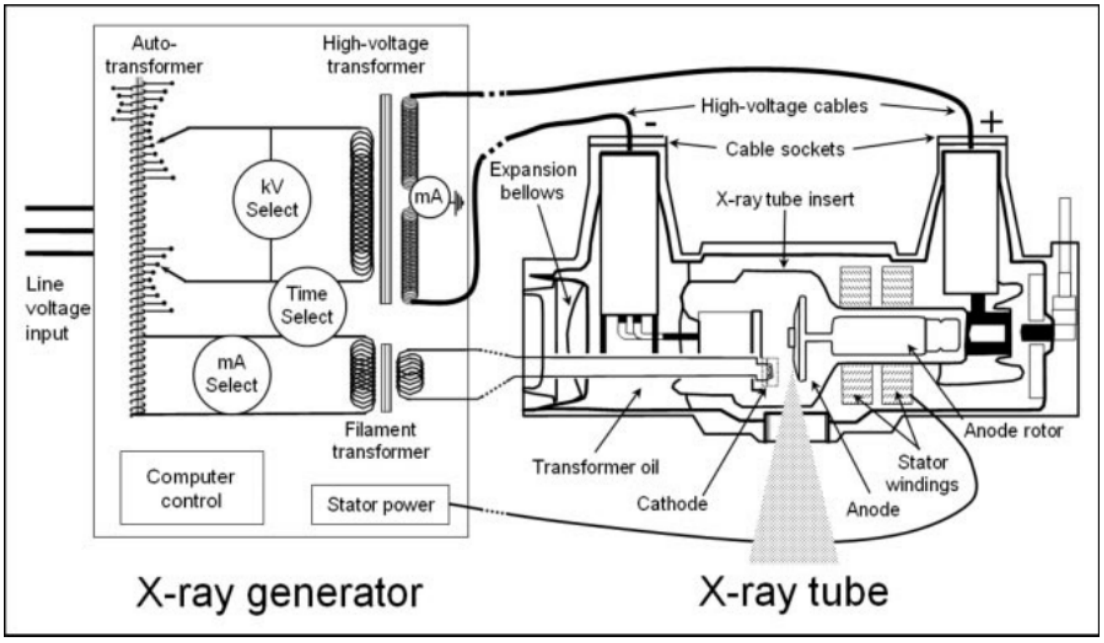


Figure 4.1.3: Device [11]

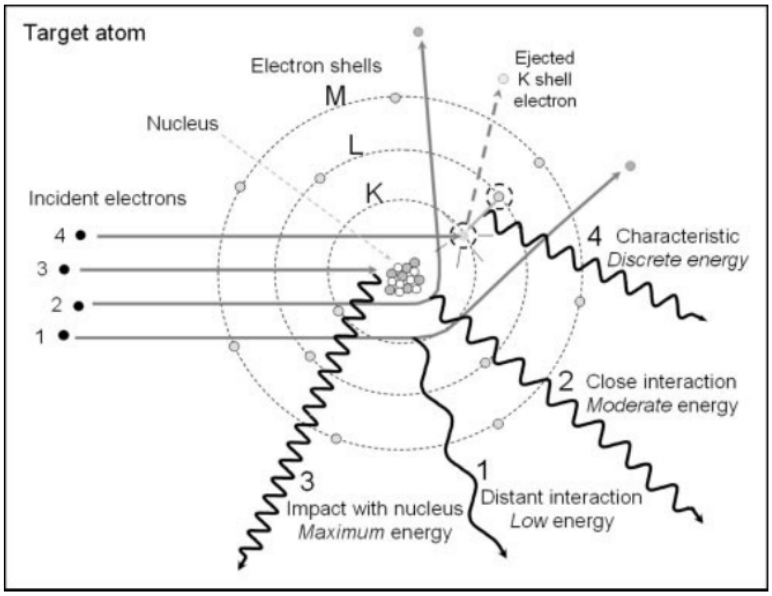


Figure 4.1.4: [11]

The path of electrons may have large deviations due to the fact that their mass is equal to that of orbital electrons in the target, which means that a lot of energy can be lost in a single encounter. Additionally, electrons can interact with the nucleus, which can abruptly change the electron direction.
Energy losses can be due to ionization and excitation (collisional losses) and is

described by the Bethe formula:

$$-\left(\frac{dE}{dx}\right)_c = \frac{2\pi e^4 NZ}{mv^2}\left[\ln\frac{mv^2E}{2I^2(1-\beta^2)} - \left(2\sqrt{1-\beta^2} - 1 + \beta^2\right)\ln 2 + \right.$$
$$\left. + (1-\beta^2) + \frac{1}{8}\left(1-\sqrt{1-\beta^2}\right)^2\right] \quad (4.2.1)$$

Electrons have smaller mass and move faster than heavy charged particles, which means that radiative losses due to bremsstrahlung or electromagnetic radiation which can emanate form any position along the electron track. When accelerated, any charge must radiate, and in this case electrons deflecting are being accelerated. The losses can be described by:

$$-\left(\frac{dE}{dx}\right)_r = \frac{NEZ(Z+1)e^4}{137m^2c^4}\left(4\ln\frac{2E}{mc^2} - \frac{4}{3}\right) \quad (4.2.2)$$

As seen from the presence of $m^2$, heavy charged particles have negligible radiative losses and from the factors $E$ and $Z^2$ show that radiative losses are more important for high energy electrons and for large atomic number materials in the absorber. The total linear stopping power for electrons is the sum of radiative and collisional losses:

$$\frac{dE}{dx} = \left(\frac{dE}{dx}\right)_r + \left(\frac{dE}{dx}\right)_c \quad (4.2.3)$$

The ratio of the specific energy losses can be approximated by:

$$\frac{(dE/dx)_r}{(dE/dx)_c} \cong \frac{EZ}{700} \quad (4.2.4)$$

Where $E$ is expressed in MeV

### 4.2.1 Depth-Dose curve

[29]
Typically, an electron beam exhibits a relatively high surface dose, which will build up to a maximum dose at a certain depth $z_{max}$, called the “electron depth dose maximum”. After reaching its peak, the dose decreases quickly and then stabilizes at a lower level, characterized by a minor residual dose component known as the "bremsstrahlung tail".
As electrons travel through a medium, they engage in Coulomb force interactions with atoms, which encompass various processes. These interactions include inelastic collisions with atomic electrons leading to ionization and excitation of atoms, known as collisional or ionization loss, as well as inelastic collisions with nuclei resulting in the production of bremsstrahlung radiation, termed radiative loss. Additionally, elastic collisions with atomic electrons and nuclei occur, characterized by changes in direction but no energy loss. In inelastic collisions, the kinetic energy is converted to excitation energy or photon energy.
The energy loss rate in collisional interactions depends on both the electron’s energy and the electron density of the medium. The rate of energy loss per unit mass

and area (referred to as mass stopping power) is higher in materials with lower atomic numbers compared to those with higher atomic numbers. This is because low atomic number materials have more electrons per unit mass and fewer tightly bound electrons unavailable for interaction. For therapy electron beams passing through tissue, the average energy loss is typically around 2 $MeVcm^2/g$ .
In contrast, the energy loss rate in radiative interactions (bremsstrahlung) is roughly proportional to the electron's energy and the square of the atomic number of the absorber. Consequently, x-ray production from radiative losses is more efficient with higher energy electrons and higher atomic number materials.
When electron beams traverse a medium, they undergo multiple scattering due to Coulomb force interactions with the medium's nuclei. This scattering causes the electrons to acquire transverse velocity components and displacements from their original path. As the electron beam travels through a patient, its average energy decreases, and its angular spread increases.
The scattering power of electrons is approximately proportional to the square of the atomic number and inversely proportional to the square of the kinetic energy. Thus, high atomic number materials are utilized in constructing scattering foils for generating clinical electron beams in linear accelerators.

### 4.2.2 Range

[29]
Interactions of electrons with each atom decreases the energy by a very small fraction. Conveniently it can be assumed that kinetic energy is lost gradually and continuously (continuous slowing down approximation - csda). We can define the **path length** of a single electron as the total distance travelled until it comes to rest, regardless of the direction of movement. The csda range (mean path-length) for an electron of initial kinetic energy $E_0$ can be found by:

$$R_{csda} = \int_0^{E_0} \left( \frac{S(E)}{\rho} \right)^{-1} dE \tag{4.2.5}$$

where $S(E)$ the stopping power.

**CSDA Range**
The concept of CSDA range reflects the average path length traveled by electrons rather than indicating their depth of penetration in a specific direction. While tables may provide CSDA ranges for electrons at different kinetic energies in air and water, they offer little practical value in characterizing electron penetration depth into absorbing materials. This is primarily because electron trajectories become highly erratic due to scattering effects, arising from interactions with both the nuclei and orbital electrons of the absorptive medium. Consequently, the actual depth of electron penetration exhibits considerable variation.

**Maximum Range** It is defined as the depth at which extrapolation o f the tail of the central-axis depth dose curve meets the bremsstrahlung background and is the largest penetration depth of electrons in the absorbing medium.

**Practical Range** It is defined as the depth at which the tangent plotted

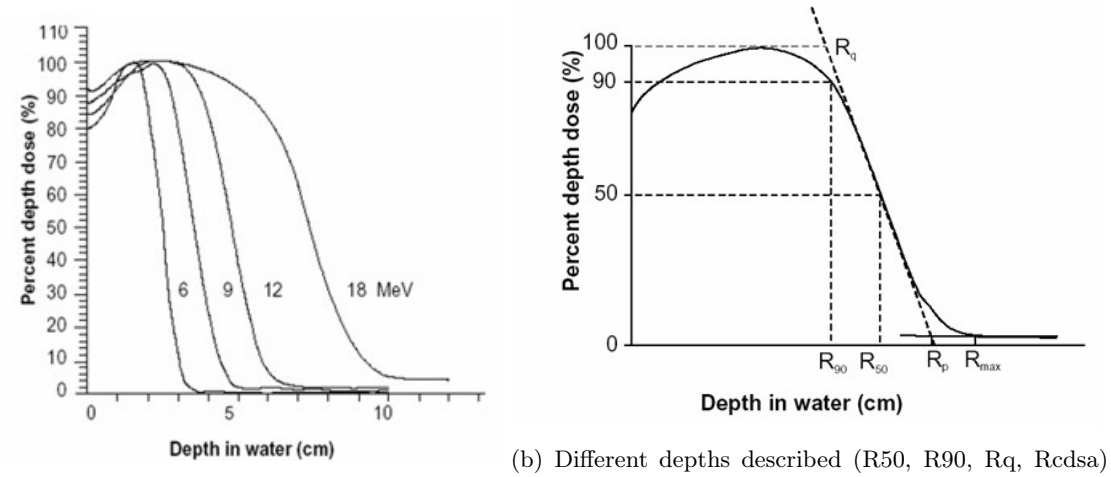


(a) Range of electrons for different energies [29] [29]

(b) Different depths described (R50, R90, Rq, Rcdsa)

Figure 4.2.1: Electron range in water

through the steepest section of the electron depth dose curve intersects with the extrapolation line of the background due to bremsstrahlung.

**Depths R90, R50, Rq**

The depths R90 and R50 are the depths above $z_{max}$ at which the dose is 90% and 50% respectively and Rq is the depth at which the tangent through the inflection point intersects the maximum dose level.

**Build up region**

When entering the absorbing medium, the electrons move initially in parallel paths and then they tend to change their direction due to multiple scattering. Upon collision with atomic electrons, the energy of the ejected electron might be large enough to cause further ionisation. Those electrons are referred to as secondary electrons or $\delta-$ rays and contribute to the build up of the dose.

When hitting a target, the surface dose is relatively high $75-95\%$ and increases to 100% at a distance $z_{max}$. The percent surface dose increases with electron energy, which can be explained by the nature of electron scattering. For example, at low energies, electrons are scattered at larger angles and subsequently the dose builds up closer to the surface.

**Dose distribution beyond $z_{max}$**

Beyond $z_{max}$, the electron dose experiences a rapid decline attributed to scattering and continuous energy dissipation. The trailing end is characterized by bremsstrahlung generation occurring within the accelerator head, within the air gap between the accelerator window and the patient, and within the irradiated medium.

## 4.3 Radiation Dose Metrics and Biological Impact

### 4.3.1 Radiation dose and units

[9] Ionizing radiation can cause events that cause damage in tissues. Exposure to radiation or the absorbed radiation can be measured as follows:

**Exposure:**
Radiation exposure measures the ability of radiation to produce ionization in the air at standard temperature and pressure conditions. It is measured with radiation detectors, such as ionization chambers (e.g., Geiger-Muller counters).

**Absorbed dose:**
Radiation dose is defined as the energy absorbed per unit mass of tissue and has units of gray ($1Gy = 1J/kg$). In the past, the unit $rad$ (radiation absorbed dose) was used ($1Gy = 100rad$).

**Equivalent dose:**
The term 'equivalent dose' is used to compare the biological effectiveness of different types of radiation to tissues and it is important when discussing about radiation protection. The dose equivalent ($H_T$) is measured in *Sieverts* ($Sv$), and is the product of absorbed dose and a radiation weighting factor $W_R$. Specifically for low LET radiations, the weighting factor is equal to 1 and $1Sv = 1Gy$.

$$H_T = \sum W_R D_T \tag{4.3.1}$$

**Effective dose:**
The effective dose is used to estimate the risk of radiation in humans. It is calculated by multiplying the equivalent dose with a tissue weighting factor $W_T$, which differs per tissue or organ. The sum $\sum W_T = 1$ for whole body radiation.

$$E = \sum W_T H_T \tag{4.3.2}$$

### 4.3.2 Basic parameters for radiotherapy

Source: [9] In Radiobiology there are some basic parameters that describe the effectiveness and impact of radiation on a tissue.

**RBE (Relative Biological Effectiveness)**
Different types of radiation cause different biological effects. RBE compares other types of radiation with a reference dose, which historically used to be the effect of 250kVp X-rays, but now it is mostly that of >1MeV photons produced from Co-60. The ratio of the reference dose divided by the tested dose needed to produce an equal biological effect is the definition of RBE.

$$RBE = \left.\frac{D_{ref}}{D_{test}}\right|_{equal-biological-effect} \tag{4.3.3}$$

**LET (Linear Energy Transfer)**
When ionizing radiations traverse though matter, they lose their energy through different mechanisms. The rate of loss of energy is dependent on the material and its density, as well as the radiation type and its energy. The energy loss per unit length in a material (such as tissue) is defined as Linear Energy Transfer (LET) $-dE/dx$ and its unit is $keV/\mu m$. LET essentially indicates the quality of different types of radiation and it is important, because the relative biological effectiveness (RBE) is dependent on the average LET. The LET varies along the track of charged particles as they slow down. Radiations can be categorized as high or low LET. Particulate radiations have high LET as the energy loss events are more closely spaced, but X- and $\gamma$-rays have low LET due to their sparse ionizations. Specifically for heavy charged particles the LET increases as their energy decreases, forming the characteristic Bragg peak. The RBE of a radiation increases for higher values of LET up to a value of $100keV/\mu m$, above which RBE decreases because more energy is deposited than that needed to cause biological effect (overkill).

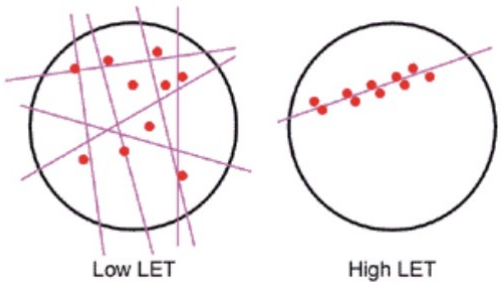


Figure 4.3.1: Difference between high and low LET radiations Web Source

**OER Oxygen Enhancement Ratio**
Radiosensitivity is dependent on oxygen levels in a tissue. More specifically, hypoxic tissues are more resistant to radiation than oxygenated ones. By using the effect on hypoxic tissues as a reference, OER can be defined as the ratio of the dose on the hypoxic divided by dose needed by the oxygenated tissue in order to have the same biological effect.

$$OER = \frac{D_{ref-hypoxic}}{D_{test-oxygenated}}\bigg|_{equal-biological-effect} \tag{4.3.4}$$

Tumors are often hypoxic, meaning they have low oxygen levels. This hypoxia makes them more resistant to radiation, making radiotherapy more difficult.

### 4.3.3 Direct and indirect effects of radiation

Sources [9] [32]
**Direct effects:**
Ionizing radiation can directly interfere with biological molecules by directly disrupting their structure through ionization or excitation. Those changes will damage or lead to cell death. Chemical bonds can be broken, leaving atoms or

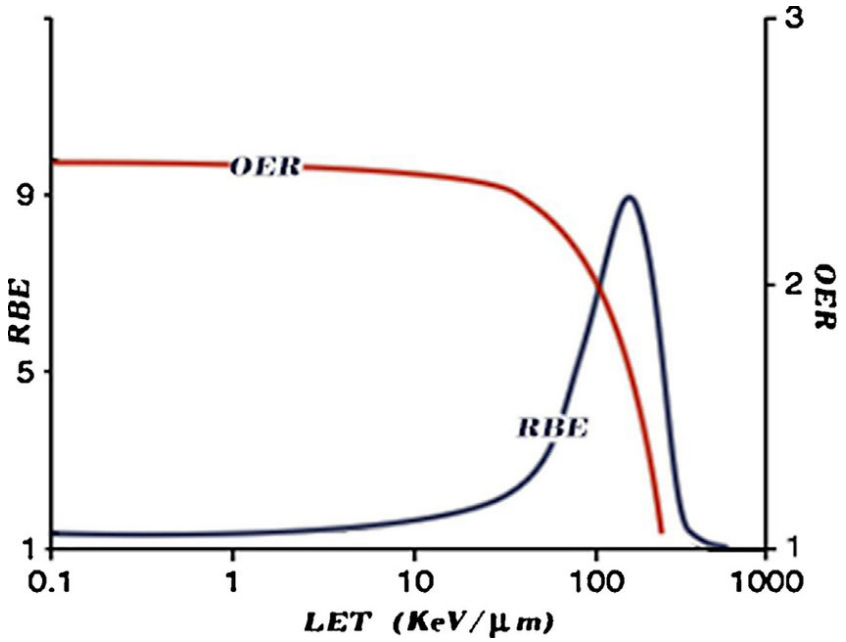


Figure 4.3.2: OER and RBE as a function of LET [12]

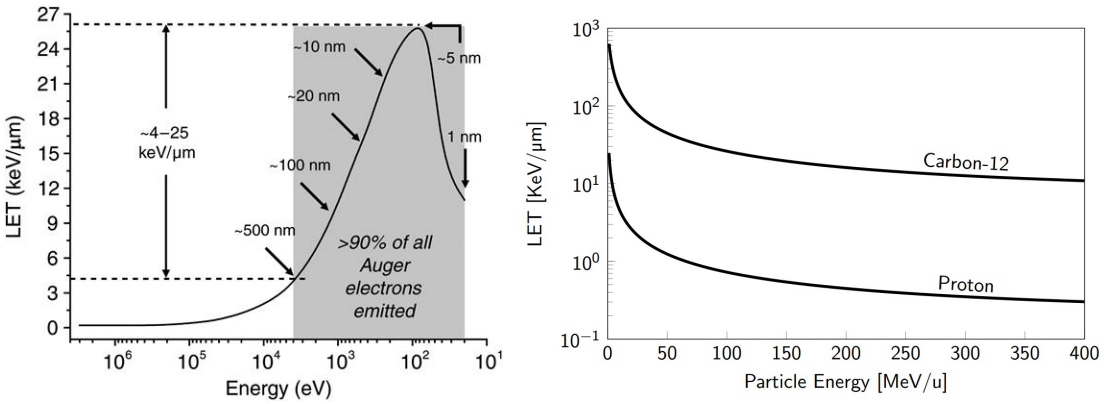


(a) Electron LET, arrows indicate the range at that energy. [30]

(b) LET of protons and carbon ions in the MeV range [31]

Figure 4.3.3: LET of particles as a function of their energy

molecules with unpaired electrons behind, that are very reactive and have a short lifetime. The time range of these reactions is around the pico-second scale and the free radicals can either be repaired, bond with oxygen or cross-link with other radicals. This process is more dominant with high LET radiation.

$$\mathrm{RH} \xrightarrow{\text{irradiation}} \mathrm{R}\bullet + \mathrm{H}\bullet$$

where RH could be a DNA molecule and cross-link reactions can occur:

$$\mathrm{R_1}\bullet + \mathrm{R_2}\bullet \rightarrow \mathrm{R_1} - \mathrm{R_2}$$

**Indirect effects – Water radiolysis**
Ionizing radiation can react with water to produce free radicals as well. Through

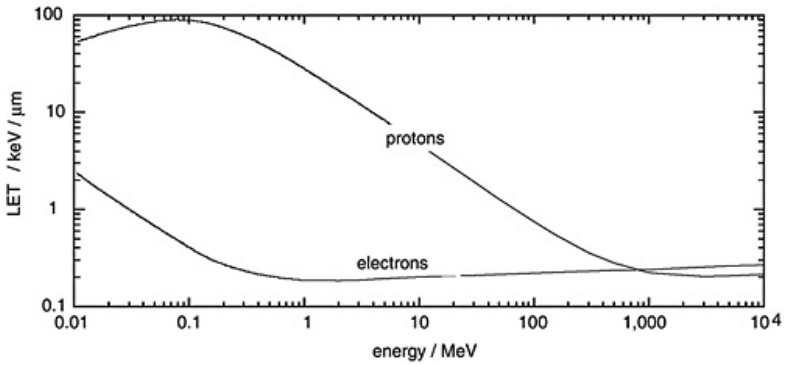


Figure 4.3.4: Comparison of Proton and Electron LET [13]

radiolysis, water is decomposed to $H^*$ and $OH^*$ radicals via excitation, or to $H_2O^+ + e^-$ via ionization. Indirect effects are dominant in low LET radiation.

$$\mathrm{H_2O} \xrightarrow{\text{excitation}} \mathrm{H\bullet + OH\bullet}$$

$$\mathrm{H_2O} \xrightarrow{\text{ionization}} \mathrm{H_2O^+ + e^-}$$

$H_2O^+$ decomposes as:

$$\mathrm{H_2O^+ \rightarrow H^+ + OH\bullet}$$

The electron will react in the following ways:

$$\mathrm{e^- \xrightarrow{+H_2O} H_2O^- \rightarrow H\bullet + OH^-}$$

$$\mathrm{e^- \xrightarrow{+H^+} H\bullet}$$

$$\mathrm{e^- \xrightarrow{+H_2O} e^-_{aq}}$$

Those free radicals can react with a DNA molecule and induce damage.

### 4.3.4 DNA damage and repair

sources [9][33]
The primary types of DNA damage are the following:

- **Single Strand Breaks (SSB)**
  It happens when the phosphate-deoxyribose backbone of one strand of the DNA double helix is damaged due to oxidative stress or ionizing radiation. They are usually repaired by the base excision repair (BER) pathway. The presence of the complimentary strand, which is not affected, makes the repair easy and efficient. Thus SSBs are not considered lethal.
- **Double Strand Breaks (DSB)**
  A double strand break occurs when both strands break in close proximity and they are considered one of the most lethal types of DNA damage. They are usually repaired by non-homologous end joining (NHEJ), which is quick but error-prone, and homologous recombination (HR) which occurs during certain phases of the cell cycle (G2/S-phases) and is more accurate. Failure in repairing DSBs can lead to mutations.

- **Base Damage**
  DNA consists of 4 bases that "store" genetic information (adenine (A), thymine (T), cytosine (C), and guanine (G)). Alteration of the sequence, absence or damage to the structure of those bases can lead to malfunctions and mutations. They are repaired by nucleotide excesion repair (NER) or (BER) that recognise and replace the damaged bases with the correct nucleodites.
- **Cross-Linking**
  It is the formation of bonds between DNA strands, or even other proteins (for instance, histones). They prevent the separation of DNA strands, blocking replication and transcription. The repair is complex and challenging and it is usually done with HR or NER.

The repair mechanisms are explained described in detail below:

- **Base Excision Repair (BER)**
  This mechanism repairs small lesions initially by removing the damaged base, which is recognised by DNA glycosylase enzymes. Using the complementary strand as a template, DNA polymerase fills the gap with the correct nucleotide and DNA ligase fixes the sugar-phosphate backbone.
- **Nucleotide Excision Repair (NER)**
  NER repairs bigger lesions that distort the helix. Once the damage is recognised, a short single strand part of the helix that contains the damage is removed (excision) by enzymes. The missing strand is synthesized and sealed as previously described in BER.
- **Mismatch Repair (MMR)**
  MMR corrects mismaches that occur during DNA replication. Proteins (like MutS) recognise the mismatch, the area around the mismatch is removed and replaced by a newly synthesized strand with the correcr nucleotides.
- **Homologous Recombination (HR)**
  In HR, a DNA template (sister chromatid) is used to repair bulky lesions like DSBs. It is very accurate, but it can occur only when a sister chromatid is available, which is right after DNA replication.
- **Non-Homologous End Joining (NHEJ)**
  NHEJ repairs DSBs when no sister chromatid is available. The broken ends are merged together, but during this process the ends might be trimmed or new nucleotides can be added to make both ends compatable. It is less accurate than HR, but faster and it is useful when the cell is not dividing.
- **Translesion Synthesis (TLS)**
  TLS is a mechanism that tolerates DNA damage and allows replication to continue ignoring lesions that could slow down or even terminate the replication process and lead to cell death. Once the replicaton fork stalls at a lesion, the DNA polymerase is temporarily replaced by the TLS polymerase that bypasses the lesion. It is less accurate and prone to errors.

### 4.3.5 Survival curves

One model used to simulate DNA damage is the Linear-Quadratic (LQ) model. This model represents the survival fraction as a function of the absorbed dose and it can be expressed through the following equation:

$$-\ln SF = \alpha D + \beta D^2 \tag{4.3.5}$$

where $\alpha$ and $\beta$ are constants that describe the decline of survival with increasing dose. For high LET radiation, $\beta$ is negligible.

## 4.4 FLASH Radiotherapy

Radiotherapy is a widely used and effective method for treating cancer. By using radiation that include particles like electrons, protons and ions, or electromagnetic radiation (X- or $\gamma$- rays), tumors are eradicated. However, one of its major challenges is that while targeting the tumor, surrounding healthy tissues are also exposed to radiation, potentially leading to complications. Ongoing research has demonstrated that increasing the dose rate from conventional levels - (CONV-RT) (typically less than 0.1 Gy/s) to Ultra High Dose Rates (UHDR) exceeding 40 Gy/s (FLASH-RT) can significantly enhance the sparing of normal tissues. [10]

### 4.4.1 FLASH effect

Early evidence of the FLASH effect was demonstrated by Dewey and Boag in 1959, when they irradiated bacteria with X-rays in oxygenated and hypoxic environments, with high and low dose rates. Conventionally, the oxygenated bacteria are more sensitive to radiation, but when they were irradiated with FLASH, they were protected [14]. Many decades later (2014), Favaudon reported that using FLASH-RT for lung tumour treatment can result in a complete response and significantly reduce both early and late toxicity to normal lung tissue. Since then, FLASH-RT has garnered significant interest in the field of radiation research [34]. In general, as shown in Figure 4.4.1, FLASH is shown to have similar antitumour effects, but is more efficient in sparing normal tissues.

### 4.4.2 Potential mechanisms for FLASH

The reason why normal cells are spared when irradiated with UHDR radiation, is not well known. Many hypotheses have been proposed including the following: [35]

**Radiolytic Oxygen Depletion** Studies have shown that when a tissue is irradiated with UHDR radiation, the oxygen levels are rapidly reduced, causing the irradiated cells to temporarily become hypoxic and more radio-resistant. Other studies in which oxygen levels were directly measured, concluded that no total oxygen depletion was observed. Thus, this hypothesis alone is not adequate to explain the FLASH effect. Instead, a reduction in oxygen consumption has been observed at higher dose rates, which is associated with lower steady-state levels of electron radicals [36]. There is also a hypothesis that FLASH irradiation reduces oxygen

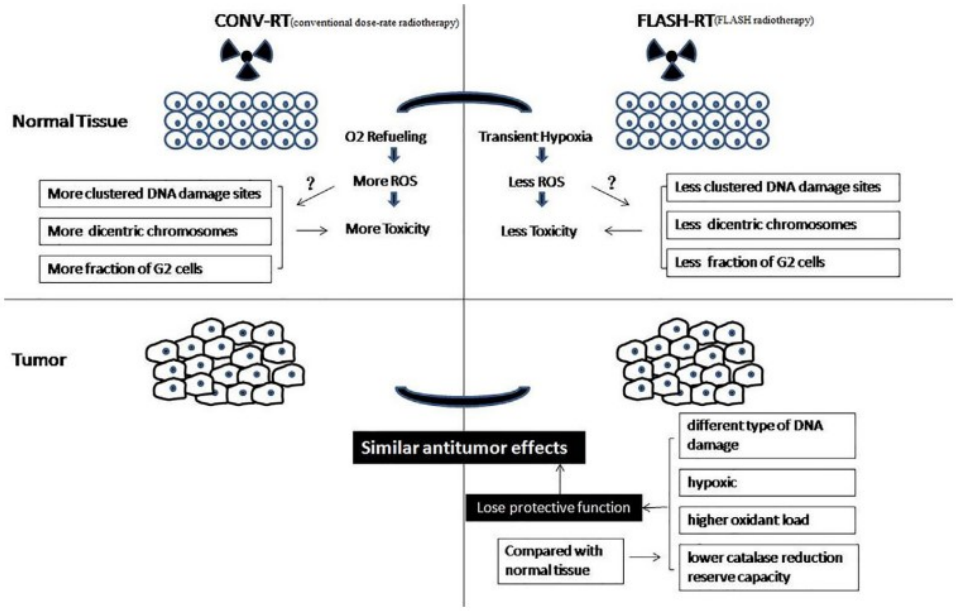


Figure 4.4.1: FLASH effect [14]

levels to stem cell niches, providing radioprotection. Preserving stem cells is very important, since they are responsible for tissue regeneration [37].

**The role of Reactive Oxygen Spieces** When cells are exposed to FLASH radiation, less free radicals are produced. Cells are now less sensitive to radiation, as described in a previous section. In conventional RT, lipids contribute a lot to the production of ROS, but in the case of FLASH, the dose is delivered quickly, reducing the lipid peroxidation and sustaining normal cells. Another source of ROS is the fenton reaction:

$$Fe^{2+} + H_2O_2 \rightarrow Fe^{3+} + OH^- + \cdot OH$$

Normal tissues can regulate the amount of liable (readily available) Fe, in comparison to cancerous cells, thus reducing the damage in normal cells. In addition to that, normal tissues have mechanisms (enzymatic) that remove ROS more efficiently than in tumours [38].

**Immune sparing hypothesis** Lymphocytes and other circulating blood cells are exposed for a very short amount of time (<1sec) with FLASH, in comparison to conventional methods in which the organism is exposed for a few minutes. As a result, smaller percentage of healthy circulating cells are preserved, and potentially reducing the odds of common side effects related to radiotherapy like lymphopenia[39].

# 5 Simulations

## 5.1 ASTRA software

The ASTRA software (**A S**pace-charge **TR**acking **A**lgorithm) consists of the programs:

- *Generator* that is used to generate the initial beam
- *ASTRA* which tracks the particles under the influence of electric and magnetic fields.

The package also comes with three graphic programs:

- *Lineplot*: used to display the beam size, emittance, bunch length etc. versus the longitudinal beam line position
- *Fieldplot*: used to display electromagnetic fields ofbeam line elements and space charge fields of particle distributions
- *PostPro*: used to display phase space plots of particle distributions and allows a detailed analysis of the phase space distribution

The simulation manual and the software are available online [40]

### 5.1.1 Generator

This program is used to generate an initial beam distribution. An example is written below.

```
&INPUT
FNAME = 'rfgun.ini'
Add=FALSE,
N_add=0,
IPart=3000,
Species='electrons'
Probe=True,
Noise_reduc=T,
Q_total=1.0E0,
Cathode=T,

Ref_zpos=0.0E0,
Ref_Ekin=7.5E-1, sig_Ekin=1.5,
Dist_z='gauss' , Dist_pz='g',


Dist_x='g', Dist_px='g',
Dist_y='g', Dist_py='g',
sig_x=1.0E0, Nemit_x=1.5E0,
sig_y=1.0E0, Nemit_y=1.5E0,
/
```

| **Parameter** | **Specification** |
|---|---|
| Ipart | Number of particles used to run the MC simulation. |
| Q_total | Total charge of the bunch in $nC$ |
| RefEkin, sig_Ekin | Initial energy of particles in $MeV$ and rms spread in $keV$ |
| sig_x, sig_y | RMS bunch size in x and y axis in $mm$ |
| Nemit_x, Nemit_y | Normalized emittance in x and y direction in $\pi * mrad * mm$ |
| Dist_ (x,y) | Spatial distribution. 'g' means Gaussian |
| Dist_ (px,py) | Momentum distribution. 'g' means Gaussian |

Table 5.1.1: Important parameters of the program generator

Explanation of the most important lines above in Table 5.1.1.

The lines above can be written in a text editor and saved with a .in extension (generator.in in this example). Using ubuntu, the program runs with the command:

```
./generator generator.in
```

The output of this program, is a file containing the position and momentum of *Ipart* particles that are defined by the user.

| | 1 | 2 | 3 | 4 | 5 | 6 | 7 | 8 | 9 | 10 |
|---|---|---|---|---|---|---|---|---|---|---|
| Parameter | x | y | z | px | py | pz | clock | macro charge | particle index | status flag |
| Unit | m | m | m | eV/c | eV/c | eV/c | ns | nC | | |

Table 5.1.2: output file of the program generator

The parameters of interest can be visualized by plotting the data. The program *postpro* generates such plots, as shown in Figures 5.1.1 and 5.1.2. To ensure high-quality visualizations, I have set $Ipart = 1.0E5$. The resulting distributions align with the predictions made in the input file. Although *postpro* supports various types of distributions, including plateau, this analysis will focus solely on the Gaussian distribution.

The particle phase-space coordinates of the initial distribution are needed in order to run the ASTRA algorithm in the next step.

### 5.1.2 ASTRA

The program ASTRA tracks particles through user-defined external fields, considering the space charge field of the particle cloud. The tracking utilizes a non-adaptive, 4th-order Runge-Kutta integration method. The input file consists of *namelists* and an example is written below:

```
&NEWRUN
Head=' example run'
RUN=1,
Distribution = 'rfgun.ini',
Xoff=0.0, Yoff=0.0,
TRACK_ALL=T,
```

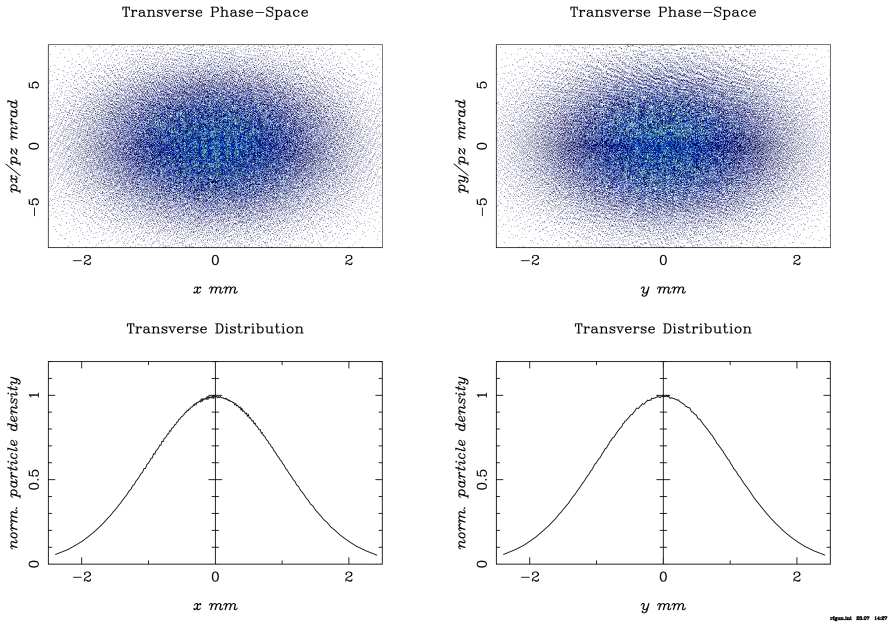


Figure 5.1.1: Transverse phase-space and distribution

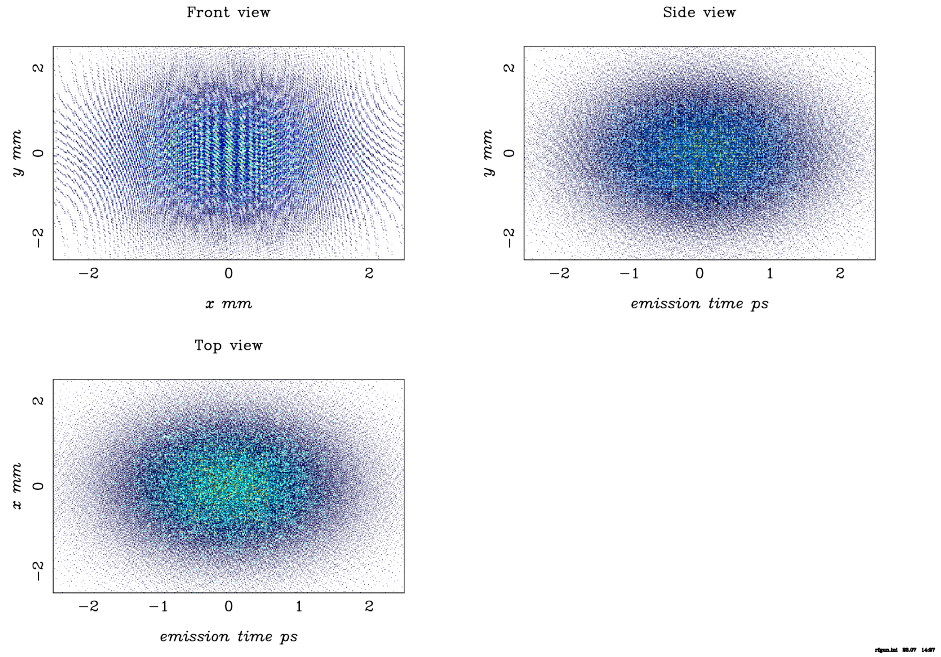


Figure 5.1.2: Front view and x,y as a function of the emission time

```
Auto_phase=T
H_max=0.001,
/
```

```
&OUTPUT
ZSTART=0.0,
ZSTOP=1.5,
Zemit=500,
Zphase=2,
RefS=T
EmitS=T,
/

&CHARGE
LSPCH=T,
LSPCH3D=T,
Nrad=10, Cell_var=2.0, Nlong_in=10
min_grid=0.0
Max_Scale=0.05
/
&CAVITY
LEField=T,
File_Efield(1)='rfField.dat', C_pos(1)=0.0,
C_noscale(1)=F
Nue(1)=2.856,
MaxE(1)=30.0,
Phi(1)=0.0,
/

&SOLENOID
LBField=T,
File_Bfield(1)='Solenoid.dat',
S_pos(1)=0.0,
MaxB(1)=0.35, S_smooth(1)=10
/

&QUADRUPOLE
Lquad=T,
!Q_grad(1)=20,
Q_K(1)=-0,
Q_length(1)=0.1,
Q_bore(1)=0.035
Q_pos(1)=0.5,
Q_zrot(1)=0.0
/
```

The namelist 'NEWRUN' contains instructions for the tracking of particles. The namelist 'OUTPUT' specifies the output parameters that will be presented.

| Parameter | Specification |
|---|---|
| Distribution | name of the initial particle distribution from Generator |
| Xoff, Yoff | Horizontal/Vertical offset of the distribution |
| H_max | maximum time step for the Runge-Kutta integration in $ns$ |
| | |

Table 5.1.3: Namelist 'Newrun'

| Parameter | Specification |
|---|---|
| ZSTART | minimal z postion for the generation of output in $m$ |
| ZSTOP | tracking will stop when the bunch center passes ZSTOP |
| Zemit | intervals between zstart and zstop |
| Zphase | Zemit = n·Zphase |

Table 5.1.4: Namelist 'Output'

The namelist 'CHARGE' includes parameters when taking space charge effects into consideration.

| Parameter | Specification |
|---|---|
| LSPCH | If TRUE, space charge effects will be taken into account |
| Nrad | number of grid cells in radial direction up to the bunch radius |
| Cell_var | variation of the cell height in radial direction<br>The innermost cell is cell_var times higher than the outermost cell. |
| Nlong_in | maximum number of grid cells in longitudinal direction within the bunch length |
| min_grid | minimum grid length during emission |

Table 5.1.5: Namelist 'Charge'

The namelist CAVITY contains information about the RF field in the structure.

| Parameter | Specification |
|---|---|
| LEField | if false, all cavity fields are turned off. |
| File_Efield( ) | file that contains information about the rf fields |
| C_pos( ) | position of the field |
| C_noscale( ) | if flase, the field will be scaled to MaxE |
| Nue( ) | frequency of rf field in $GHz$ |
| MaxE( ) | Max value of E field in $MV/m$ |
| Phi( ) | phase of RF field in $rad$ |

Table 5.1.6: Namelist 'Cavity'

The namelist SOLENOID includes fields generated from solenoids.

The namelist QUADRUPOLE includes fields generated from quadrupole magnets.

Table 5.1.9 presents the radar frequency bands as defined by the IEEE standard. [15]

| Parameter | Specification |
|---|---|
| LBField | if false, all solenoids fields are turned off. |
| File_Bfield( ) | file that contains information about the solenoid fields |
| S_pos | position of the solenoid |
| MaxB( ) | Max value of solenoid magnetic field in $T$ |

Table 5.1.7: Namelist 'Solenoid'

| Parameter | Specification |
|---|---|
| Lquad | if false, all quadrupoles are turned off. |
| Q_grad( ) | quadrupole gradient $T/m$ |
| Q_K( ) | focusing strength of the quadrupole $m^{-2}$ |
| Q_length | length of quadrupole |
| Q_bore | taper parameter for the quadrupole field edge |
| Q_pos | position of quadrupole |
| Q_zrot | rotation of quadrupole |

Table 5.1.8: Namelist 'quadrupole'

| Band designation | Frequency range | Explanation of meaning of letters |
|---|---|---|
| HF | 0.003 to 0.03 GHz | High frequency |
| VHF | 0.03 to 0.3 GHz | Very high frequency |
| UHF | 0.3 to 1 GHz | Ultra-high frequency |
| L | 1 to 2 GHz | Long wave |
| S | 2 to 4 GHz | Short wave |
| C | 4 to 8 GHz | Compromise between S and X |
| X | 8 to 12 GHz | Used in World War II for fire control |
| Ku | 12 to 18 GHz | Kurz-under |
| K | 18 to 27 GHz | German: Kurz (short) |
| Ka | 27 to 40 GHz | Kurz-above |
| V | 40 to 75 GHz | |
| W | 75 to 110 GHz | W follows V in the alphabet |
| mm or G | 110 to 300 GHz | Millimeter |

Table 5.1.9: Frequency bands according to IEEE [15]

## 5.2 Simulation without Space Charge

In this part, I'll examine the behavior of electron beams in a linear accelerator, neglecting space charge effects. This approach aims to enhance familiarity with the simulation and understand the various effects of parameter changes without causing beam instability, which will be addressed in the next subsection.

### 5.2.1 L-Band Simulation Results

For the first run, a bunch will be accelerated by using the rf field already provided by the developers, which essentially is a 3-Cell in L band (approx 1.3GHz). Solenoid fields and quadrupoles are switched off. The electric field is shown in figure 5.2.1

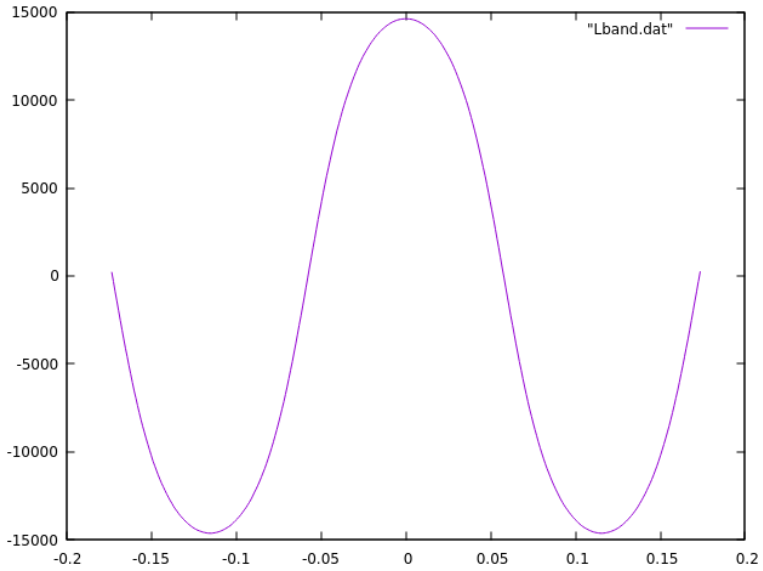


Figure 5.2.1: Cavity field, it was shifted by 20cm to the right because the original file was as shown. The vertical axis is arbitrary, since it is limited by maxE in the simulation code

As seen in the emittance graph, fluctuations occur after the electric field starts to act. However, the emittance remains relatively constant overall, as predicted by the Liouville theorem. The transverse size of the beam decreases, and although the beam is initially collimated, it spreads out after entering the field. As the beam gains momentum in the z-direction, the divergence decreases. The rate of change of momentum with respect to distance, dp/dz, is also observed. The particle energy increases inside the waveguide, and the output energy has a low spread of 0.5%.

In all of the following simulations, the beam will be stable and the normalized emittance will remain relatively constant in the accelerating structure. From $\epsilon_n = \beta\gamma\sigma_x\sigma_{x'}$, we can see that as the speed increases, for a constant emittance the product $\sigma_x\sigma_{x'}$ will decrease. The divergence seems to stabilize and the size decreases. Also, for higher momenta, the beam will not deflect as much as in lower speeds.

| Input | Qb (nC) | $\sigma_x, \sigma_y (mm)$ | $K_{in} \pm \Delta K (keV)$ | cells | maxE(MV/m) | L(m) |
|---|---|---|---|---|---|---|
| Vaule | 1 | 1 , 1 | $50 \pm 1$ | 3 | 35 | 0.5 |

| Output | $E \pm \Delta E (MeV)$ | $\sigma_x, \sigma_y (mm)$ | $\epsilon_x, \epsilon_y$ $(\pi mradmm)$ | $\sigma_z (mm)$ | $\epsilon_z$ $(\pi mradkeV)$ |
|---|---|---|---|---|---|
| Vaule | $5.84 \pm 0.03$ | 0.53 , 0.53 | 1.79 , 1.83 | 0.45 | 0.55 |

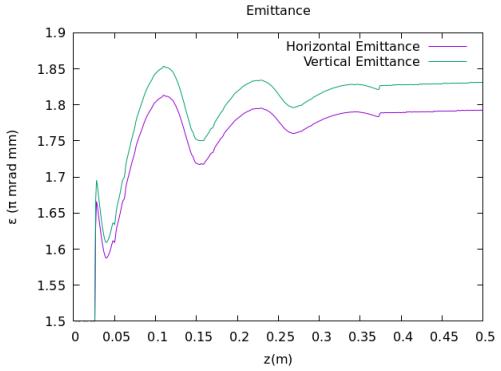


(a) Emittance

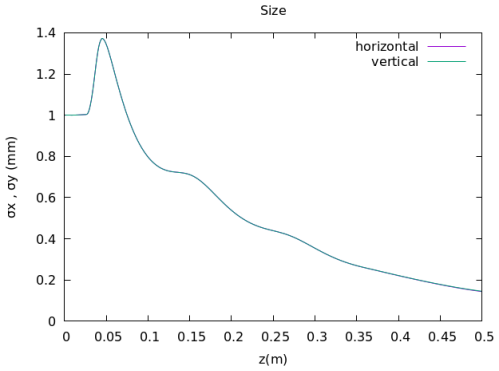


(b) Size

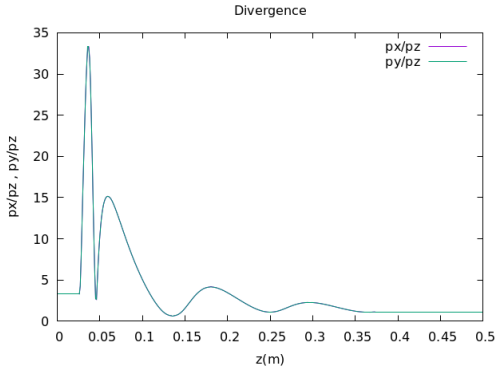


(c) Divergence

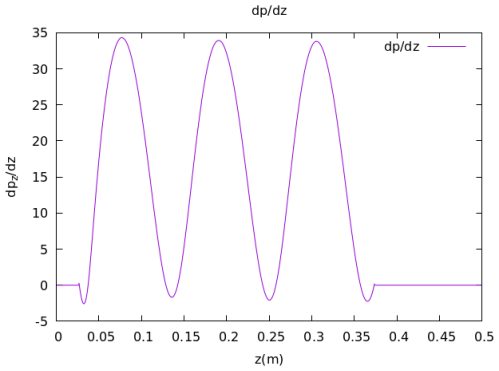


(d) dp/dz

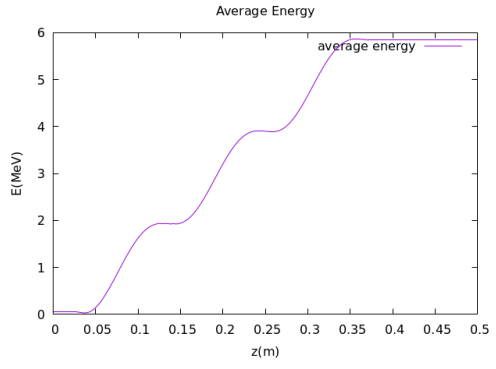


(e) Average Energy

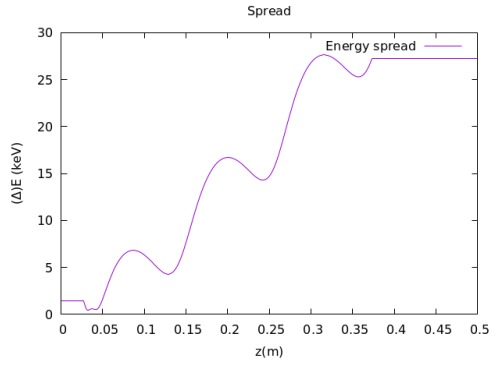


(f) Spread

Figure 5.2.2: Table of plots

### 5.2.2 S-Band Simulation Results

In this section, the frequency within the waveguide is set to the S-Band at $f = 2.856GHz$, as this is the standard operating frequency for most S-Band linear accelerators. The subsequent simulations will examine the impact of varying the number of cavities and the maximum energy of the RF field on the beam. Additionally, the resulting changes in other related graphs will be analyzed.

I conducted two simulation runs: the first (Figure 5.2.4) with the same number of cells as the L-band run (Figure 5.2.2) to observe the differences, and the second (Figure 5.2.5) with a higher charge, greater amplitude of the RF field, and more cells to achieve higher energies. Consequently, the structure length in the second run is larger.

The results show that the final energy in the first run is lower than in the L-band, and the acceleration occurs over a shorter distance. This is due to the higher frequency of the S-band, which results in a smaller wavelength or cell size.

In both runs, the emittance exhibits an upward trend, which is undesirable as a constant emittance is preferred. The beam size decreases in the first few centimeters in both runs; however, in the second run, the beam size increases significantly afterwards, which is also unfavorable.

The bigger charge seems to not have an effect on anything, and that is because the space charge forces were not taken into consideration. The effect of higher charge values will be very noticable in the following simulations.

It is clear that higher energies can be achieved by increasing the cell number or the amplitude of the electric field. Using the least square method in the following simulations, the final energy can be expressed as a function of the product of the number of cells and the rf amplitude through the equation $E = a + b(no.cells)(maxE)$ where $a = -3.5 \pm 1.9MeV$ and $b = (2.61 \pm 0.04)10^{-2}$ for an S-band linac. See figure 5.2.3

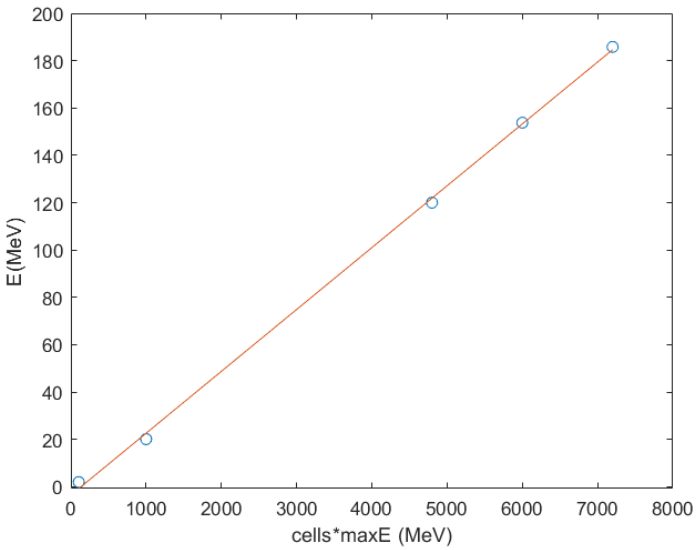


Figure 5.2.3: Final energy as a function of the product of number of cells and maxE.

| Input | Qb (nC) | $\sigma_x, \sigma_y (mm)$ | $K_{in} \pm \Delta K (keV)$ | cells | maxE(MV/m) | L(m) |
|---|---|---|---|---|---|---|
| Vaule | 1 | 1 , 1 | $50 \pm 1$ | 3 | 35 | 0.5 |

| Output | $E \pm \Delta E (MeV)$ | $\sigma_x, \sigma_y (mm)$ | $\epsilon_x, \epsilon_y$ $(\pi mradmm)$ | $\sigma_z (mm)$ | $\epsilon_z$ $(\pi mradkeV)$ |
|---|---|---|---|---|---|
| Vaule | $2.03 \pm 0.03$ | 0.19 , 0.20 | 1.69 , 1.72 | 0.48 | 0.53 |

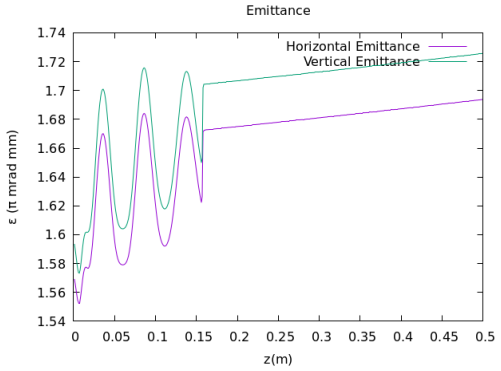


(a) Emittance

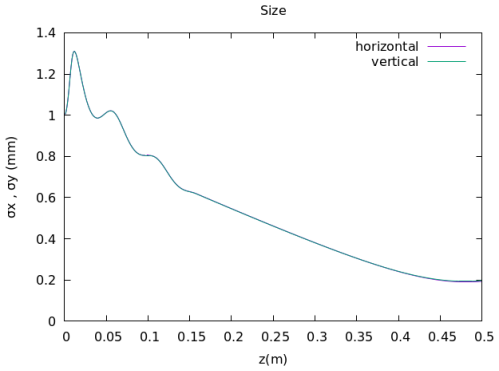


(b) Size

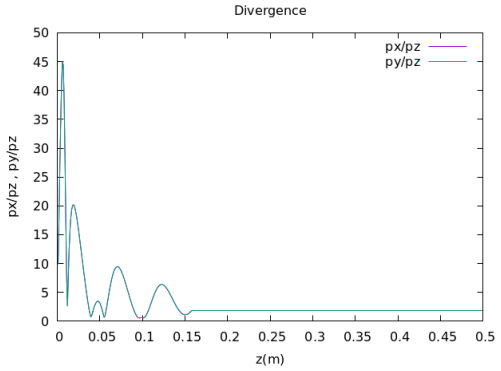


(c) Divergence

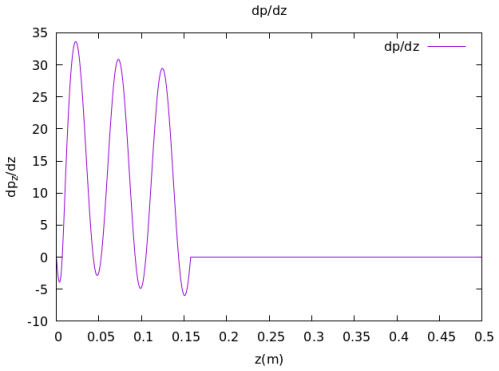


(d) dp/dz

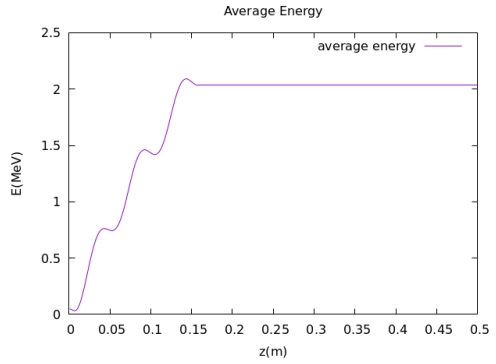


(e) Average Energy

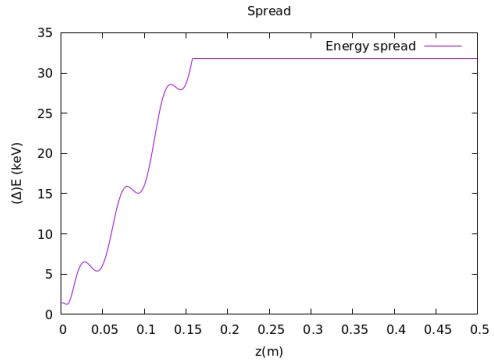


(f) Spread

Figure 5.2.4: Table of plots: S-Band

| Input | Qb (nC) | $\sigma_x, \sigma_y (mm)$ | $K_{in} \pm \Delta K (keV)$ | cells | maxE(MV/m) | L(m) |
|---|---|---|---|---|---|---|
| Vaule | 100 | 1 , 1 | $50 \pm 1$ | 20 | 50 | 1.5 |

| Output | $E \pm \Delta E (MeV)$ | $\sigma_x, \sigma_y (mm)$ | $\epsilon_x, \epsilon_y$ $(\pi mradmm)$ | $\sigma_z (mm)$ | $\epsilon_z$ $(\pi mradkeV)$ |
|---|---|---|---|---|---|
| Vaule | $20.1 \pm 0.3$ | 1.1 , 1.1 | 1.96 , 2.00 | 0.30 | 1.19 |

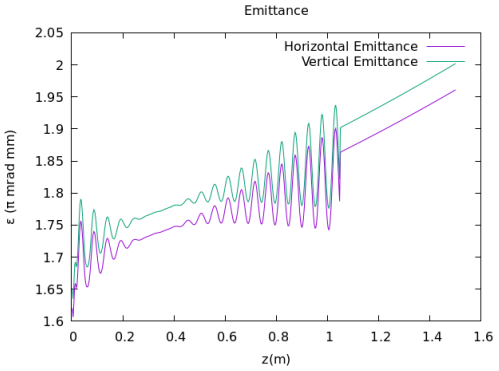


(a) Emittance

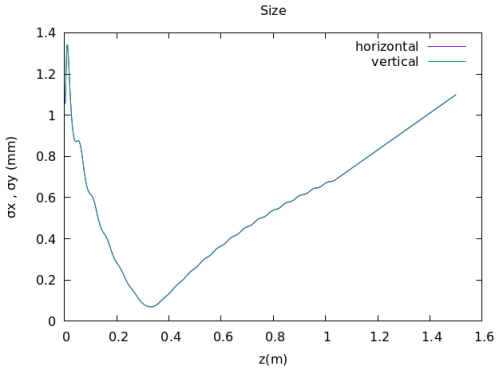


(b) Size

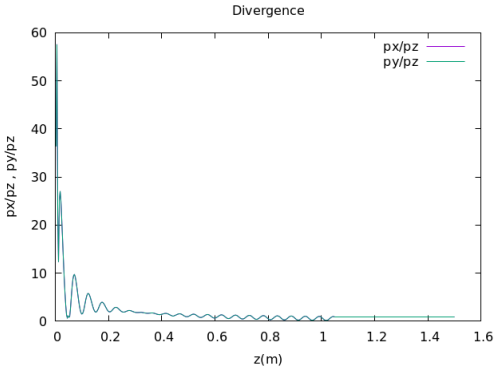


(c) Divergence

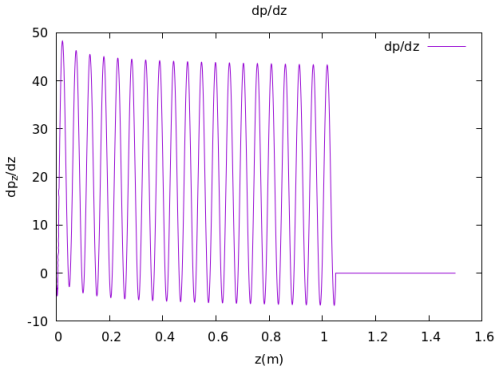


(d) dp/dz

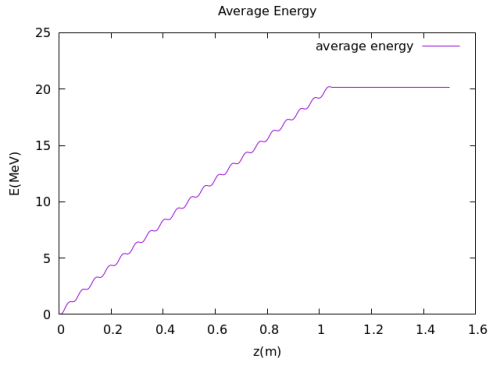


(e) Average Energy

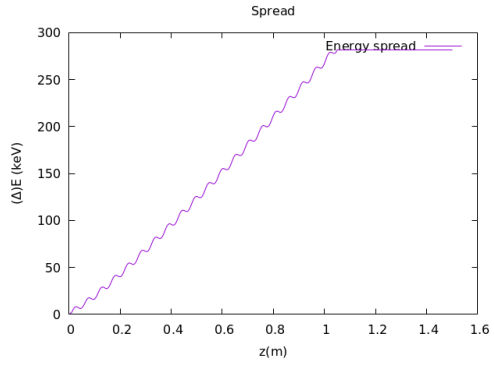


(f) Spread

Figure 5.2.5: Table of plots: S-Band

### 5.2.3 The effect of Solenoids - 140MeV Beam

In this run I attempted to increase the number of cells and the maximum amplitude of the RF signal, in order to reach an output beam energy of ~140MeV. It was necessary to increase the length of the structure. There were huge fluctuations of the beam emittance and the size of the beam would increase by a lot, which is an unwanted behaviour.

In order to resolve this issue, solenoids were added as shown in figure 5.2.6 with a maximum field value of $B_{max} = 0.35T$. The field is parallel to the direction of the beam, so that only particles that diverge from the path are affected. Those particles will gain angular momentum while inside the fields and lose it after exiting, resulting a net angular momentum of zero.

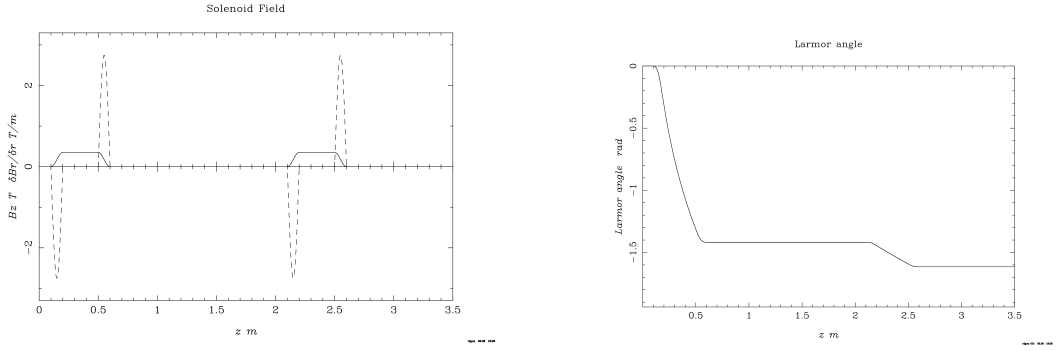


(a) Solenoid fields (MaxB=0.35T)

(b) Larmor angle

Figure 5.2.6: Solenoid Fields and Larmor angle

Charged particles under the influence of magnetic fields undergo Larmor precession. The larmor angle $\theta_L = \omega_L t$, where $\omega_L = \frac{eB}{m_e}$, is indicative of the time spent inside the magnetic field. In the scenario described, although the magnetic field strength is the same in both solenoids, the speed of the particle bunch is lower in the first solenoid than in the second. As a result, the particles spend more time in the magnetic field in the first solenoid, leading to a greater 'Larmor angle'. During that time, the particles perform a helical motion.

Solenoids are particularly effective at lower particle velocities, as illustrated in the Larmor graph 5.2.6b. At these lower speeds, solenoids help to significantly reduce emittance fluctuations, thereby stabilizing the beam size. Their symmetric focusing ability allows them to influence in both x and y transverse directions equally, making them highly effective for controlling the beam size throughout the linac. This symmetry ensures consistent focusing, which is crucial for maintaining beam quality and minimizing size variations as the beam progresses through the accelerator.

| Input | Qb (nC) | $\sigma_x, \sigma_y (mm)$ | $K_{in} \pm \Delta K (keV)$ | cells | maxE(MV/m) | L(m) |
|---|---|---|---|---|---|---|
| Vaule | 100 | 1 , 1 | $50 \pm 1$ | 60 | 100 | 3.5 |

| Output | $E \pm \Delta E (MeV)$ | $\sigma_x, \sigma_y (mm)$ | $\epsilon_x, \epsilon_y$ $(\pi mradmm)$ | $\sigma_z (mm)$ | $\epsilon_z$ $(\pi mradkeV)$ |
|---|---|---|---|---|---|
| Vaule | $140.4 \pm 0.8$ | 0.42 , 0.42 | 2.06 , 2.04 | 0.19 | 2.44 |

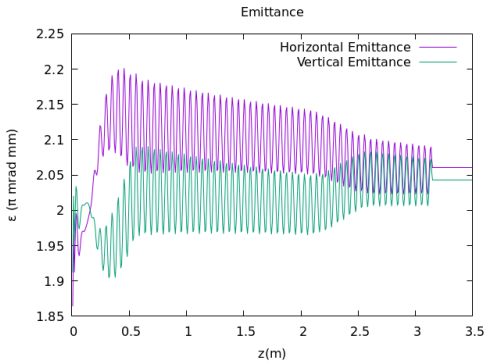


(a) Emittance

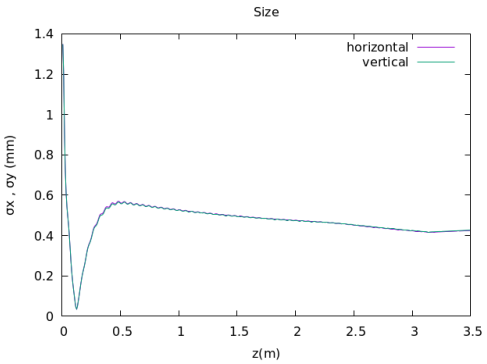


(b) Size

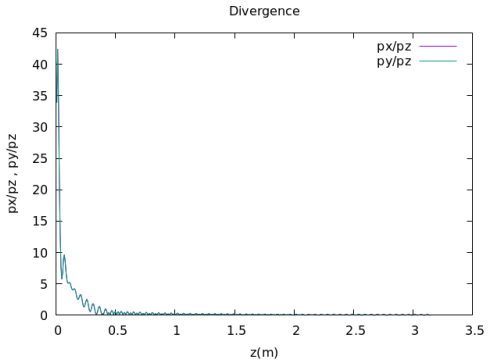


(c) Divergence

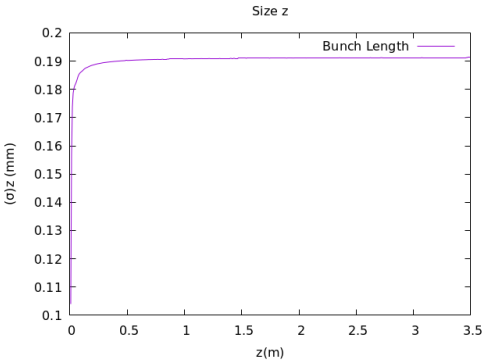


(d) Bunch Length

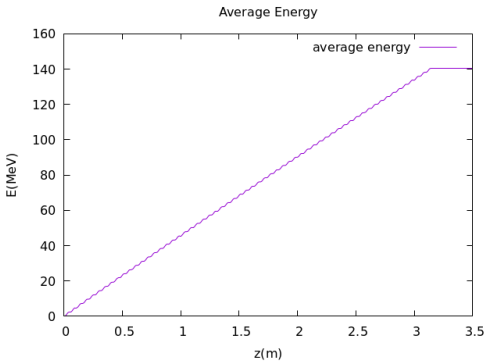


(e) Average Energy

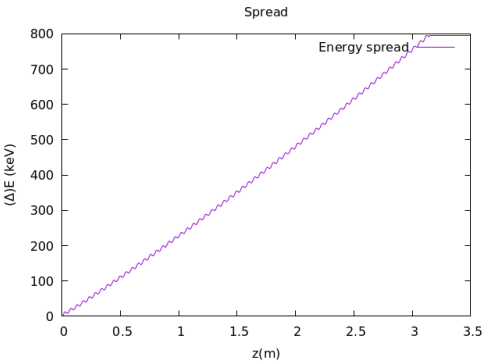


(f) Spread

Figure 5.2.7: Table of plots: Solenoid

## 5.3 Simulation with Space Charge

The previous simulations provided a reasonable approximation for small bunch charges (less than 1 nC). However, for larger bunch charges, the forces become significant enough to cause beam expansion, larger diversion angles or even instability. In the case of FLASH, very high bunch charges are needed (500nC) in order to deliver an ultra high dose in a very small amount of time. Also in the case of X-ray FLASH, where the electrons have to hit a target to release electromagnetic radiation, the conversion efficiency is very small, so it is very important to study such extreme cases.

### 5.3.1 50nC Beam Simulation

For the next simulations, I've increased the beam size to $\sigma_x = \sigma_y = 3mm$, which would increase the emittance to about $\epsilon = 160\pi mradmm$. The average energy and energy spread are not influenced by the forces. Indeed, for higher energies, the beam is more stable. Solenoids were used again in order to smooth out the beam at 0.8, 1.8 and 2.8m and the amplitude of the rf field was set to $80MV/m$.

In the first simulation (Figure 5.3.2), the emittance exhibits significant fluctuations initially, which stabilize after 2 meters in the waveguide. The beam size initially increases to about twice its original size but then shrinks transversely as the energy increases. On the other hand, the bunch length grows to a stable value, and the energy spread is considerably large (5x that observed in Figure 5.2.7) indicating substantial longitudinal expansion of the beam due to space charge forces. The energy spread (4%) is very high, so this configuration is not suitable for medical applications.

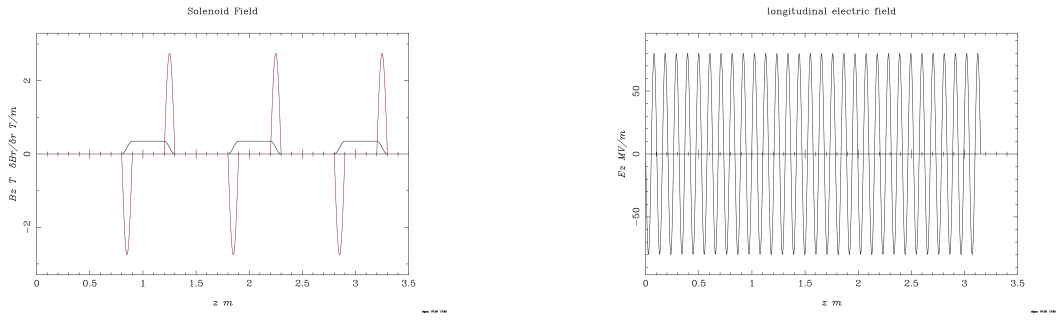


(a) Solenoid fields (MaxB=0.35T)

(b) Cavity fields (MaxE=80MV/m)

Figure 5.3.1: Solenoid and Cavity Fields

| Input | Qb (nC) | $\sigma_x, \sigma_y (mm)$ | $K_{in} \pm \Delta K (keV)$ | cells | maxE(MV/m) | L(m) |
|---|---|---|---|---|---|---|
| Vaule | 50 | 3 , 3 | $50 \pm 1$ | 60 | 80 | 3.5 |

| Output | $E \pm \Delta E (MeV)$ | $\sigma_x, \sigma_y (mm)$ | $\epsilon_x, \epsilon_y$ $(\pi mradmm)$ | $\sigma_z (mm)$ | $\epsilon_z$ $(\pi mradkeV)$ |
|---|---|---|---|---|---|
| Vaule | $120 \pm 5$ | 1.12 , 1.09 | 157 , 160 | 2.63 | 4315 |

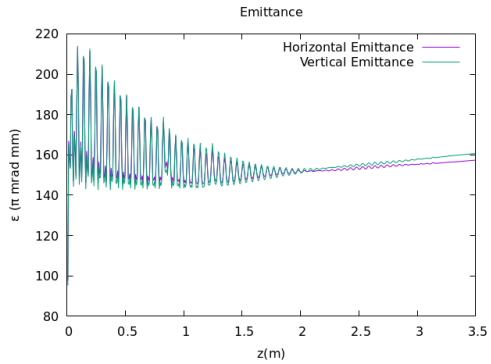


(a) Emittance

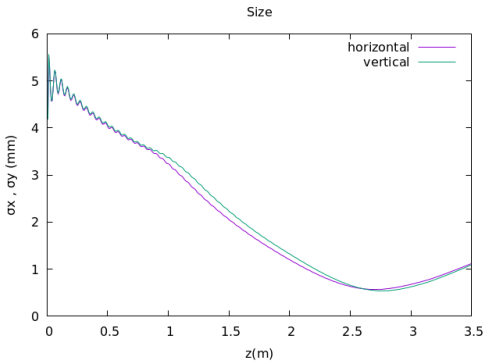


(b) Size

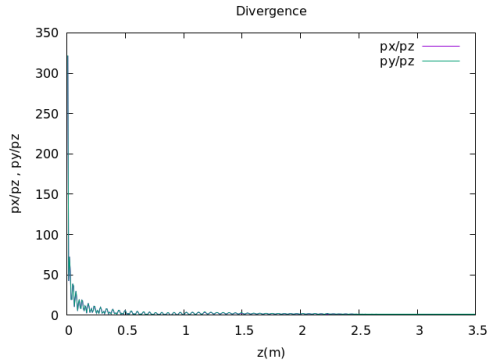


(c) Divergence

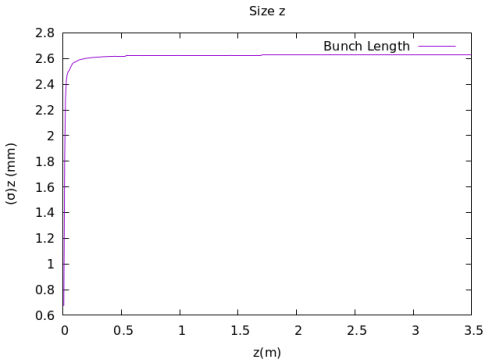


(d) Bunch Length

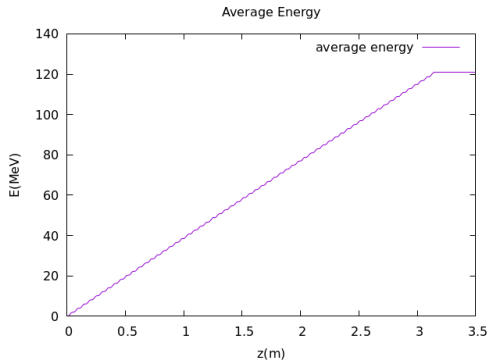


(e) Average Energy

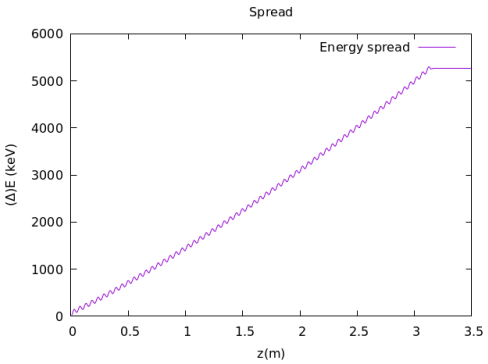


(f) Spread

Figure 5.3.2: Table of plots: Space Charge

### 5.3.2 Scaling up to 500nC beam

The previous run (Figure 5.3.2) was performed with a bunch charge of 50nC. By increasing the charge to 500nC, the beam would become unstable since a large percentage of the particles (about 28%) would get lost and about 1% would travel backwards. In order to resolve this issue, I will try to vary the input kinetic energy before entering the accelerating structure, the initial size, the amplitude or even the shape of the electric field.

For the first run (Figure 5.3.3), I have increased the beam size to $\sigma_x = \sigma_y = 6.0mm$, the initial kinetic energy to $K_{in} = 200keV$ and the amplitude of the electric field to be $E_{zmax} = 100MV/m$. Now the beam is stable and reaches a maximum energy of $E = 154MeV$. For reference, in a second run (Figure 5.3.4) I increased the electric field amplitude to $E'_{zmax} = 120MV/m$ with a maximum electron energy of $E' = 186MeV$. The beam dimensions were selected to reduce space charge forces. By increasing the standard deviation of the beam, the space charge forces, which are particularly significant at low velocities, are now mitigated.

For larger electric fields, the emittance exhibits fewer fluctuations, resulting in a more stable and consistently lower value. In order to reduce emittance, the size should be reduced while the divergence is small. A way to reduce the beam size without causing beam instability is by increasing the initial kinetic energy of the electrons as they enter the accelerating structure from the thermionic cathode and bunching system. However, these systems typically deliver beams with energies ranging from 50 to 80 keV, making it challenging to achieve practical energies above 200 keV. Solenoids were used again at positions 0.6m, 1.6m, 2.6m to smooth out the beam and no quadrupoles.

The final result seems to be quite stable since the beam emittance remains constant with very few fluctuations in the accelerating structure. In both cases the beam size seems to shrink and remain fairly constant at the end. Since the space charge forces are reduced for higher energies, the beam can be stable at smaller sizes. The beam divergence is very small at the output and the final energy spread is 2% in the first case, which is generally considered as very wide. In the second case the spread is about 1.5% which is a lot better, considering the very high bunch charge, but for reference, medical linacs have a tighter energy spread of less than 1%.

| Input | Qb (nC) | $\sigma_x, \sigma_y (mm)$ | $K_{in} \pm \Delta K (keV)$ | cells | maxE(MV/m) | L(m) |
|---|---|---|---|---|---|---|
| Vaule | 500 | 6.0 , 6.0 | $200 \pm 5$ | 60 | 100 | 3.5 |

| Output | $E \pm \Delta E (MeV)$ | $\sigma_x, \sigma_y (mm)$ | $\epsilon_x, \epsilon_y$ $(\pi mradmm)$ | $\sigma_z (mm)$ | $\epsilon_z$ $(\pi mradkeV)$ |
|---|---|---|---|---|---|
| Vaule | $154 \pm 3$ | 1.56 , 1.44 | 570 , 583 | 2.71 | 6187 |

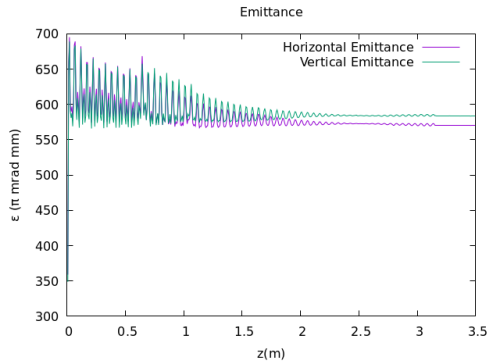


(a) Emittance

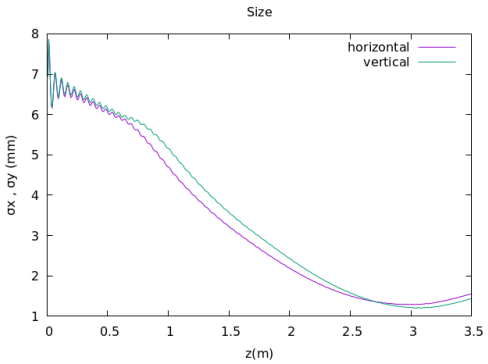


(b) Size

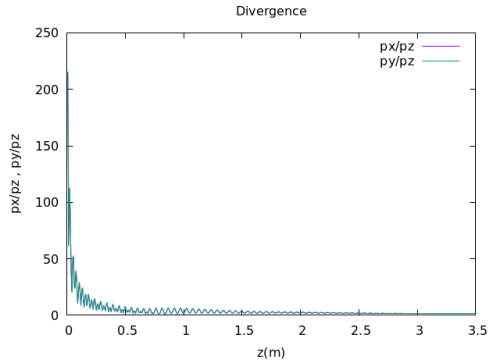


(c) Divergence

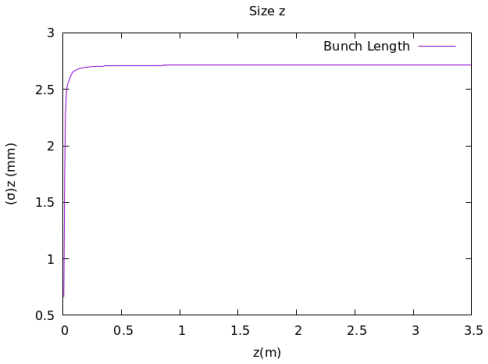


(d) Bunch Length

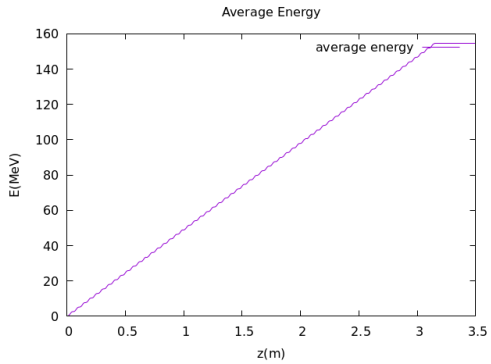


(e) Average Energy

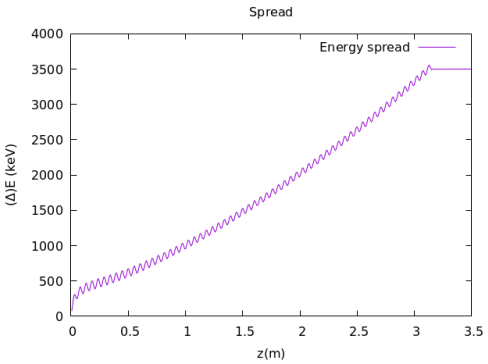


(f) Spread

Figure 5.3.3: Table of plots: 500nC 1st run

| Input | Qb (nC) | $\sigma_x, \sigma_y (mm)$ | $K_{in} \pm \Delta K (keV)$ | cells | maxE(MV/m) | L(m) |
|---|---|---|---|---|---|---|
| Vaule | 500 | 6.0 , 6.0 | $200 \pm 5$ | 60 | 120 | 3.5 |

| Output | $E \pm \Delta E (MeV)$ | $\sigma_x, \sigma_y (mm)$ | $\epsilon_x, \epsilon_y$ $(\pi mradmm)$ | $\sigma_z (mm)$ | $\epsilon_z$ $(\pi mradkeV)$ |
|---|---|---|---|---|---|
| Vaule | $186 \pm 3$ | 1.96 , 1.76 | 533 , 542 | 2.36 | 4709 |

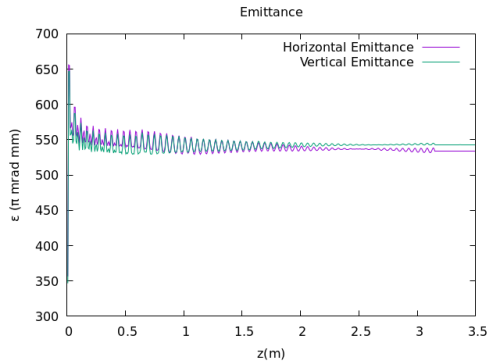


(a) Emittance

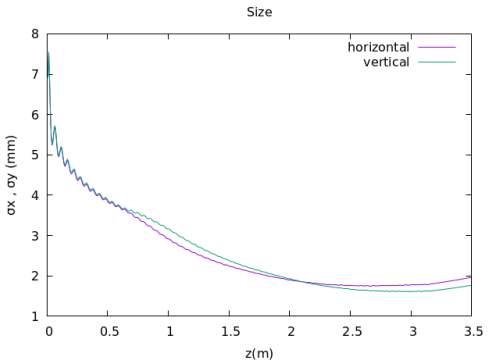


(b) Size

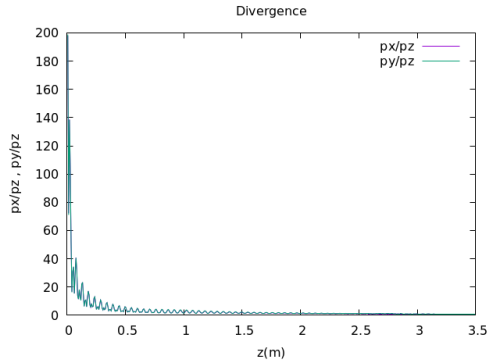


(c) Divergence

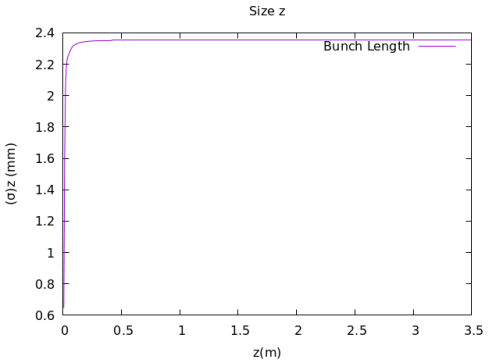


(d) Bunch Length

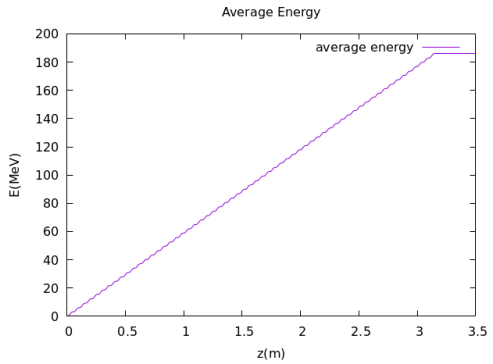


(e) Average Energy

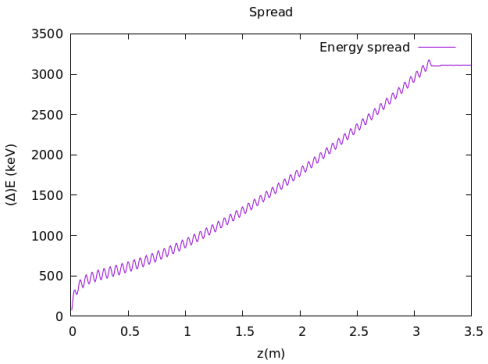


(f) Spread

Figure 5.3.4: Table of plots: 500nC 2nd run

## 5.4 Beam Dynamics and Space Charge Fields

The ASTRA software using the tool *Fieldplot*, allows for the plotting of electric and magnetic fields within the electron bunch, based on properties such as energy, size, charge, and charge distribution. To achieve this, I create a file similar to generator.in, set the cathode parameter to False, and input the beam properties derived from previous ASTRA simulations. By using the *postpro* tool, I can visualize the characteristics of the output beam.

### 5.4.1 Beam Distribution Plots: X-Y, Y-Z, and X-Z Projections

In the input file for *postpro*, I've set the parameters as described above and the data as seen on the simulation of Figure 5.3.4 at $z = 3.5m$. The standard deviation $\sigma$ and the FWHM are connected by the formula $FWHM = 2\sqrt{2\ln 2}\sigma \approx 2.354\sigma$ for a Gaussian distribution.

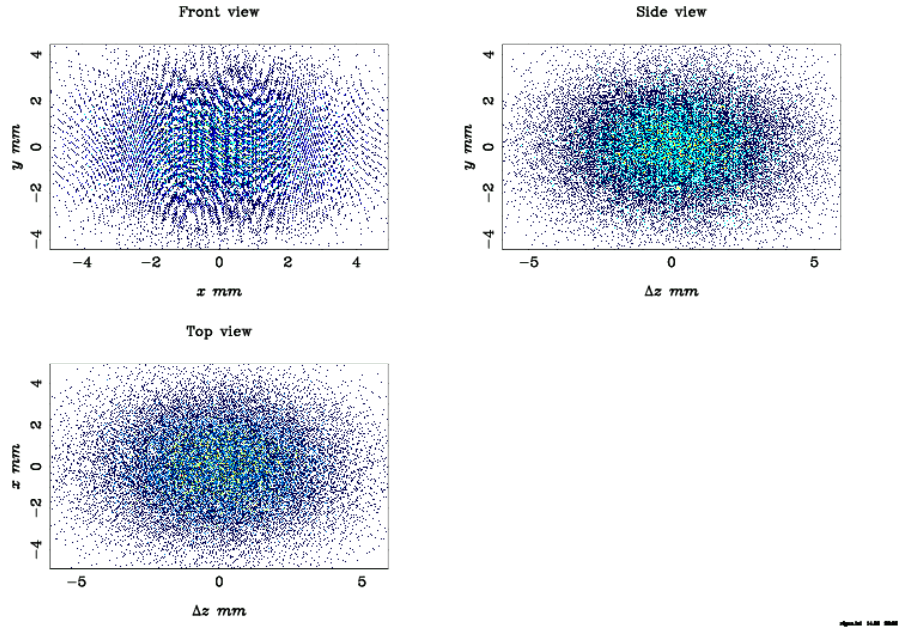


Figure 5.4.1: Projections of output beam

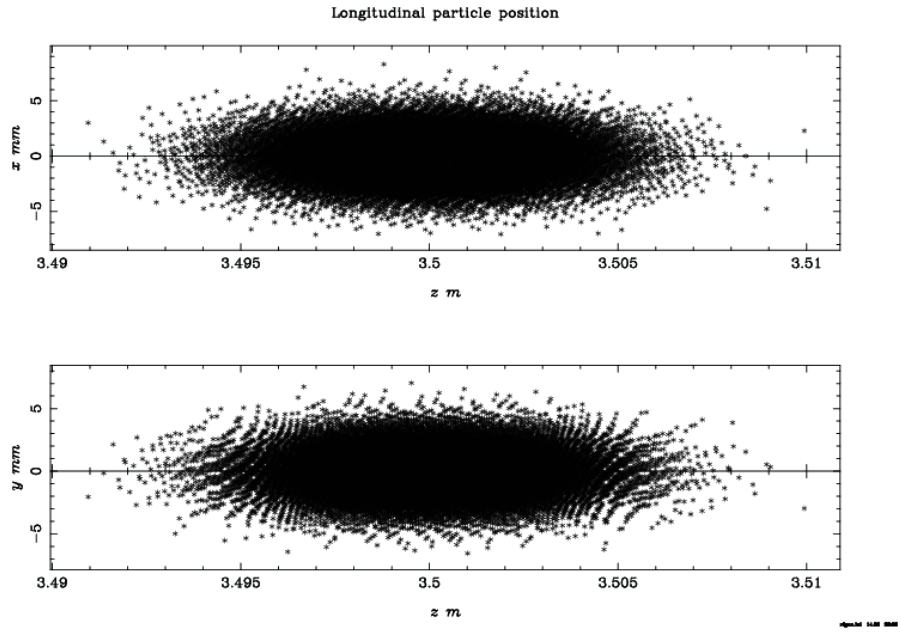


Figure 5.4.2: longitudinal profile of output beam

### 5.4.2 Charge dependance of Fields

As shown in Equations 3.3.9 and 3.3.10, the fields exhibit a linear dependence on the charge of the bunch. This linear relationship is clearly seen in the simulation results presented in Figures 5.4.3 and 5.4.4. In the latter figure, the charge is 100 times greater than in the former, and correspondingly, the fields are scaled by a factor of 100.

For a gaussian distribution of charged particles [41]:

$$n(r) = \frac{1}{(2\pi)^{3/2}\sigma_r^2\sigma_z} e^{-\frac{r^2}{2\sigma_r^2}} e^{-\frac{z^2}{2\sigma_z^2}} \tag{5.4.1}$$

For the electric field, eq.3.3.9 can be written as:

$$E_r = \frac{q}{\epsilon_0 r}\int_r n(r)rdr = \frac{q}{2\pi\epsilon_0}\frac{e^{-\frac{z^2}{2\sigma_z^2}}}{\sqrt{2\pi}\sigma_z}\frac{1-e^{-\frac{r^2}{2\sigma_r^2}}}{r} \tag{5.4.2}$$

and similarly for the magnetic field from eq.3.3.10

$$B_\theta = \frac{qv\mu_0}{r}\int_r n(r)rdr = \frac{q\beta}{2\pi\epsilon_0 c}\frac{e^{-\frac{z^2}{2\sigma_z^2}}}{\sqrt{2\pi}\sigma_z}\frac{1-e^{-\frac{r^2}{2\sigma_r^2}}}{r} \tag{5.4.3}$$

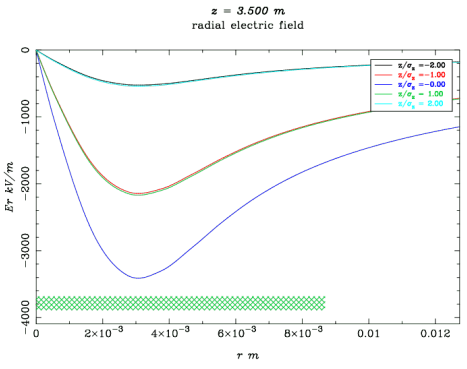


(a) Radial Electric Field - radial

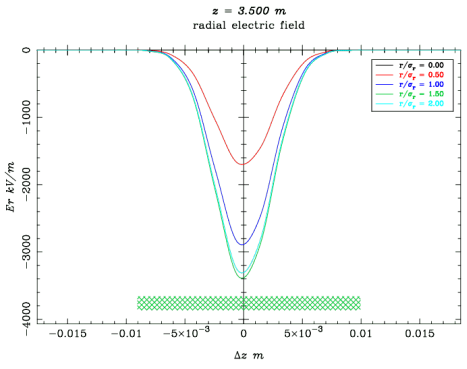


(b) Radial Electric Field - longitudinal

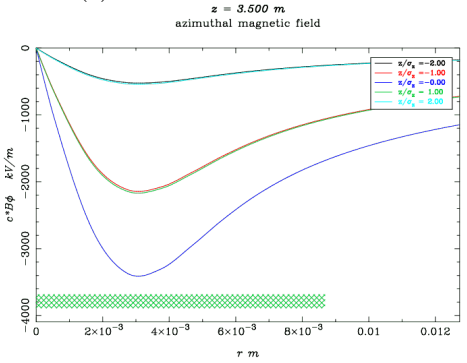


(c) Azimuthial Magnetic Field - radial

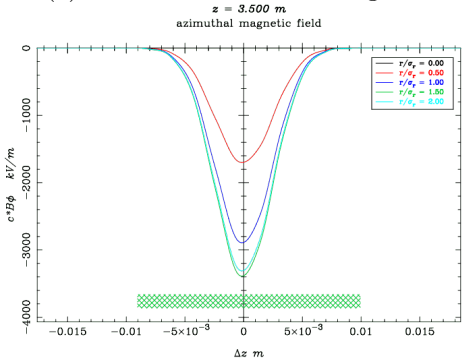


(d) Azimuthial Magnetic Field - long

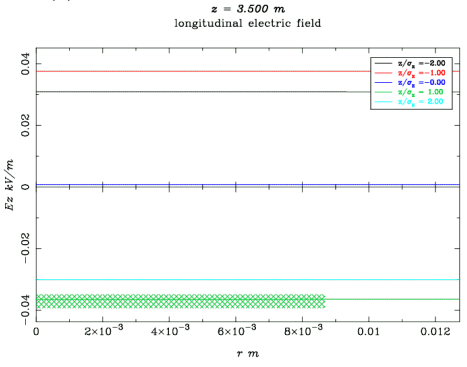


(e) Longitudinal Electric Field - radial

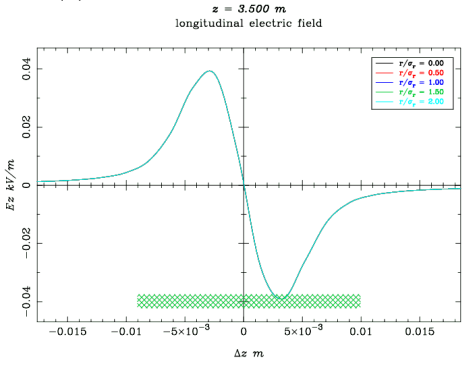


(f) Longitudinal Electric Field - long

Figure 5.4.3: Space Charge fields for a 5nC bunch

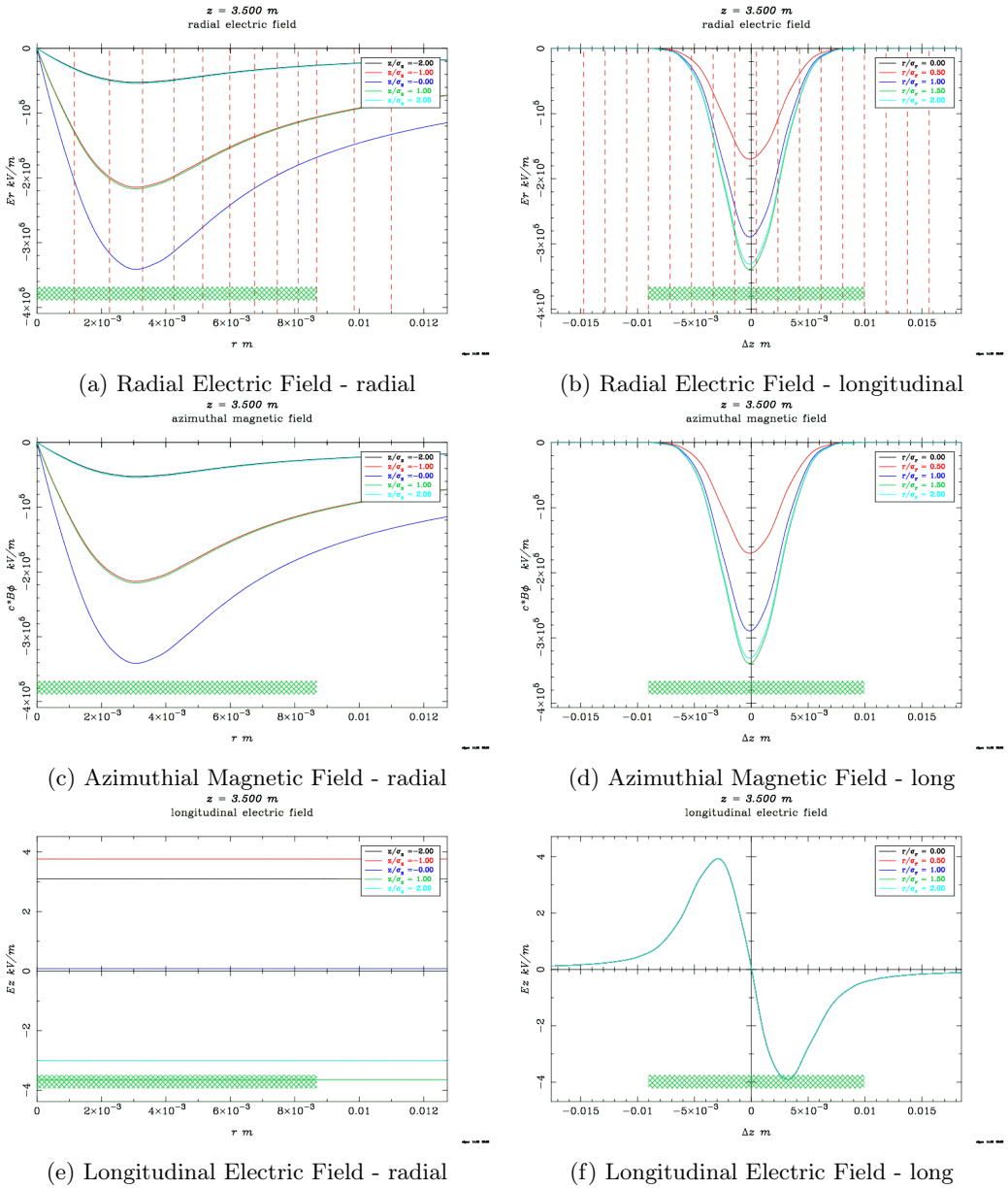


(a) Radial Electric Field - radial

(b) Radial Electric Field - longitudinal

(c) Azimuthial Magnetic Field - radial

(d) Azimuthial Magnetic Field - long

(e) Longitudinal Electric Field - radial

(f) Longitudinal Electric Field - long

Figure 5.4.4: Space Charge fields for a 500nC bunch

### 5.4.3 Beam energy and Space Charge Fields

The Lorentz force is given by eq.3.3.11 and from the $1/\gamma^2$ at the denominator, we see that for lower energy beams such as those at the injector stage before entering the accelerating structure, the force is significantly stronger than that at the output. For a 200keV bunch, $\gamma = 1.3$ and $\beta = 0.69$, whereas for a 180MeV bunch, $\gamma = 365$, which means that for the low energy beam the forces are about $(\gamma_2/\gamma_1)^2 \approx 10^5$ times stronger in the input than at the output.

This is illustrated in Figure 5.4.5. In the simulation, rather than plotting the Lorentz Force directly, the developers plot the 'effective electric field,' which

essentially represents the force per unit charge. Therefore, to achieve the high dose rates required for FLASH radiotherapy, it is important to design more efficient injectors that can pre-accelerate the beam to a high enough energy in a very short period of time.

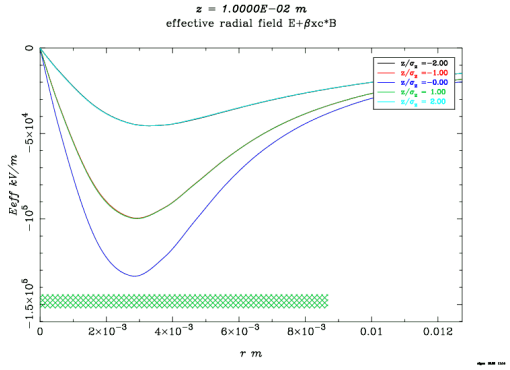


(a) 200keV radial

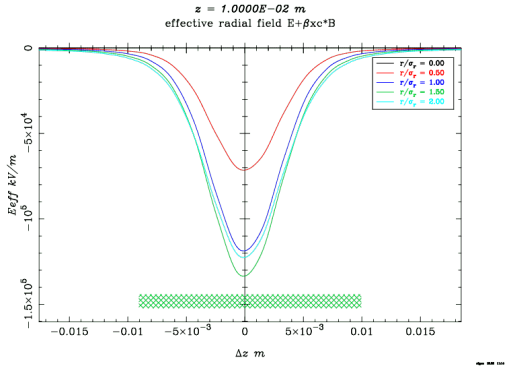


(b) 200keV longitudinal

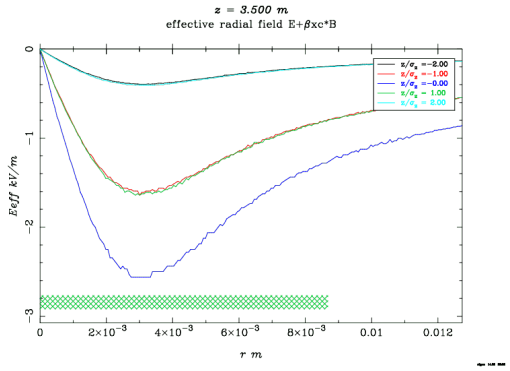


(c) 180MeV radial

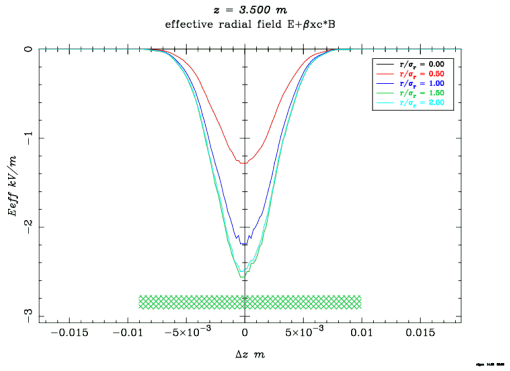


(d) 180MeV longitudinal

Figure 5.4.5: Comparison of the 'effective' electric field for high and low energy beams. $E_{eff} = F_{Lor}/q$

# 6 Dosimetry and DNA damage simulation

Using the output from the linac simulations in the previous section, we can calculate the dose absorbed in a medium, which in our case is water, and then try to run Monte Carlo simulations see DNA damage for different target parameters. The software used will be MCDS and although MCDS cannot directly simulate the effects of FLASH dose rates, we can interact with various parameters within the simulation to approximate the conditions at the irradiation site.

## 6.1 Dose calculation

The dose (in Gy) is calculated by the product of the fluence (particles per unti area) times the stopping power of the medium.

$$D(Gy) = \Phi(\#/m^2) \cdot S(Jm^2/kg) \tag{6.1.1}$$

For the area, I will consider a circular cross section, since in all the simulations above $\sigma_x \approx \sigma_y$ and to convert the standard deviation to FWHM radius, I will multiply by $2\sqrt{2\ln 2}$. Thus, $r^2 = (8\ln 2)\sigma_r$.

The number of particles is easily calculated by dividing the bunch charge to the electron charge $N = q/e$

The mass stopping power as a function of energy can be found using the ESTAR Database. In this case I'll use water as a target. Figure 6.1.1

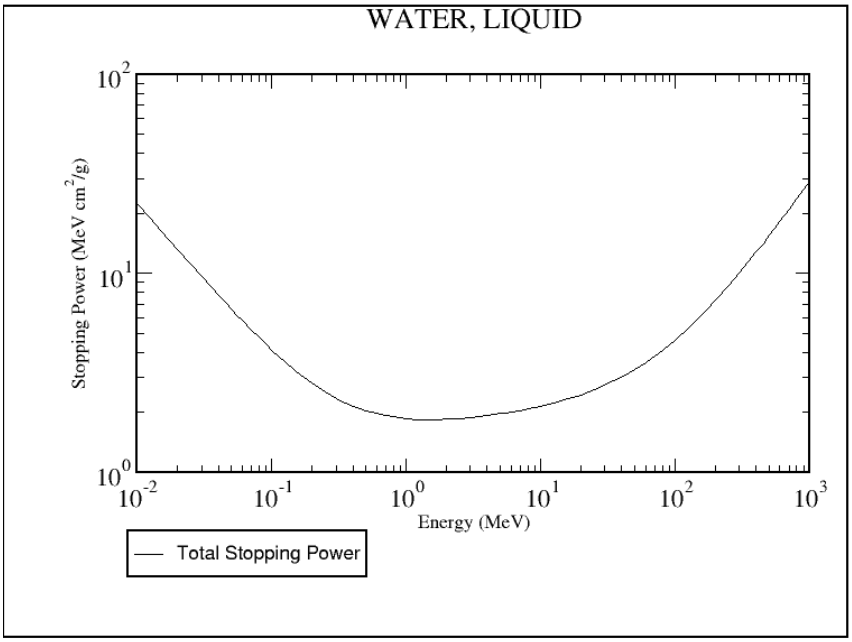


Figure 6.1.1: Mass stopping power of water as a function of energy

By downloading the data from the website, I tried plotting from 2MeV to 250MeV and the function could be approximated to be linear ($R^2 = 0.9996$) see Fig 6.1.2. Using least square regression, the stopping power can be written as

$S = a + bE$, where $a = 1.872 \pm 0.4\% MeVcm^2/g$ and $b = 0.0275 \pm 0.4\% cm^2/g$. The conversion $1MeVcm^2/g = 1.6 \cdot 10^{-19} \cdot 10^{-8} Jmm^2/kg$.

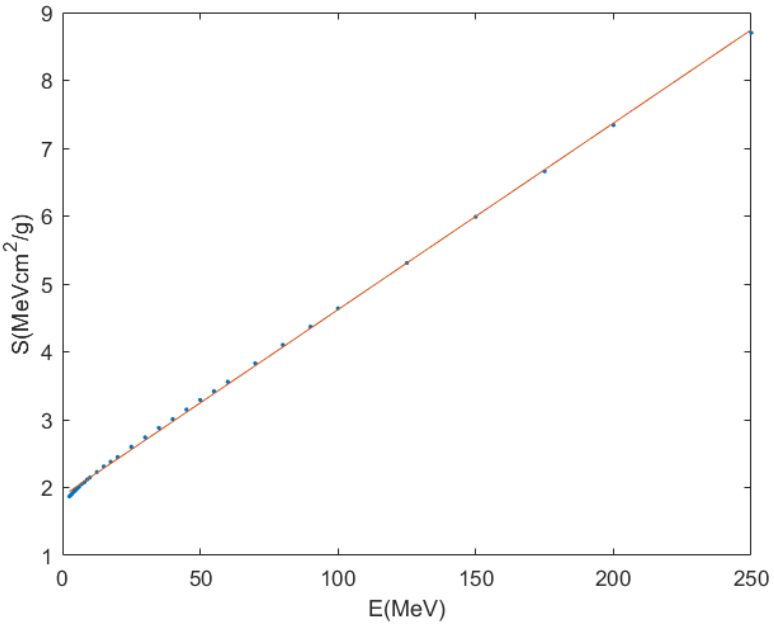


Figure 6.1.2: Mass stopping power for $2MeV < E < 250MeV$

Using the expressions above, dose can be empirically written as:

$$D(Gy) = \frac{25}{2\pi \ln 2} \frac{Q_{bunch}}{\sigma_r^2}(a + bE) \tag{6.1.2}$$

where the values are expressed in $Q(nC)$, $\sigma_r(mm)$ and $E(MeV)$. The constants $a = 1.872 \pm 0.4\% MeVcm^2/g$ and $b = 0.0275 \pm 0.4\% cm^2/g$ were calculated and fitted from experimental data and are valid for $2MeV < E < 250MeV$ (unit conversions were taken into consideration).

If there were no other absorbers like scattering foils or range modulators, the maximum dose for a $Q = 500nC$ bunch, $\sigma_r = 1.8mm$ and $E = 186MeV$ (simulation 5.3.4) would be $D = 6 \cdot 10^3 Gy$. For a linac that outputs pulses at $PRF = 100Hz$, the average dose rate for a single pulse the dose rate would be $\dot{D} \approx 6 \cdot 10^5 Gy/s$.

## 6.2 DNA damage simulation

In this section, I will simulate DNA damage using the MCDS software in an attempt to see the the effects of FLASH irradiation as described in the theoretical part. MCDS does not support FLASH dose rates and the input parameters are very limited. I will instead take into account the oxygen depletion hypothesis and the fact that less ROS are produced in the targeted tissue and analyze DNA damage under those conditions. Calculation for the relative biological effectiveness will be made for both electrons and protons.

### 6.2.1 MCDS Software

The Monte Carlo Damage Simulation (MCDS) Software is designed to simulate DNA damage by different types of radiation, including electrons and ions. [42]

The input file for the Monte Carlo Damage Simulation (MCDS) must have a '.inp' extension and the filename should be in the form of "test.inp".

```
CELL: DNA=1 NDIA=8 CDIA=20
SIMCON: seed=123 nocs=200
RADX: PAR=e KE=10 AD=5
EVO2: mmHg=100
DMSO: CONC=0.2
```

To run the I type the command:

```
./MCDS test.inp
```

**CELL: Cell Characteristics and Parameters**

| Parameter | Specification |
|---|---|
| DNA | DNA content of the cell nucleus (in Gbp) |
| NDIA | Diameter of the cell nucleus (in $\mu$m). |
| CDIA | Diameter of the cell (in $\mu$m) |

Table 6.2.1: CELL Parameters

**SIMCON: Simulation Control Parameters**

| Parameter | Specification |
|---|---|
| seed | Seed for the random number generator |
| nocs | Number of MC simulations. Each simulation represents damage to one cell |

Table 6.2.2: SIMCON Parameters

### RADX: Radiation Exposure Parameters

| Parameter | Specification |
|---|---|
| PAR | Particle type (e.g., e, p, 1H, 2H, 4He, 12C, 56Fe, etc.) |
| KE | Kinetic energy of the particle (MeV) |
| MeV/A | Kinetic energy specified as MeV per nucleon (often used for massive ions) |
| AD | Absorbed dose (Gy) |

Table 6.2.3: RADX Parameters

### EVO2: Environmental O2 Concentration (Oxygen Effect)

| Parameter | Specification |
|---|---|
| pO2 | Percent oxygen concentration (0 to 100%) |
| mmHg | Alternate method to specify the oxygen concentration (760 mmHg = 100%) |

Table 6.2.4: EVO2 Parameters

### DMSO: Parameters Related to Simulating the Effects of DMSO

| Parameter | Specification |
|---|---|
| CONC | DMSO (Dimethyl sulfoxide) concentration (mol $dm^{-3}$) |

Table 6.2.5: DMSO Parameters

In the following simulations, I will irradiate a target composed of cells with a diameter of $20\mu m$ and a nucleus diameter of $8\mu m$, containing $10^9$ base pairs. The target will be exposed to 10 MeV electrons, delivering a dose of 5 Gy.

Dimethyl sulfoxide (DMSO) $(CH_3)_2SO$ is commonly used as a solvent due to its ability to scavenge reactive oxygen species (ROS).

In these simulations, I will vary the oxygen concentration (mmHg[1]) and the DMSO concentration to observe their effects on the outcome.

[1]Millimeters of Mercury (Hg) is a unit of pressure and 1atm=760mmHg. Sometimes it is used to express the partial pressure of gases in biological or medical contexts. Since this unit will be used, assume 100mmHg=13% $O_2$, 10mmHg=1.3% $O_2$ etc

### 6.2.2 Simulation Results

In Figure 6.2.1a I have performed simulations to calculate the total number of clusters per unit Gy and per unit GBp (=$10^9$ base pairs) as a function of the oxygen concentration. The simulations span a range of oxygen levels, from 0.01 mmHg, representing hypoxia, up to 100 mmHg, which corresponds to a well oxygenated tissue. This was repeated for different values of the concentration of DMSO.

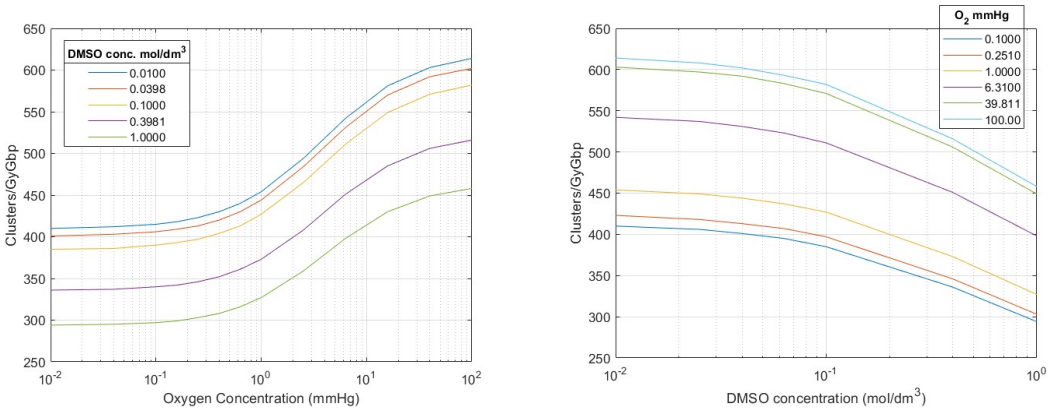


(a) Total DNA damage as a function of the oxygen concentration. The lines represent different DMSO concentrations in mol*dm$^{-3}$

(b) Total DNA damage as a function of the DMSO concentration. The lines represent different oxygen concentrations in mmHg

Figure 6.2.1: Total damage by 10MeV electrons and 5Gy absorbed dose

It is clear that higher oxygen concentrations lead to an increase in DNA damage, which is in accordance to theoretical predictions. Additionally, the graphs are shifted downwards at higher DMSO concentrations, indicating in a reduction in DNA damage.

In Figure 6.2.1b I have performed simulations to calculate the total number of clusters per unit Gy and per unti GBp as a function of the DMSO concentration. The simulations span a range of DMSO concentrations, from 0.01 mol*dm$^{-3}$, representing an environment with higher ROS concentration, up to 1 mol*dm$^{-3}$, which corresponds to less ROS. This was repeated for different values of the concentration of oxygen.

It is clear that for higher DMSO concentrations the DNA damage is reduced. Furthermore, the graphs are shifted upwards at higher oxygen concentrations, as described in the previous set of simulations.

The MCDS software provides SSBs, DSBs and the Total amount DNA damage. Other types of DNA damage include oxidations, base damage etc. The non DSB damage can be more easily repaired by the cell repair mechanisms. Double strand breaks are harder to repair due to the complexity of the damage and the repair mechanisms are more prone to error. The number of SSBs and DSBs respectively is shown in Figure 6.2.2 and it can be said that in 10MeV electrons, about 1/3 of the damage is due to SSBs. [2]

[2]The y axis in 6.2.2 was mistakenly written in the two graphs. The correct value is in the caption of each subfigure

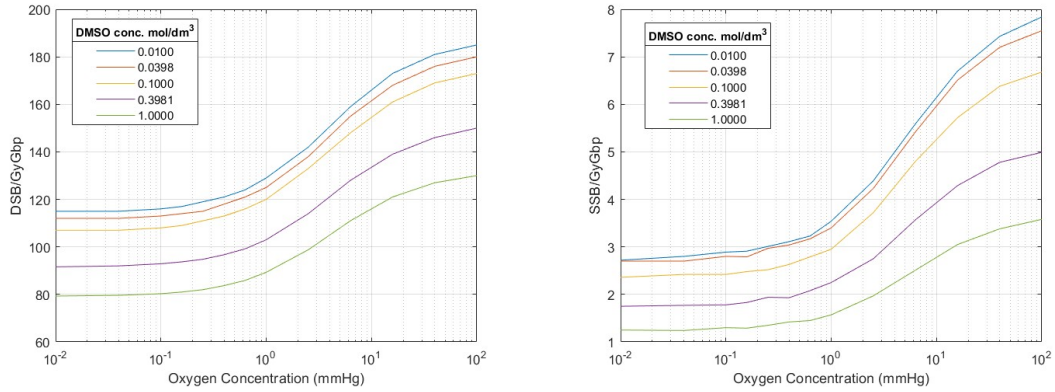


(a) SSBs as a function of oxygen concentration

(b) DSBs as a function of oxygen concentration

Figure 6.2.2: SSBs and DSBs as a function of oxygen concentration - 10MeV electrons

A graph of LET as a function of energy for both protons and electrons was generated using MCDS, as shown in Figure 6.2.3. This closely resembles the theoretical curve presented in Figure 4.3.4.

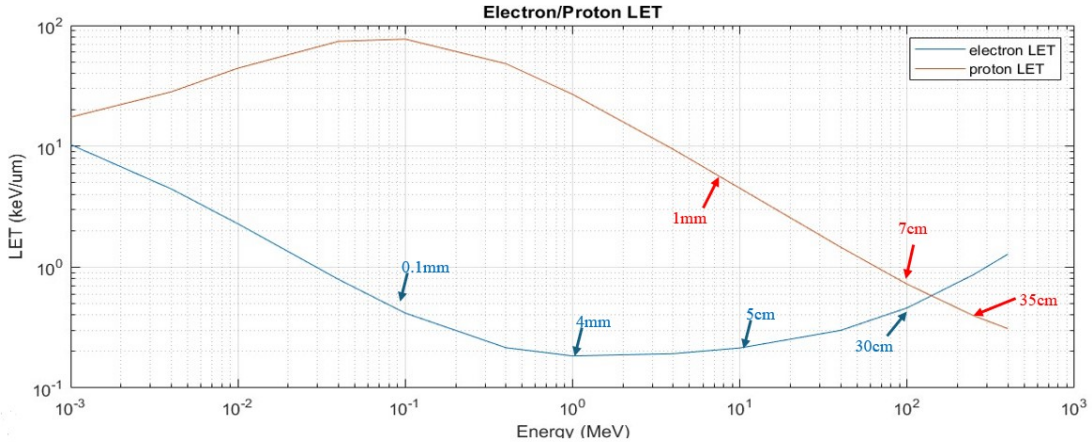


Figure 6.2.3: Proton and Electron LET as a fuction of energy and CSDA range at the given points

### 6.2.3 Calculating RBE

A more accurate measure of the biological impact is provided when calculating the Relative Biological Effectiveness RBE. It can be defined in two ways:

- The ratio of the dose of a reference radiation to the dose of the test radiation required to produce the same biological effect.
- The ratio of the amount of biological damage (e.g., DNA damage) caused by the reference radiation to the damage caused by the test radiation, for an equivalent dose.

In this case the second definition is more useful. The reference radiation is usually the $\gamma$-ray produced from Co-60, but MCDS does not simulate photon radiation. To

compensate for that, I have used 1keV electrons instead. When photons interact with matter, they generate secondary electrons and by setting the radiation to be caused by 1keV electrons for the **same absorbed dose** and identical conditions, it would be a good enough approximation. Since the Oxygen and DMSO concentrations used are the same, RBE can be simply calculated by dividing $N_{test}/N_{ref}$.

Considering the ratio of the total damage, the RBE as a function of oxygen concentration for given values of the DMSO concentration are presented in Figure 6.2.4

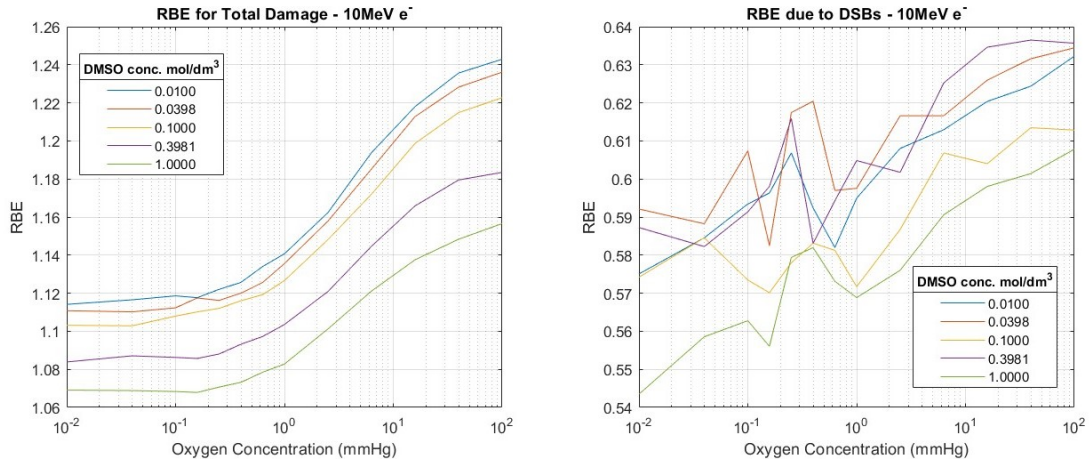


Figure 6.2.4: RBE for total and DSB damage - 10 MeV electrons

Higher RBE values are observed for lower DMSO concentrations and higher oxygen concentrations, similar to Figure 6.2.1a.

It could be argued that non-dsb lesions are more efficiently and accurately repaired and that the permanent damage is mostly attributed to DSBs. For this reason, I created a graph (Figure 6.2.4b) that presents the RBE as a function of the oxygen concentration, but the ratio chosen is:

$$RBE = \frac{DSB_{test}}{DSB_{ref}}\bigg|_{same\_absorbed\_dose}$$

Figure 6.2.5 shows the RBE of electrons as a function of their energy for DSB and non-DSB damage. Low RBE indicates that the test radiation has a similar effect to that of the reference radiation. RBE has higher values for high LET radiation (like protons or ions), whereas electrons have lower LET and consequently lower RBE. In Figure 6.2.5, it is clear that the RBE of electrons shows minimal dependence on the energy of the electrons for E>100keV, and the variation with oxygen concentration is also relatively small. RBE seems to converge to 1 at 1keV, but this happens because it is equal to the reference radiation. While lower-energy electrons, such as 1 keV electrons, have a higher LET and can cause more dense ionizations leading to more DSBs, higher-energy electrons tend to produce fewer DSBs due to their lower LET.

Generally, higher energy protons cause less DSBs, since the LET is lower, which means that the lesions are not very concentrated. As particle energy decreases,

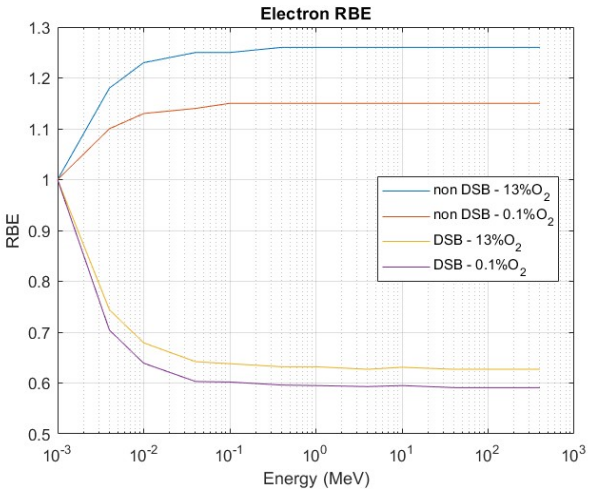


Figure 6.2.5: RBE of electrons as a function of Energy. RBE values converge to 1keV since this energy was used for reference

LET increases, which results to more concentrated lesions, and a higher proportion of DNA damage is attributed to DSBs. This behaviour is demonstrated in the case of 200MeV and 100keV protons in figure 6.2.6. The higher-energy protons primarily interact at the entrance of the irradiated tissue, while the lower-energy protons correspond to the energy at the Bragg peak region, where most of the energy is deposited.

The simulations presented in Figure 6.2.6 illustrate both the total and partial DNA damage caused by double-strand breaks (DSBs) for high and low energy protons. Generally the LET of protons is higher than that of electrons, so the amount of DSBs is a lot higher and it can be seen in the 100keV runs, as the RBE value is around 5 for hypoxic enviroments and around 2 for normal tissues. This is a very high value and it is indicative of the benefits of proton therapy, because at the Bragg peak region the RBE is very high, more Double Strand Breaks are induced, that are harder to repair, suggesting a high killing efficiency.

As RBE is a comparison between the tested and a reference damage by low energy electrons, whose LET is lower than that of protons, the number of DSBs for electrons will be very low, especially at low oxygen concentrations. Electrons usually do indirect damage via ROS, that require oxygen in order to be produced. This is the reason behind the very higher RBE values at low oxygen concentrations in the case of protons. A more analytical expression of proton RBE as a function of energy is shown in Figure6.2.7, whereas for electrons the value of RBE for energies $100keV < E < 100MeV$ seems to be relatively constant around 1.2 for non-DSB damage and around 0.6 for DSB only damage.

In the high-energy region, the RBE values for the total number of lesions are around 1.1, while for the graph that only consists of DSBs, the RBE values are around 0.6. This suggests that at the entrance of the irradiated area, fewer DSBs are induced compared to the reference dose, and a higher fraction of damage consists of lesions that are easier for the cell to repair. This highlights the advantage

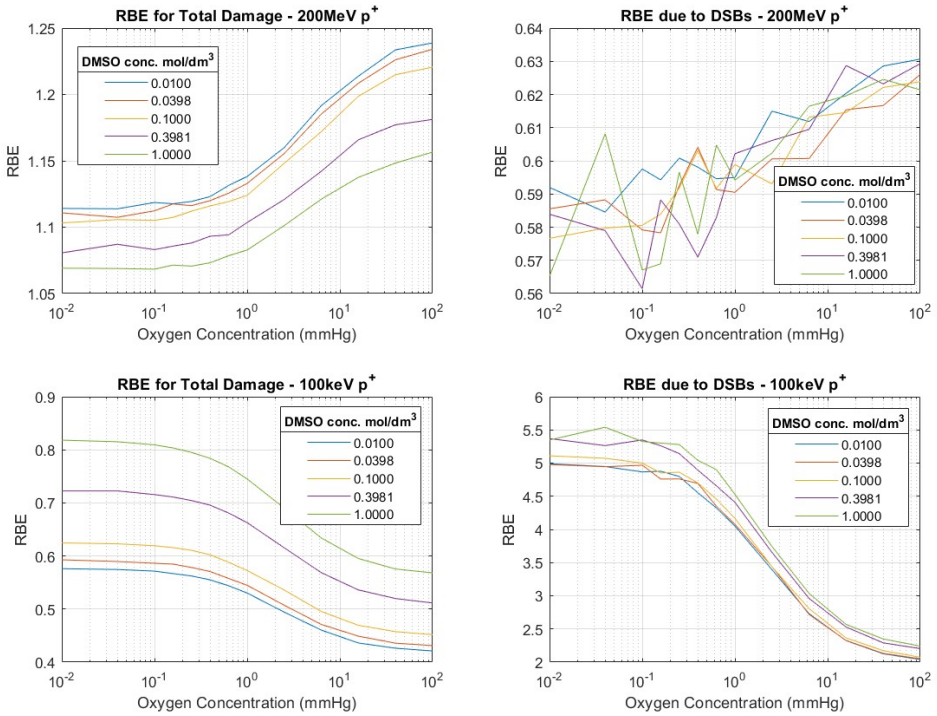


Figure 6.2.6: RBE of protons as a function of oxygen and DMSO concentrations for different energies

of using protons for irradiating deep seated tumours. The proton beam's energy is modulated in order for the Bragg peak to be positioned within the tumor to maximize damage.

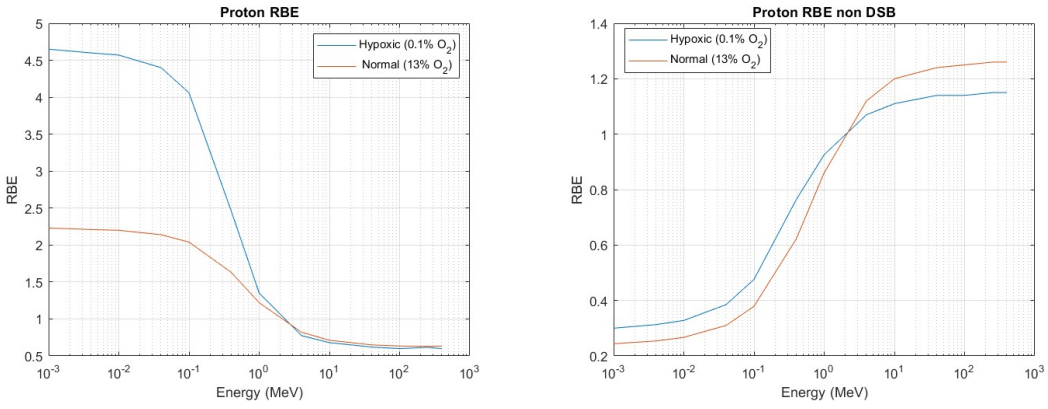


(a) Proton RBE for damage due to DSBs

(b) Proton RBE for damage due to non-DSB

Figure 6.2.7: Proton RBE for DSB and non-DSB damage as a function of Energy

### 6.2.4 Discussion about FLASH

According to our hypothesis, when comparing FLASH-RT with CONV-RT, the graphs should be interpreted as follows:

- CONV-RT
  - The production of ROS is normal, so we focus on lower DMSO concentrations, which is a ROS scavenging agent.
  - The oxygen levels do not change during the irradiation process, so for normal tissues we consider higher values of oxygen concentration (100mmHg =13%)
- FLASH-RT
  - The production of ROS is limited because of the timescale, oxygen levels, so we focus higher DMSO concentrations, as the scavenging agent removes ROS.
  - The oxygen is temporarily depleted during FLASH irradiation, so momentarily we consider lower values of oxygen concentration.

The normal tissue sparing effect of the FLASH effect is evident in Figures 6.2.1a and 6.2.1b. As the oxygen concentration decreases and the DMSO concentration increases, less DNA damage occurs, as reflected by fewer clusters of lesions in the graphs. This mirrors the behavior of normal tissue under the FLASH effect, where rapid oxygen depletion leads to less ROS production and as a consequence less damage. A similar trend is observed in the simulations shown in Figure 6.2.2, in which only the effect of DSBs is shown, that can cause more severe and potentially irreversible DNA damage.

Tumors are often hypoxic due to poor vascularization and usually have higher ROS concentrations. In Figure 6.2.1a, the green line (DMSO = 1.00 mol/dm$^3$ - bottom line) can be considered a representation of normal tissue under the FLASH effect, where fewer lesions are produced due to reduced ROS formation. On the other hand, tumor tissue would correspond to one of the lines above this green line, indicating more lesions and damage due to ROS. This takes into consideration the fact that tumors are already hypoxic, the oxygen levels are not drastically reduced under FLASH irradiation and are less protected from the FLASH effect.

For conventional radiotherapy (CONV-RT), the behavior of normal and tumor tissues can be shown when focusing to the right side of the graphs. Normoxic normal tissues would correspond to higher oxygen concentrations (around $10^2 mmHg$), where more lesions are produced due to the greater availability of oxygen, enhancing ROS production. Tumors, with their hypoxic nature, would fall into the middle range (around $10^0 - 10^1 mmHg$) on the graph. In this case, they would still produce significant lesions, but less than well-oxygenated normal tissue, making tumors more resistant to conventional therapy compared to normal cells.

On Figure 6.2.5, it is evident that the RBE of electrons does not depend that much on the energy of electrons and the dependence on oxygen concentreation is not that much. Since 1keV electrons have higher LET, the number of DSBs

is reduced for higher energy electrons that have lower LET. Also for low oxygen concentrations that could be caused by the transient hypoxia, it seems as if the effectivness of electrons is a bit lower than for oxygenated in doing DSBs. Thus the values of Figure 6.2.4 are valid for a broader energy spectrum rather than just 10MeV.

In Figure 6.2.5, it was demonstrated that the RBE of electrons shows minimal dependence on the energy of the electrons for E>100keV, and the oxygen dependence is also relatively small. For low oxygen concentrations that could be caused by transient hypoxia, the effectiveness of electrons in inducing DSBs appears to be slightly reduced compared to oxygenated conditions. This suggests that oxygen has a small impact on the RBE in terms of causing DSBs.

The case of protons (Figure 6.2.6 and 6.2.7) is particularly interesting because their RBE for DSBs varies significantly with energy and oxygen concentration. At high energies, corresponding to the entrance region of the irradiated tissue, the RBE is relatively low due to the lower LET of protons in this region, which is very beneficial for normal tissue sparing. However, as protons slow down, their LET increases dramatically to around 70 keV/μm at the Bragg peak region, leading to a much higher RBE. Low oxygen environments could be caused by the transient hypoxia associated with the FLASH effect and it seems to have a significant effect.

This increase in RBE near the Bragg peak occurs because, at low energies, protons cause more direct DNA damage and the presence of oxygen is not that important anymore, as OER drops at high LET (Figure 4.3.2). In contrast, reference radiations like X-rays or electrons primarily rely on ROS production, which is oxygen-dependent, to induce DNA damage. Therefore, protons at low energies remain highly effective even under hypoxic conditions, making them especially potent at causing DSBs, while the effectiveness of low-LET radiation drops significantly in the absence of oxygen.

Even though the oxygen depletion hypothesis is not widely accepted to be the reason behind the normal tissue sparing effect of FLASH-RT, the findings presented here could still be useful for studying the effect of protons and electrons to tissues with different oxygen or ROS concentrations. The advantage of proton therapy is also demonstrated above. This study was more of a physio chemical approach to the FLASH effect, since biological factors including the fact that some proteins or other structures could be more resistant to FLASH irradiation. Further research is important to understand the underlying mechanisms.

# 7 Conclusions

This thesis consisted of two parts; the LINAC simulation and the DNA damage simulation.

The ASTRA software proved to be quite a powerful tool for analyzing electron beam parameters within the accelerating structure, the output beam characteristics and the space charge forces. Initially no space charge effects were taken into account in order to familiarize with the software capabilities and its interface. Once space charge effects were included, the differences were noticeable, especially for high bunch charges. This work could have been better if quadrupole magnets were added to create FODO lattice that would focus the beam, or by taking the wakefields into consideration. A suitable software for this purpose could be MADX (Methodical Accelerator Design), by CERN. MADX is a tool used for the design, simulation, and optimization of particle accelerators.

The MCDS software was very useful qualitatively assessing the effects of various parameters at the irradiated site. Even though simulating FLASH dose rates was not possible, key hypotheses from existing research including oxygen depletion and the role of ROS were taken into account. Through this indirect procedure estimations of the FLASH effect were made for both protons and electrons by calculating DSB and non-DSB damage and comparing the results with those of low energy electrons instead of $\gamma$ rays that are not supported by MCDS to calculate the relative biological effectiveness. This simulation could be performed again in the future using more advanced software like GEANT4, as ongoing research is developing libraries capable of accurately simulating FLASH effects.

# 8 Bibliography

## References


[1] Thomas P Wangler. *RF Linear accelerators*. John Wiley & Sons, 2008.

[2] Martin Reiser. *Theory and design of charged particle beams*. John Wiley & Sons, 2008. Chapters 43-44.

[3] David H. Dowell. Lecture 2: Electron emission and cathode emittance. In *online notes*. STANFORD LINEAR ACCELERATOR CENTER, 2015.

[4] Helmut Wiedemann. *Particle accelerator physics 4th edition*. Springer Nature, 2015.

[5] Unknown. Source Unknown. Efforts to locate the original source were unsuccessful.

[6] CJ Karzmark and Neil C Pering. Electron linear accelerators for radiation therapy: history, principles and contemporary developments. *Physics in Medicine & Biology*, 18(3):321, 1973.

[7] Jörg Rossbach and Peter Schmueser. Basic course on accelerator optics. Technical report, P00011673, 1993.

[8] Klaus Wille. *The physics of particle accelerators: an introduction*. Clarendon Press, 2000.

[9] International Atomic Energy Agency and International Atomic Energy Agency. Radiation biology: A handbook for teachers and students, 2010.

[10] Jonathan R Hughes and Jason L Parsons. Flash radiotherapy: current knowledge and future insights using proton-beam therapy. *International journal of molecular sciences*, 21(18):6492, 2020.

[11] J Anthony Seibert. X-ray imaging physics for nuclear medicine technologists. part 1: Basic principles of x-ray production. *Journal of nuclear medicine technology*, 32(3):139–147, 2004.

[12] Omar Desouky and Guangming Zhou. Biophysical and radiobiological aspects of heavy charged particles. *Journal of Taibah University for Science*, 10, 04 2015.

[13] National Research Council, Division on Earth, Life Studies, Board on Radiation Effects Research, and Committee to Assess Health Risks from Exposure to Low Levels of Ionizing Radiation. Health risks from exposure to low levels of ionizing radiation: Beir vii phase 2. _, 2006.

[14] Binwei Lin, Feng Gao, Yiwei Yang, Dai Wu, Yu Zhang, Gang Feng, Tangzhi Dai, and Xiaobo Du. Flash radiotherapy: history and future. *Frontiers in oncology*, 11:644400, 2021.

[15] Wikipedia contributors. Radio spectrum - ieee, 2024. Accessed: 2024-07-31.

[16] M Stanley Livingston. Early history of particle accelerators. In *Advances in Electronics and Electron Physics*, volume 50, pages 1–88. Elsevier, 1980.

[17] Luis W Alvarez, Hugh Bradner, Jack V Franck, Hayden Gordon, J Donald Gow, Lauriston C Marshall, Frank Oppenheimer, Wolfgang KH Panofsky, Chaim Richman, and John R Woodyard. Berkeley proton linear accelerator. *Review of Scientific Instruments*, 26(2):111–133, 1955.

[18] Anil K Maini. *Handbook of defence electronics and optronics: fundamentals, technologies and systems*. John Wiley & Sons, 2018.

[19] Albert L. Septier Pierre M. Lapostolle. *Linear Accelerators*. North Holland Publishing Company, 1970.

[20] Arthur Wehnelt. X. on the discharge of negative ions by glowing metallic oxides, and allied phenomena. *The London, Edinburgh, and Dublin Philosophical Magazine and Journal of Science*, 10(55):80–90, 1905.

[21] Franz Mandl. *Statistical physics*, volume 14. John Wiley & Sons, 1991.

[22] Shyh-Yuan Lee. *Accelerator physics*. World Scientific Publishing Company, 2018.

[23] RE Collins. Foundations for microwave engineering, piscataway, 2001.

[24] Klaus Floettmann. Some basic features of the beam emittance. *Physical Review Special Topics-Accelerators and Beams*, 6(3):034202, 2003.

[25] USPAS. Us particle accelerator school. In *Fundamentals of Accelerator Physics and Technology with Simulations and Measurements Lab*. uspas, January 2023.

[26] Donald A Edwards and Michael J Syphers. *An introduction to the physics of high energy accelerators*. John Wiley & Sons, 2008.

[27] Faiz M Khan. *The physics of radiation therapy*. Lippincott Williams & Wilkins, 2010.

[28] Glenn F Knoll. *Radiation detection and measurement*. John Wiley & Sons, 2010.

[29] Ervin B Podgorsak. *Radiation oncology physics: a handbook for teachers and students*. iaea, 2005.

[30] Amin I Kassis. Molecular and cellular radiobiological effects of auger emitting radionuclides. *Radiation protection dosimetry*, 143(2-4):241–247, 2011.

[31] Eivind Rørvik. Scoring of linear energy transfer (let) for calculation of biological dose in proton therapy. In *cern*. CERN, 2016.

[32] E.N. Gazis. *Ιοντίζουσες Ακτινοβολίες - Φυσική - Εφαρμογές*. Εθνικό Μετσόβιο Πολυτεχνείο, 1999.

[33] Nimrat Chatterjee and Graham C Walker. Mechanisms of dna damage, repair, and mutagenesis. *Environmental and molecular mutagenesis*, 58(5):235–263, 2017.

[34] Vincent Favaudon, Laura Caplier, Virginie Monceau, Frédéric Pouzoulet, Mano Sayarath, Charles Fouillade, Marie-France Poupon, Isabel Brito, Philippe Hupé, Jean Bourhis, et al. Ultrahigh dose-rate flash irradiation increases the differential response between normal and tumor tissue in mice. *Science translational medicine*, 6(245):245ra93–245ra93, 2014.

[35] Yinghao Lv, Yue Lv, Zhen Wang, Tian Lan, Xuping Feng, Hao Chen, Jiang Zhu, Xiao Ma, Jinpeng Du, Guimin Hou, et al. Flash radiotherapy: A promising new method for radiotherapy. *Oncology letters*, 24(6):1–14, 2022.

[36] Jeannette Jansen, Jan Knoll, Elke Beyreuther, Jörg Pawelke, Raphael Skuza, Rachel Hanley, Stephan Brons, Francesca Pagliari, and Joao Seco. Does flash deplete oxygen? experimental evaluation for photons, protons, and carbon ions. *Medical physics*, 48(7):3982–3990, 2021.

[37] Guillem Pratx and Daniel S Kapp. A computational model of radiolytic oxygen depletion during flash irradiation and its effect on the oxygen enhancement ratio. *Physics in Medicine & Biology*, 64(18):185005, 2019.

[38] Douglas R Spitz, Garry R Buettner, Michael S Petronek, Joël J St-Aubin, Ryan T Flynn, Timothy J Waldron, and Charles L Limoli. An integrated physico-chemical approach for explaining the differential impact of flash versus conventional dose rate irradiation on cancer and normal tissue responses. *Radiotherapy and oncology*, 139:23–27, 2019.

[39] Chidi M Okoro, Emil Schüler, and Cullen M Taniguchi. The therapeutic potential of flash-rt for pancreatic cancer. *Cancers*, 14(5):1167, 2022.

[40] K Flöttmann. Astra: A space charge tracking algorithm, user's manual, 2017.

[41] Massimo Ferrario, Mauro Migliorati, and Luigi Palumbo. Space charge effects. *arXiv preprint arXiv:1601.05214*, 2016.

[42] Robert Steward. Monte carlo damage simulation (mcds) software, 2012.

| **Acronym** | **Definition** |
|---|---|
| LINAC | Linear Accelerator |
| ASTRA | A Space Charge Tracking Algorithm |
| RF | Radio Frequency |
| ROS | Reactive Oxygen Species |
| LET | Linear Energy Transfer |
| CDSA | continuous slowing down approximation |
| DMSO | Dimethyl Sulfoxide |
| RBE | Relative Biological Effectiveness |
| OER | Oxygen Enhancement Ratio |
| MCDS | Monte Carlo Damage Simulation |
| FLASH | Radiotherapy with dose rate >40Gy/s |
| CONV-RT | Conventional Radiotherapy |
| UHDR | Ultra High Dose Rate |
| SSB | Single Strand Break |
| DSB | Double Strand Break |

Table 8.0.1: List of Acronyms and Definitions